Brain state evaluation in multi-modal brain signal recordings

Dissertation

zur Erlangung des Grades eines
Doktors der Naturwissenschaften

der Mathematisch-Naturwissenschaftlichen Fakultät
und
der Medizinischen Fakultät
der Eberhard-Karls-Universität Tübingen

vorgelegt
von

Kengo Takahashi
aus Kyoto, Japan

2023

Tag der mündlichen Prüfung: 4.4.2023

Dekan der Math.-Nat. Fakultät: Prof. Dr. Thilo Stehle
Dekan der Medizinischen Fakultät: Prof. Dr. Bernd Pichler

1. Berichterstatter: Dr. Xin Yu

2. Berichterstatter: Prof. Dr. Cornelius Schwarz

Prüfungskommission: Prof. Dr. Jan Born

Prof. Dr. Klaus Scheffler

Prof. Dr. Cornelius Schwarz

Dr. Xin Yu

Erklärung / Declaration:

Ich erkläre, dass ich die zur Promotion eingereichte Arbeit mit dem Titel: „Brain state evaluation in multi-modal brain signal recordings“ selbständig verfasst, nur die angegebenen Quellen und Hilfsmittel benutzt und wörtlich oder inhaltlich übernommene Stellen als solche gekennzeichnet habe. Ich versichere an Eides statt, dass diese Angaben wahr sind und dass ich nichts verschwiegen habe. Mir ist bekannt, dass die falsche Abgabe einer Versicherung an Eides statt mit Freiheitsstrafe bis zu drei Jahren oder mit Geldstrafe bestraft wird.

I hereby declare that I have produced the work entitled: "Brain state evaluation in multi-modal brain signal recordings", submitted for the award of a doctorate, on my own (without external help), have used only the sources and aids indicated and have marked passages included from other works, whether verbatim or in content, as such. I swear upon oath that these statements are true and that I have not concealed anything. I am aware that making a false declaration under oath is punishable by a term of imprisonment of up to three years or by a fine.

Tübingen, den ....

Datum/Date Unterschrift/Signature

Abstract

Brain states, which indicate degrees of arousal during wakefulness, sleep, or anesthesia, have been long investigated over the last decades. The dynamics of distinct brain states are conserved across different species of animals and tightly linked to physiological behaviors (e.g., pupil size modulation) and specific brain network activity. Both pupil size and brain states are substantially regulated by neuromodulators originating from the brainstem and subcortical structures through interactions with the cerebral cortex, partly sharing common regulatory pathways. For this reason, pupil size and neuronal activities of arousal-regulating brain regions demonstrate high correlations. However, the correlation emerges with high variability across recording trials, indicating a possible involvement of complex pupil- and brain state- regulatory pathways, including brain regions of the lateral hypothalamus (LH) and anterior cingulate cortex (ACC) that could induce the varied correlation properties. In this dissertation, I aim to shed light on neural pathways regulating the brain state and pupil size variations using a multi-modal experimental design in three research protocols. The first goal was to demonstrate a platform to bridge the fields of functional magnetic resonance imaging (fMRI), pupillometry, and fiber photometry neuronal Ca^{2+} recordings in anesthetized animals and evaluate brain state dynamics from across-scale recordings. Using the information from Ca^{2+} signals, we first distinguished different brain states. In each of these brain states, different correlation features between fMRI signal and pupil size changes appeared, e.g., strong positive correlations in the A5 region where noradrenergic neurons are located. The second goal was to assess cross-scale brain dynamics in electrophysiology, fMRI, pupillometry, and fiber photometry Ca^{2+} recordings for specifying different brain states under anesthesia based on the lateral hypothalamic (LH) activity. Across multi-scale recording trials, both local field potential (LFP) and fMRI signals detected in the LH presented distinct brain states with consistent distribution patterns of positive and negative correlations with pupil dynamics. The association of different pupil dynamics to a distinct brain state was further verified by neuronal activity coupling between the LH and anterior cingulate cortex (ACC), indicating the LH-ACC circuit-specific regulation of pupil dynamics. The third goal was to demonstrate the properties of the LH regarding pupil size and brain state regulations using optogenetics, pupillometry, and electrophysiology. Optogenetic stimulation of the LH in anesthetized animals evoked pupil dilation and LFP delta power reduction. These changes showed an exponential relationship with respect to the stimulation frequency. Moreover, the exponential feature was observed only under one specific underlying brain state for LFP delta power reduction but under all brain states for pupil dilation. These observations suggested that the LH mediates pupil size independently of the underlying brain state variations. Overall, these studies identified several important features of pupil-regulatory circuits underlying brain-state transitions under anesthesia. The complex signal interdependence shown here indicated that the brain state is orchestrated in multiple regions (especially the LH and ACC) and at multiple scales (frequency and amplitude of neuronal firing, inter-region correlation with pupil size, neurovascular coupling, etc.). This dissertation presents a novel way to track brain state transitions by connecting pupillary signals and their variable

relationship with the whole brain signal and offers a reference framework to understand the LH-ACC relationship. We demonstrate that LH/ACC activity provides a strong indication of different vigilance levels and may become a useful approach to evaluate the ongoing brain states in arousal-related clinical research.

Contents

Acronyms

AAV	adeno-associated virus
ACC	anterior cingulate cortex
ANOVA	analysis of variance
ARAS	ascending reticular activating system
A5	noradrenergic cell group 5
Ca^{2+}	calcium
BOLD	blood oxygen level dependent
ChR2	channelrhodopsin-2
EEG	electroencephalogram
EPI	echo planar imaging
EWN	Edinger-Westphal nucleus
FDR	false discovery rate
fMRI	functional magnetic resonance imaging
GABA	gamma-aminobutyric acid
GCaMP	green fluorescent protein-calmodulin fusion protein
GE	gradient echo
IML	intermediolateral column
LC	locus coeruleus
LH	lateral hypothalamus
LFP	local field potential
MCH	melanin-concentrating hormone
MR	magnetic resonance
MRI	magnetic resonance imaging
MI	modulation index
MUA	multiunit activity
NREM	non-rapid eye movement
PLV	phase locking value
RARE	rapid acquisition with relaxation enhancement
REM	rapid eye movement
RF	radio frequency
ROI	region of interest
TE	echo time
TR	repetition time
T_2^*	transverse relaxation time constant
VGAT	vesicular GABA transporter
VTA	ventral tegmental area

1 Chapter I: Introduction to the evaluation of brain state

The brain of animal and human has developed uniquely over millions of years. A number of animals across different species share fundamental brain structures and behavioral features and have common regulatory features to control physiological processes such as sleeping and eating. Brain states are referred to as various degrees of wakefulness or different depths of sleep or anesthesia that vary across temporal scales, and they are one of the fundamental features seen across all animal species (e.g., mammals, fish, birds, and insects) [1–6]. Brain states transit from one to another such as the transition between sleep and wakefulness [1, 7]. Even within sleep, wakefulness, or anesthesia, the brain state oscillates and switches from one to another state periodically as a result of arousal regulation; for instance, from a rapid eye movement (REM) to non-rapid eye movement (NREM) sleep [1, 8–11]. Studies have investigated different brain states through behavioral observations such as pupillometry and brain signal measures such as electrophysiological and functional magnetic resonance imaging (fMRI) signals. [9, 10, 12–15]. One of the most well-known methods to evaluate the brain state is the measurement of electrophysiological signals such as electroencephalogram (EEG) and local field potential (LFP). By observing different features of electrical activity in the brain (e.g., slow oscillations and high amplitude during sleep but high frequency and low amplitude during wakefulness), a clear distinction of different brain states is possible [1] (Figure 1.1). However, the definition of a certain brain state is still controversially discussed among researchers since the term often implies characteristics of different behavioral and physiological phenomena detected at multiple scales [5, 6]. When two brain

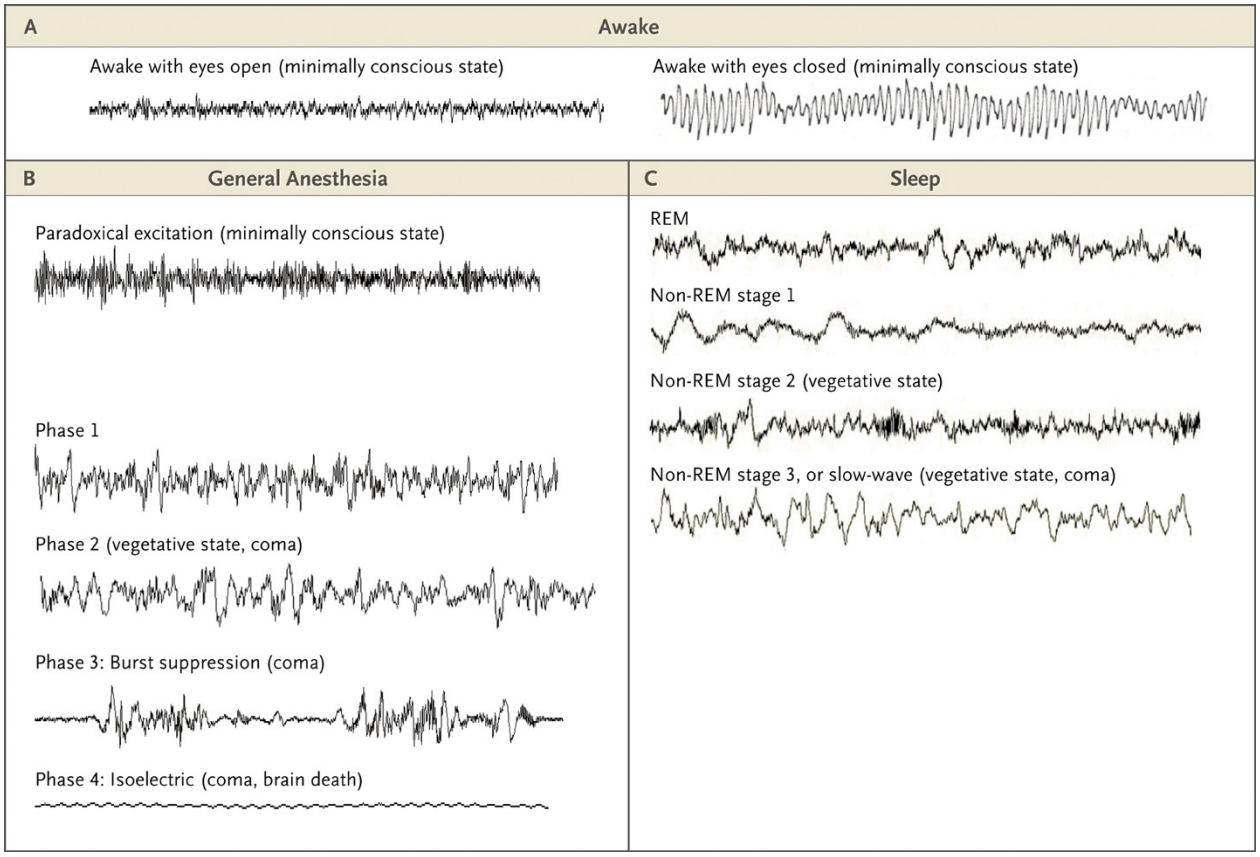

Figure 1.1 Diverse features of electrophysiological signals under different brain states of wakefulness, coma, anesthesia, and sleep. Reproduced with permission from [1], Copyright Massachusetts Medical Society.

states are clearly distinguishable through electrophysiological signals, e.g., wakefulness and NREM sleep, researchers agree that these visible differences in electrophysiological signals indicate two different brain states. However, different brain states also exist within non-radically different sub-states of the brain. For instance, fluctuation of neuronal signals and pupil size occurs under anesthesia, and these changes commonly indicate different degrees of arousal [11, 16–19]. These oscillations of neuronal signals and pupil size can be consistently observed within sleep or wakefulness, also suggesting distinct brain states [9, 20]. Indeed, brain states under anesthesia share similarities with different stages of the sleep cycle, indicating possession of similar brain state regulatory systems [21, 22]. Due to the nature of complex degrees in the arousal level, the distinction of different brain states often requires to perform exploratory analyses such as functional connectivity analysis in fMRI or correlation analysis across multi-modal recording methods [20, 23–25]. Since understanding the full scale of these sub-states is challenging, further research is necessary to facilitate comprehension of the brain state.

1.1 Cortical and subcortical regulation of the brain state and pupil size under unconsciousness

A number of evidences show that subcortical and brainstem structures mediate brain arousal states mainly through the ascending reticular activating system (ARAS) in the vertebrate brain [26–29]. In fact, lesions in the ARAS lead to disorders of consciousness such as coma [30]. ARAS is comprised of multiple brain nuclei that release different neurotransmitters respectively for arousal regulation, e.g., noradrenaline from the locus coeruleus (LC), acetylcholine from the laterodorsal tegmental nucleus, dopamine from the ventral tegmental area, and serotonin from the raphe nuclei [26]. These midbrain/brainstem nuclei send their projections to extensive regions of the cortex and regulate brain states [26, 31, 32]. The transfer of neuronal signals in this relay from the brainstem to the cortex is closed at the thalamus during the unconscious state (both sleep and anesthesia) [33], and therefore sensory inputs do not pass through to the

cortex. During a deep unconscious state, interactions between glutamatergic pyramidal cells (excitation) and gamma-aminobutyric acid (GABA) interneurons (inhibition) in the cortex generate up (depolarization) and down (hyperpolarization) states. The balance of cortical excitation and inhibition produces the slow wave, which can be observed as delta waves (1-4 Hz) in EEG during sleep and anesthesia [7, 34]. The bursting activities of cortical neurons that produce the up and down states of slow waves are delivered to the thalamus from layer 5 and 6 of cortical neurons [34]. The thalamic neurons have the ability to fire rhythmically, and the glutamatergic excitatory cells project to layer 4 of the cortex. Synchronization of reciprocal activities between the cortex and thalamus enables us to detect the slow wave in electrophysiology. These slow waves are disrupted by activation of the brainstem since various neurotransmitters are released and modulate cortical and thalamic activities [26, 27, 35]. Even within different brain states under unconsciousness, neurons in the subcortical and brainstem areas (e.g., the LC and lateral hypothalamus (LH)) are discharged differently [26, 36, 37]. Thus, studies focused on the functional mechanisms and interactions of cortical and subcortical areas contribute to the understanding of brain state regulations.

1.1.1 Neuronal mechanisms of pupil size modulation

The change in brain states is often reflected in pupil size and in electrophysiological signals of the brain [5, 9, 20, 38]. Pupil size is modulated by multiple brain regions that also regulate the brain state such as the LC and hypothalamus [39–42] (Figure 1.2). The pupil size changes spontaneously over time in a resting state, also known as pupillary hippus [38]. This rhythmic dilation and constriction of pupil size are controlled by the balance between sympathetic and parasympathetic pathways through the brainstem and subcortical regions [41, 42]. The pupil dilation is regulated by an increase in the sympathetic activity or decrease in the parasympathetic activity. The muscle of the iris, responsible for pupil size enlargement through the sympathetic pathway, is controlled by the Edinger-Westphal nucleus (EWN) via the ciliary ganglion for pupil size enlargement through the sympathetic pathway. The pupil constriction is primarily regulated by an

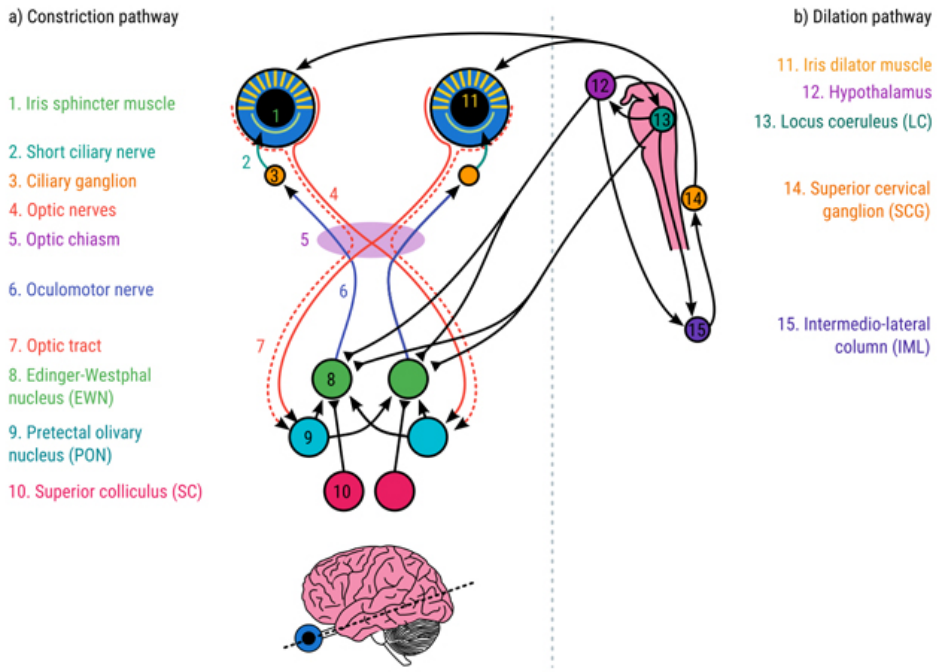

Figure 1.2 Pupil size modulation by multiple brain regions (Adapted from [42]).

increase in the parasympathetic activity. The sphincter muscle of the iris is controlled by the intermediolateral column (IML) via the superior cervical ganglion for pupil size reduction through the parasympathetic pathway. Both IML and EWN receive projections from the LC [42, 43], and therefore, neuronal activities of LC are often reflected in and correlated with pupil size [39, 41, 44–46]. However, recent studies have shown that pupil size does not always anticipate the neural activity of these arousal-regulating neurons such as the LC due to the influence of brain states [47]. In fact, electrical stimulation of the LC evokes pupil dilation but with a time delay of milliseconds to a second [45, 46], further indicating the involvement of other brain regions in pupil size modulation [38]. Indeed, in addition to neuronal projections from the LC to the IML and EWN, other brain regions such as the hypothalamus and superior colliculus also send projections to these nuclei [42–44]. Hence, high correlations between pupil size and arousal-regulating neuronal activities can be also observed in a distant region such as the anterior cingulate cortex (ACC) [46, 48].

1.1.2 The role of midbrain and brainstem in brain state regulation

It has long been known that midbrain and brainstem regions play a crucial role in arousal regulation [26, 49–51]. There was earlier evidence that the ARAS originated from the reticular formation of the brainstem since stimulation of this region triggered cortical activation [27, 29]. In fact, lesions of the ARAS lead to the opposite effect, abolishing cortical activation and generating slow waves [28, 52, 53]. With the advance of experimental techniques in recent years, multiple studies also revealed functional roles of more specific midbrain and brainstem nuclei on mediating brain states such as the LC [51], ventral tegmental area (VTA) [54], dorsal raphe nucleus [55], and LH [56]. These subcortical/brainstem regions possess essential cell groups that release arousal-modulating neurotransmitters, e.g., dopaminergic, noradrenergic, GABAergic, and orexinergic neurons [57]. For instance, dopaminergic neurons in the VTA contribute to cortical arousal, shown by evidence that electric stimulation of VTA and optogenetic stimulation of dopaminergic neurons in the VTA induces wakefulness from anesthesia [54, 58]. Thus, different types of neurotransmitters contribute to physiological regulation distinctly, evidenced by pupil size, electrophysiologically-defined arousal or autonomic modulation [45, 50, 55, 56, 59, 60]. Previous studies demonstrated that noradrenergic neuronal activities in the LC particularly correlate with certain markers of arousal (e.g., EEG and electromyography) as well as with pupil size [39, 41, 50]. In fact, direct activation of the LC through electric and optogenetic stimulation induces pupil dilation and also cortical discharges when animals are under unconsciousness [39, 50, 61, 62]. However, the correlation between pupil size and neuronal activity of the LC is not always linear [46, 47]. It is suggested that other brain-state regulating regions such as hypothalamus and ACC may be involved in pupil size modulation [63].

1.1.3 The role of lateral hypothalamus in brain state regulation

The LH is a distinct brain region in the subcortical structure where various types of arousal-regulating neurons co-exist such as orexin, vesicular GABA transporter (VGAT),

and melanin-concentrating hormone (MCH) expressing neurons [64]. Neuronal activity of the LH is involved in mediating different brain states during anesthesia, sleep, and wakefulness [13, 15, 65, 66]. Orexin neurons, (also known as hypocretin neurons) found exclusively in the LH, are one of the most long-investigated nuclei for arousal regulation [64, 67, 68]. Studies on this neuronal population have shown that a deficit of orexin neuropeptides causes narcolepsy in animals [69, 70] and that neurodegeneration of orexin neurons is linked to human narcolepsy [71, 72]. Besides, their neuronal activity increases during wakefulness but decreases during slow-wave sleep or anesthesia [65, 73]. In fact, optogenetic activation of orexin neurons leads to a brain state transition from NREM sleep to wakefulness [74], and optogenetic silencing of orexin neurons promotes slow-wave sleep [75]. This fact strongly suggests that orexin neurons are crucial for brain state regulation. In addition to orexin neurons, studies using optogenetics and chemogenetics demonstrated that other neuronal populations of the LH such as VGAT and glutamatergic neurons also promote wakefulness [15, 76]. However, MCH neurons [77] in the LH have an opposite functional role compared to the other neuronal types of the LH, promoting sleep [26, 78, 79]. These neurons are less active during wakefulness but more active during sleep, especially in REM sleep [80]. They fire maximally during REM sleep, low during NREM sleep, and minimally during wakefulness. Optogenetic studies also confirmed that MCH neurons promote sleep [79, 81]. Each neuronal population of the LH fires during a certain brain state but stays silent during others, e.g., reduced discharges of awake-enhancing neurons such as orexin neurons during anesthesia or NREM sleep [65, 73]. In consistence with the rate of neuronal discharges in the LH, optogenetic/electric manipulation of LH neurons with different stimulation frequencies modulates brain states differently, evoking brain state alteration when higher stimulation frequencies ($\geq 5\,\mathrm{Hz}$) are applied [15, 74, 81, 82]. The LH neurons are projected to a number of both cortical and subcortical regions that also mediate the brain state such as the thalamus, VTA, LC, and ACC [13, 15, 83–85]. A part of these LH-projected regions such as LC, EWN, and ACC are also involved in pupil size regulations, demonstrating high correlations between neuronal activity of these regions and pupil size [46, 48, 61, 62].

In fact, an involvement of LH in pupil size controlling network has also been claimed in previous studies [59, 86, 87]. Therefore, LH may play a key role in investigating concealed functions of brain state-dependent pupil dynamics.

1.1.4 The role of anterior cingulate cortex in brain state regulation

The ACC is a part of the cerebral cortex commonly seen across different species [88, 89] (Figure 1.3). Several studies have reported that the ACC has a direct impact

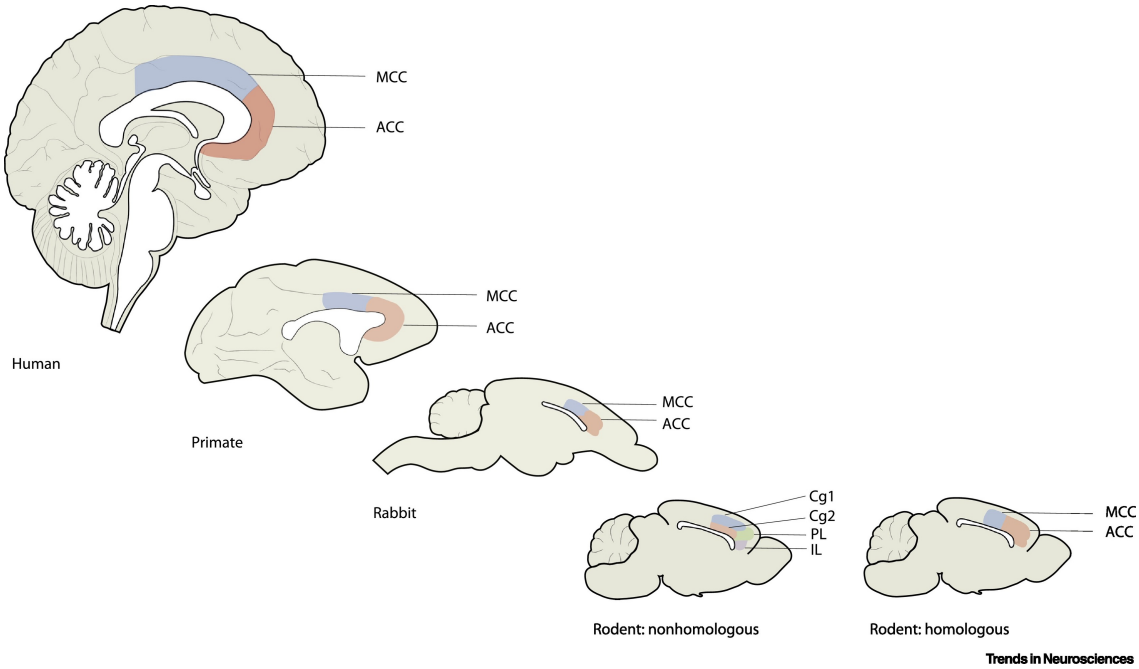

Figure 1.3 The location of the cingulate cortex across different species. ACC: anterior cingulate cortex, MCC: midcingulate cortex (Adapted from [88]).

on sustaining wakefulness [90] as well as modulating pupil dynamics [46]. In fact, the ACC is known to participate in the default mode network in rodents and humans [91]. During deep sleep and wakefulness, the ACC participates in the resting-state network differently [92], suggesting brain state-dependent activity of this brain region. For instance, Horovitz et al. [92] shows the involvement of the ACC in the default mode network decreased under deep sleep, which is also in agreement with a recent study reporting high participation of the ACC in the default mode network during wakefulness and N1 stage of NREM sleep compared to N2/N3 stages of sleep [24]. A neurochemical

study also shows that the bidirectional connections between the LC and ACC play an important role in sustaining wakefulness, as demonstrated by a research report showing that lesions of the ACC or denervation of catecholaminergic projections from the LC to the ACC resulted in reduced wakefulness [90]. Furthermore, the ACC is involved in pupil size modulation. As described in the above section 1.1.2, the LC plays a crucial role in regulating pupil size. However, changes in pupil size are not solely controlled by the LC. Instead, they are likely modulated by multiple brain regions, including the ACC [48, 63]. In fact, lesions of the ACC alter pupil regulation [93], and a recent study suggests that different modes of activity at the ACC relate to different brain states, measured as distinct brain correlation patterns with changes of pupil size, particularly involving noradrenergic regions in the brainstem [10]. These studies demonstrate that ACC activity can reflect pupil dynamics and this cortical area might be a key region for certain arousal-related brain state regulation.

1.2 Research techniques for brain state evaluation

The brain state is typically assessed behaviorally by eye-tracking and physiologically by various brain signal measures (e.g., electrophysiology and fMRI) to track the degree of wakefulness or the depth of sleep or anesthesia [5, 6, 9, 10, 12, 20]. Different brain states have been identified as unique neural signatures using electrophysiology (e.g., low frequency neuronal oscillations during sleep) [1], neuroimaging (e.g., different functional connectivity patterns between sleep and wakefulness) [24], and pupillometry (e.g., as relatively constricted pupil size during a low arousal level of both conscious and unconscious states) [9, 20]. Each method has technical strengths and limitations in recording brain signals (e.g., high temporal and low spatial resolution in electrophysiology, low temporal and high spatial resolution in fMRI), and therefore many studies combine multiple techniques to evaluate brain states [12, 20, 23, 94]. In animal research, both invasive and non-invasive in vivo measurements have been widely conducted to better understand the micro-scale details of neural activities and global brain functions such as brain connectivity, e.g., the combination of fMRI and optogenetics to stimulate a specific brain nucleus and assess the whole brain activity [95, 96]. In the following sections, different techniques used for brain state assessments are introduced.

1.2.1 In vivo electrophysiology

Extracellular in vivo electrophysiology is one of the most frequently used methods in animal studies to evaluate the brain state due to its high temporal resolution (less than a millisecond) [1]. This method records electrophysiological signals from the extracellular space of neurons at a region of interest (ROI) in the brain by inserting an electrode (e.g., tungsten metal electrode) and enables to investigate the neuronal activities of specific brain regions. The electrode inserted in the brain can capture a mixture of multiple neuronal features such as spikes (action potentials) and LFP. For brain state evaluation, LFP is widely evaluated since different oscillatory features of LFP represent distinct brain states (e.g., 1-4 Hz of slow oscillation during sleep/anesthetized states).

LFP signals in the cortex are generated by pyramidal neurons, lumped together in laminar morphology. The pyramidal neurons produce a current dipole between current sink and source. For instance, when synaptic inputs activate apical dendrites of a neuron, depolarization of the cell occurs, which creates stronger negative potentials outside the cell and positive potentials inside the cell since Na^+ ions flow into the cell. The currents flow from current sink (apical dendrites) towards the source (soma), and this movement creates the dipole, which can be detected by the electrode [97, 98]. In the cortex, a large dipole is detected due to the laminar morphology of pyramidal neurons [99]. However, the subcortical structures which lack laminar morphology can also generate LFP from focal excitatory input, which is large enough to be detected [100]. In fact, a large number of studies have reported LFP recording in other subcortical areas that lack of laminar structure such as thalamus [101, 102], substantia nigra [103, 104], striatum [105, 106], and LH [107–110].

Since the recorded electrophysiological signal contains various neuronal features as well as noise (e.g., 50 Hz electrical noise), raw data are first filtered into different frequency bands. Filtered signals between 1-5 kHz commonly represent local spiking activities within approximately 200 µm distance from the tip of electrode, known as multiunit activity (MUA). Filtered signals between 0-600 Hz represent local neuronal activities within approximately 2 mm distance from the tip of electrode, known as LFP. However, the ability to record single unit activity, MUA, and LFP depends on electrode impedance, tip size, shape, and material (e.g., electrode with lower impedance can detect signals from wider areas). In fact, the distance at which an electrode can detect LFP has been reported with various ranges between several micrometers and millimeters across multiple studies: the approximate recording distance of LFP is around 1 mm but can range between 0-3 mm [111–116].

The LFP signals are commonly filtered into different frequencies of oscillations such as delta (1-4 Hz), theta (4-7 Hz), alpha (7-14 Hz), beta (15-30 Hz), low gamma (30-60 Hz), and high gamma (60-100 Hz) bands [20, 117, 118]. Each LFP band has different biological meanings [118, 119]. For instance, during deep sleep and anesthesia,

slow waves are dominantly detected as the primary cortical activity in electrophysiology [1, 119, 120]. The primary brain wave switches to higher frequencies when the brain state transits from sleep/anesthesia to wakefulness [1, 9, 20]. Therefore, functional analysis of LFP is a well-established procedure to evaluate different brain states.

1.2.2 functional Magnetic Resonance Imaging

The measurement of blood oxygen level dependent (BOLD) signal fluctuations with fMRI is a well-established method to evaluate whole-brain activity non-invasively [121, 122]. The BOLD fMRI signal is governed by dephasing of proton spins in the blood vessels. When a cognitive event (e.g., triggered by a stimulus) occurs, synaptic inputs induce neuronal spike and neurotransmitters are released from neurons, indicating neuronal activities (Figure 1.4 (1)). The modulation of neuronal activities directly and indirectly trigger changes in hemodynamic responses such as blood volume, blood flow, and blood oxygenation due to neurovascular coupling (Figure 1.4 (2,3)). The combination of these changes can be detected by imaging sequences of MRI since the amount of dephasing of proton spins in oxygenated and deoxygenated blood is different (Figure 1.4 (4)). After a radio frequency (RF) pulse is transmitted from an RF coil, the magnetic resonance (MR) signal decays exponentially over the time due to the spin dephasing, characterized by the transverse relaxation time constant ($T_2{}^*$). The detected signal change is called BOLD fMRI response [123](Figure 1.4), which can be detected by $T_2{}^*$ weighted imaging sequences such as a gradient echo (GE) sequence. The 0.01-0.1 Hz range of BOLD-fMRI fluctuation is particularly known to indicate neural activity during the resting state [124, 125]. In contrast to the limited recording area in electrophysiology, i.e., limited to the number of recording sites on the electrode(s), fMRI provides a higher spatial resolution and can detect the whole brain activity. The fMRI signal comes from vascular-based responses, an indirect measurement of neuronal signals [123]. Previous studies confirmed that the fMRI signal shows high correlations with electrophysiology signals, a direct measurement of neuronal responses (See 1.2.5) [126, 127]. Thus, fMRI analysis is useful to investigate a wide range of brain functions (e.g., evaluations of

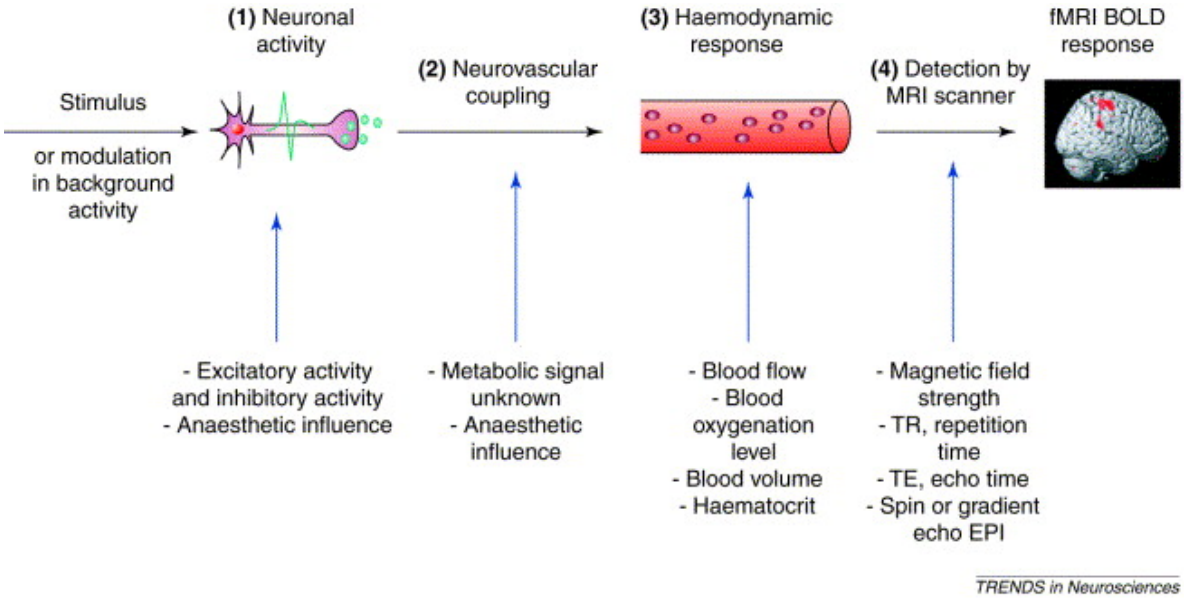

Figure 1.4 Physiological processes to provoke BOLD-fMRI responses (Reprinted from [123] with permission from Elsevier).

brain states, neurodegenerative diseases, or disorders of unconsciousness) with whole brain coverage [6, 128]. For instance, functional connectivity analysis from resting-state fMRI is a powerful technique to evaluate whole brain functions [129]. It evaluates the temporal correlation across different brain regions that express similar functional features. As a result of this connectivity analysis, different brain networks (e.g., default mode network) appear under distinct brain states of wakefulness, sleep, or anesthesia [6, 24, 25].

1.2.3 Calcium signal recording

Detection of calcium (Ca^{2+}) signal is a direct measurement of neural activities by observing changes of intracellular Ca^{2+} concentration in neurons through fluorescent signals [130, 131]. The concentration of Ca^{2+} ions in the extracellular space is maintained at a higher level than in the intracellular space at rest when there is no evoked neuronal activity. However, when the neuron fires (depolarized), Ca^{2+} ions in the extracellular space flow into the intracellular compartment since voltage-gated Ca^{2+} channels open. This increase of Ca^{2+} ions in the intracellular concentration can be used to measure

neuronal activities. In order to detect the neuronal activity in the brain using Ca^{2+} signals, genetically encoded fluorescent sensors such as green fluorescent protein-calmodulin fusion protein (GCaMP) (calcium sensors) [132, 133] are commonly used. The genetic information of GCaMP is delivered to a ROI by using a viral vector (e.g., adeno-associated virus (AAV)) [134]. When the target neurons that express fluorescent dyes are depolarized, Ca^{2+} signals can be detected by applying excitation light (e.g., wavelength between $480 - 510\,\text{nm}$ [135]) through one-/two- photon microscopy [136–138] or fiber photometry [131, 139]. Especially, fiber photometry for Ca^{2+} signal recordings is widely used in multi-modal fMRI recordings because an optical fiber is compatible with magnetic resonance imaging (MRI) [95, 139, 140]. Due to the noise-free nature of the optical fiber in the magnetic environment, the Ca^{2+} signals from fiber photometry are often used as an alternative method to LFP measurement for tracking neuronal activity [10] (Figure 1.5).

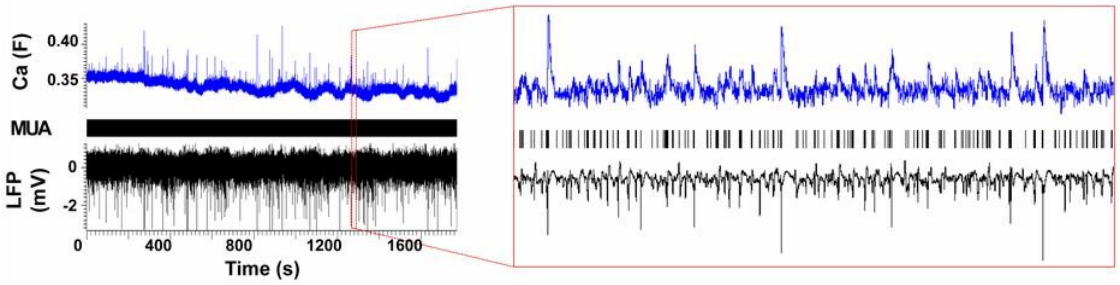

Figure 1.5 An example of simultaneous LFP, MUA, and Ca^{2+} signal recordings, showing strong correlations across different neuronal signal measures (Adapted from [10]).

1.2.4 Optogenetics

Optogenetics is a biological approach to stimulate neuronal cells through light [141, 142]. By experimentally manipulating neuronal activities, researchers can investigate the functional roles of cell-specific brain nuclei [143]. This method allows excitation (depolarization) or inhibition (hyperpolarization) of a specific type of neuronal cells, depending on how researchers set up the experimental design [143, 144]. In order to con-

trol neuronal activities, microbial rhodopsins, transmembrane ion channel proteins that sense light such as channelrhodopsin [145] and halorhodopsin [146], are integrated into membranes of neurons in a ROI in the brain using a viral vector (e.g., AAV and lentiviral vectors) [143, 147, 148]). The genes that produce rhodopsins are linked with other cell-specific promoters, which can be active in a specific cell type only such as neurons [144]. Therefore, cell-specific activation becomes possible with this technique. These light-sensitive ion channels in the transfected neurons open when they receive a specific wavelength of light, e.g., 473 nm wavelength of blue light for channelrhodopsin-2 (ChR2) activation [144]. This opening of channels causes an influx of positively charged ions such as Na^+ and Ca^{2+} or negatively charged ions such as Cl^- into the cell. This chemical movement induces depolarization or hyperpolarization of the neurons. In research to investigate brain states, optogenetics is widely used to activate arousal-regulating neurons such as orexin and noradrenergic neurons and alter the brain state experimentally. For example, activation of orexin neurons in the LH triggers a brain state transition from NREM sleep to wakefulness [74]. In parallel with brain state transition, behavioral modulation such as pupil size is commonly monitored; for example, optogenetic activation of noradrenergic neurons in the LC or serotonergic neurons in the dorsal raphe nucleus induces pupil dilation [61, 149]. Therefore, optogenetics is a powerful tool to experimentally manipulate brain states and understand the function of brain nuclei on brain state regulation.

1.2.5 Correlations across different recording techniques

Logothetis et al. [126] first reported that LFP is in direct relationship with BOLD signals in fMRI. However, the correlation between LFP and BOLD fMRI can be positive or negative [127]. Although the mechanism that causes these variations of the LFP-BOLD coupling is not fully understood, the correlation between LFP and BOLD signals depends on several factors such as brain regions, LFP frequency ranges, and brain states [150–152]. It has been reported that higher LFP frequencies (e.g., gamma band) are more positively coupled with BOLD while low LFP frequencies (e.g., delta band) tend to be

more negatively coupled [127, 150], although these positive and negative correlations vary across different brain regions [151]. Schölvinck et al. reported that positive correlations between low frequency (2-15 Hz) LFP power and fMRI signal could be observed across wide regions of the cerebral cortex such as frontal, parietal, and occipital lobes [153]. Conner et al. also reported a similar observation showing that the delta band is positively correlated with the global BOLD signal across the cortex, however, regional differences were observed, including some anti-correlations in the middle and superior temporal gyrus [151]. Additionally to these studies, the delta band power and BOLD signals were found to be negatively correlated in the prefrontal cortex [154]. Subcortical areas such as the striatum also exhibited negative correlations between LFP delta band power and BOLD signal fluctuations [155]. Even within the same area, correlation features of fMRI with neuronal signals vary across different temporal scales [152, 153]. For instance, correlation values between LFP and fMRI are low during an eye open state but high during an eye closed state within the same monkey [153], demonstrating brain state-dependent coupling features across multi-modal recordings.

Simultaneous monitoring of eye responses and brain signal measures (e.g., electrophysiology and fMRI) can also be used to evaluate brain states [9, 12, 20, 23]. Technical constraints of multi-modal neuroimaging methods (e.g., interference of fMRI signals with electrodes and/or limited temporal resolution in fMRI and spatial resolution in electrophysiology signal recordings) often lead to a lack of understanding about functional roles of different brain regions on brain state regulation, and pupillometry can add further details of brain states upon evaluation. Using pupillometry, the brain state has been studied in rodents during wakefulness [9], sleep [20], and anesthesia [10]. Similar to the variations of correlations between electrophysiology and fMRI measurements across different temporal scales, correlation patterns between pupil size and brain signal measures also vary depending on brain states [10, 20, 23]. For instance, low frequency LFP power exhibits strong negative correlations with pupil size oscillations during slow-wave sleep but weaker correlations during wakefulness [20]. Overall, these features of varied correlation across multi-modal measurements can be utilized as a useful approach to

elucidate complex brain state mechanisms.

1.3 Project aims

Pupil size has been used as an index to evaluate brain states over the last decade. Both brain states and pupil size are mainly regulated by subcortical and brainstem areas, suggesting an overlap of regulatory pathways. For instance, optogenetic manipulation of arousal- and pupil- regulating nuclei in the brainstem causes both brain state and pupil size modulations. Despite a strong link between pupil size and neuronal activities of multiple arousal-regulating regions, the correlation feature diversifies under different brain states or among different brain regions. This observation suggests an involvement of up-regulatory regions such as LH and ACC that govern pupil-regulatory circuits but also modulate brain states. Investigating these up-regulatory regions may illuminate attributes of brain state and pupil size interactions. The purpose of this dissertation is to provide a deeper understanding of neuronal mechanisms on brain state and pupil size regulations through investigations of the ACC and LH using multi-modal brain signal recordings with pupillometry under three main experimental protocols:

1. Understanding brain state-dependent correlations of pupil size with the whole brain using pupillometry, fMRI, and Ca^{2+} signal recordings, described in Chapter II.

2. Evaluating brain state-dependent pupil dynamics based on functional interactions between pupil size and LH/ACC activities using pupillometry, electrophysiology, fMRI, and Ca^{2+} signal recordings, described in Chapter III.

3. Manipulating pupil size and brain states experimentally through direct activation of the LH using pupillometry, electrophysiology, and optogenetics, described in Chapter IV.

2 Chapter II: Multi-modal fMRI measurements for brain state assessments

2.1 Introduction

All work in this Chapter II has been already published in Proceedings of the National Academy of Sciences (PNAS) in 2020 [10].

Neuronal oscillation below 0.1 Hz in a resting state is involved in arousal fluctuation [12, 156]. Using multi-modal brain imaging and behavioral measurements such as fMRI, electrophysiology, and pupillometry, investigation of this oscillatory feature can also reveal neuromodulatory attributes of distinct brain states and the transition between them [5, 140, 157–159]. Especially, low frequency fMRI BOLD fluctuation (0.01-0.1 Hz) reflects neural activity at the rest state [124, 125]. From the acquired fMRI data, functional connectivity is commonly calculated for evaluating different brain states, cognitive functions or clinical disorders [24, 160–162]. Especially, brain state transitions/fluctuations under wakefulness, sleep, or anesthesia are often evaluated from resting-state fMRI signals, showing distinct functional connectivity patterns among different brain states [12, 24, 25, 91, 153, 163, 164]. A previous animal study reported that simultaneous fMRI and Ca^{2+} astrocytic/neuronal signal recordings could indicate brain state transitions under anesthesia [140]. Furthermore, oscillation of these fMRI signals also correlates with dynamics of pupil size across temporal scales, and these correla-

tions represent arousal fluctuations and vary depending on the underlying brain state [12, 23, 165]. However, functional brain networks of arousal state transitions are not fully well-known.

Changes in pupil size are associated with brain state modulations and also neuronal activity of arousal-regulating cortical (e.g., the ACC) and brainstem (e.g., noradrenergic neurons in the LC) regions [9, 20, 45, 46, 48, 166]. For instance, pupil size appears to be more constricted when the cortex is in a slow-wave state but more dilated when the cortex is in a desynchronized state [9]. Under an unconscious state of sleep or anesthesia, pupil size also changes spontaneously across different temporal scales [16, 17, 20]. However, correlations between pupil size and neuronal activity of arousal-regulating regions such as the ACC and LC often vary across different recording trials [46], possibly due to the influence of brain state differences [47].

Although these various correlations are often studied in electrophysiology with pupil size [9, 20, 45, 46], the correlation features at the global brain level have not been clearly understood. By evaluating trials that show brain-state differences, unique correlation features between pupil size and global brain activity may arise depending on different brain states. In Chapter II here, the aim of study was first to establish a platform to investigate pupil size, whole-brain BOLD fMRI, and Ca^{2+} signals from GCaMP-mediated fiber photometry in anesthetized animals. By utilizing Ca^{2+} signals as a tool to distinguish different brain states, we demonstrated brain state-dependent correlations between pupil size and whole-brain BOLD fMRI signals.

2.2 Methods

2.2.1 Subjects

Ten Sprague Dawley rats (Strain: Crl:CD(SD), Sex: Male, Charles River Laboratories, Sulzfeld, Germany) were used in all experiments. The age of rats was 4-5 weeks at the start of the experiment when the intracranial virus-vector injection was conducted. The age of rats at the time of fMRI experiments was 3-6 months.

2.2.2 Stereotaxic injection of viral constructs

Transfection of viral constructs was conducted in 4-5 weeks old rats for virus expression of calcium indicator. The animal was anesthetized with oxygen-enhanced air (30 % oxygen) mixture containing 5.0 % isoflurane in an induction box. The anesthetized animal was placed in a stereotactic frame in a prone position. The animal's head was secured to a stereotaxic frame with earpieces and a bite bar. Animals were kept being anesthetized with 1.5-2.5 % isoflurane via nose cone. The depths in anesthesia was examined by the absence of pedal withdrawal. The body temperature of the animal was monitored and controlled to be at 37-38 °C by a heating pad. A small amount of sterile ophthalmic ointment was placed in each eye to protect them from drying. Hairs above the surgical area were shaved first. Then, the area was cleaned with 70 % alcohol and iodine. A sagittal midline incision was made to expose the skull. In order to inject a viral construct, a craniotomy was performed on the surface of the skull above the ACC based on the rat brain atlas from Paxinos and Watson [167]. The viral construct, GCaMP(AAV5.Syn.GCaMP6f.WPRE.SV40), was injected at the ACC (A/P= +1.20 mm, M/L= +0.50 mm, D/V= -1.50 mm) with the portion of 600 nL at a rate of 200 nL/min. After the injection is completed, the craniotomy was closed with sterile wax. It the end, the skin was sutured and disinfected.

2.2.3 Surgical preparation for measurements of fMRI and calcium signals

Prior to the fMRI experiments, animal surgeries were performed to ventilate the animal, provide intravenous anesthetics, monitor blood pressure, and record calcium signals. The animals were first anesthetized in a gas mixture containing 5.0 % isoflurane in an induction box. The anesthetized animal was supinely placed on a custom-made board for tracheal intubation. Animals were ventilated at 60±1 breaths per minute with 2.0 % isoflurane and oxygen-enhanced air (20 % oxygen) via tracheal intubation on a table with a heating pad. The body temperature of the animal was kept between 37-38 °C. The animal's hair on the groin of the right hind limb was shaved. The shaved area was disinfected, and a small surgical incision was made on the disinfected area. Surgeries for femoral artery and vein cannulation were performed using polyethylene tubes (PE-50) through this incised area. Once cannulation was done, the incised area was sutured and closed. Then, the animal was pronely placed on a stereotactic device for optical fiber insertion in the cortex. The animal's head was secured with earpieces and a bite bar on the stereotactic device, and its head hairs were shaved. The shaved area was cleaned with 70 % alcohol. A sagittal midline incision was made on the disinfected area to expose the skull. A craniotomy (< 1 mm diameter) was performed on the surface of the skull above the ACC (A/P= +1.20 mm, M/L= +0.50 mm). An optical fiber (200 µm diameter) was then inserted into -1.50 mm depth from the surface of the brain where GCaMP was expressed. The optical fiber was fixed to the skull with cement. Once the fiber was stably attached, the earhole was filled with a fluoride paste. Finally, an intravenous infusion of alpha-chloralose anesthesia (a bolus of ($\backsim$ 80 mg/kg) was conducted through the catheter, previously inserted in the femoral vein. Simultaneously, inhalation of isoflurane was stopped. The animal was moved to the MRI scanner and secured on a custom-made bed. A heating pad was used to maintain the body temperature of the animal at 37 °C. This temperature was monitored through a rectal probe. End-tidal CO_2 was also monitored through the intubation tube. One catheter from the femoral artery was connected to a blood pressure recording device (Biopac 150 system), and the

other catheter from the femoral vein was connected to an infusion pump, both located outside of the scanner. Through this catheter in the femoral vein, alpha-chloralose anesthesia ($\backsim$ 25 mg/kg/h) and pancuronium ($\backsim$ 2 mg/kg/h) were provided throughout the experiment.

2.2.4 Data acquisition of brain images and fMRI signals

A 14.1 T / 26 cm magnet (Magnex) with an Avance III console (Bruker) was used to acquire all structural and functional images. A custom-made transceiver surface coil ($\backsim$ 2x2.7 cm), connected to the scanner, was placed on the head of the animal for excitation and reception of signals. To acquire fMRI data, 3D echo planar imaging (EPI) sequence was used for 15 min and 25 s of scan time (925 volumes) in each trial with parameters of 400x400x600 µm resolution, 48x48x32 matrix size, 12.5 ms echo time (TE), and 1 s repetition time (TR) with the whole brain coverage. To acquire anatomical brain images for image registration purpose, the rapid acquisition with relaxation enhancement (RARE) sequence was used with parameters of 600 µm slice thickness, 128x128 matrix size, 150 µm in-plane resolution, 8x RARE factor, 32 slices, 9 ms TE, and 4 s TR.

2.2.5 Extraction of pupil diameter in pupillometry

A video camera with 30 mm x 21 mm x 15 mm dimension and 10 mm focal length of the lens was used to capture the pupil size during the fMRI experiment. Additionally, an infrared LED light (wavelength: 880 nm) was placed next to the video camera to increase the contrast of pupil image since the video was recorded in a dark environment. Honestech VHS to DVD (version 2.0) was used to record the video with the following parameters: 29.97 frames/second, 24 bits per pixel in RGB24, and 240 x 352 pixels. To measure pupil size from the acquired videos, the DeepLabCut toolbox [168, 169] was used. Four points were diagonally marked on the edge of pupil from 1330 frames of 73 videos (Figure 2.1a). Then, an artificial network was trained based on these labeled frames using k-means clustering. This trained network computed the four points of all frames from all 73 videos (Figure 2.1b, c).

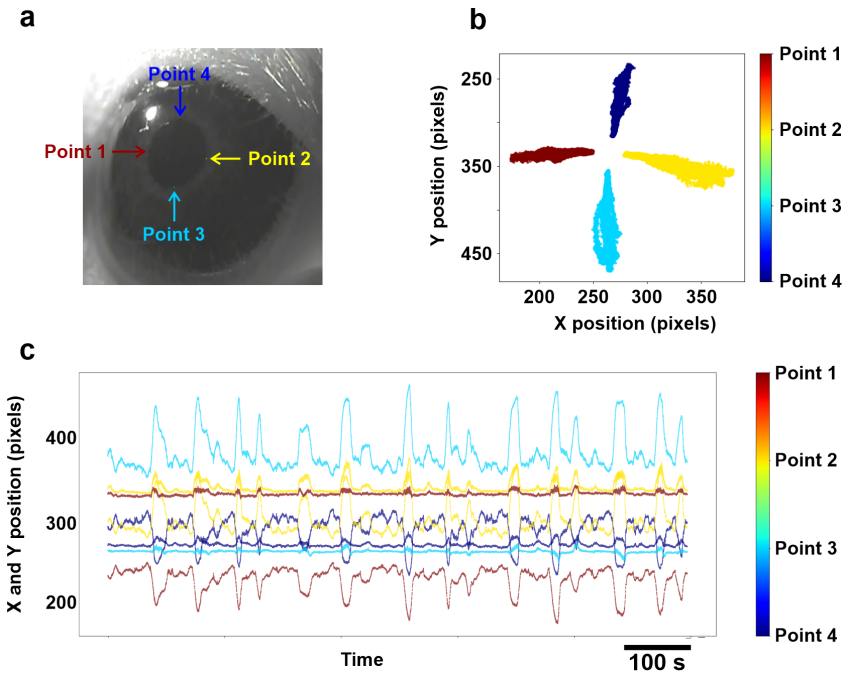

Figure 2.1 A representative example of pupil size extraction in DeepLabCut. a) four points were labeled on the edge of pupil. b) The coordinates of four points from all frames (15 min) in one trial. c) The time course of x and y coordinates for all four points across 15 min of recording.

From the extracted four points, the pupil size (in pixels) was calculated with the following equation 2.1 .

$$d_{\text{pupil}} = \frac{\sqrt{(x_2 - x_1)^2 + (y_2 - y_1)^2} + \sqrt{(x_4 - x_3)^2 + (y_4 - y_3)^2}}{2} \tag{2.1}$$

2.2.6 Data acquisition of calcium signals

The Ca^{2+} signal (GCaMP) at the ACC ($A/P = +1.20\,\text{mm}$, $M/L = +0.50\,\text{mm}$, $D/V = -1.80\,\text{mm}$) was acquired using fiber photometry. The optical fiber (200 µm diameter, FT200-EMT, Thorlabs) was connected between the ACC and a light path setup. The analog signals from the light path setup were converted to digital signals and recorded in Biopac 150 system at the sampling rate of 5 kHz.

2.2.7 Data analysis of calcium signals

In order to evaluate the change of Ca^{2+} fluorescent signals, the acquired signals were first normalized with the following equation:

$$F_{change} = \frac{\Delta F}{F} \tag{2.2}$$

Changes in fluorescent signals are depicted as F_{change}, the fluorescent signal of a certain time point as ΔF, and the initial fluorescent signal as F.

For extracting power of Ca^{2+} signals, spectral analysis was performed using the wavelet decomposition with a specification of 0.5-10 Hz frequency band and 2 s sliding window from the raw data of Ca^{2+} signals. From the outcome of spectral analysis, the Ca^{2+} spectral power was extracted between 0.5-10 Hz. The extracted Ca^{2+} power was filtered with the passband of 2-3 Hz, using the filtfilt function of Matlab (R2020b, The MathWorks Inc., Natick, Massachusetts, USA).

bandpass filtered with passband

2.2.8 Data analysis of fMRI signals

All functional data from each animal was first registered to the anatomical scan of the same animal using the AFNI software package [170]. All anatomical RARE scans across animals were registered to one RARE scan as a template to pair all data of different animals using the 3dAllineate function of AFNI. Then, all EPI data were registered using these transformation matrices. The preprocessed functional data were filtered between 0.005 and 0.15 Hz to perform further fMRI analysis such as correlation analysis between pupil size and fMRI signals.

2.3 Results

2.3.1 Simultaneous acquisition of fMRI, calcium signals, and pupil size

We first established a multi-modal fMRI setup to investigate the brain state-dependent relationship between pupil size and whole brain activities: simultaneous recordings of whole-brain fMRI signals, fiber photometry calcium signals, and pupil size (Figure 2.2).

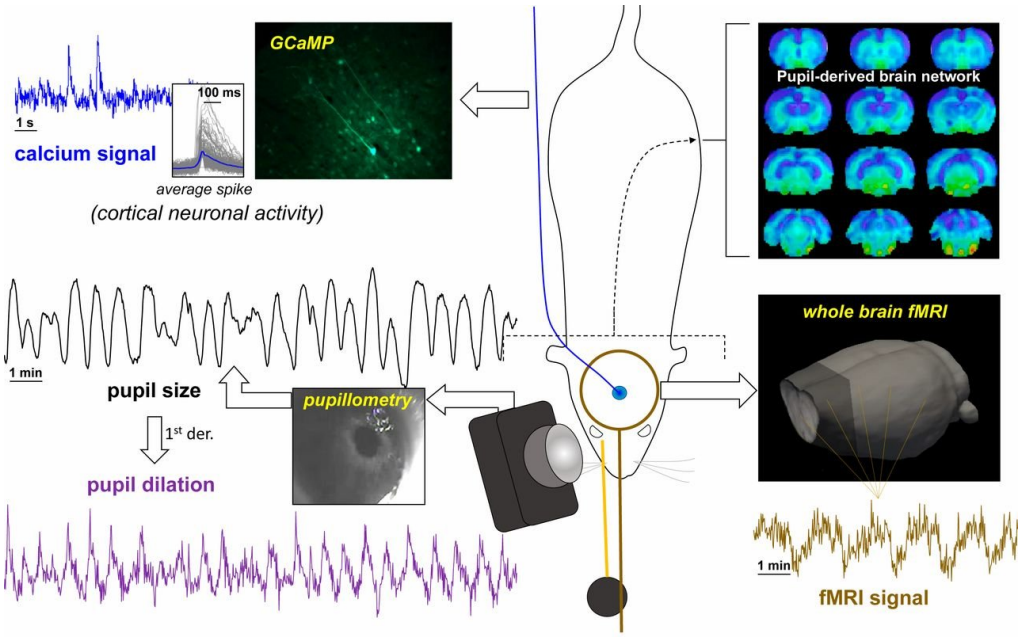

Figure 2.2 The experimental setup for multi-modal fMRI recordings. The diagram describes the calcium signal from the ACC (expressing GCaMP fluorescence), pupil size fluctuations, 1st derivative of pupil size time course, the whole brain fMRI signal, and the correlation between the fMRI and pupil size (Adapted from Pais-Roldán et al., 2020) [10].

The pupil size was recorded as a video inside of the MRI scanner for 15 min in each trial. In a resting state under anesthesia, the pupil spontaneously dilated and constricted across time (Figure 2.3a). In line with pupil size fluctuations, the power of neuronal calcium signals from ACC, expressing GCaMP fluorescence (Figure 2.2), also showed coherent fluctuations, most robustly observed between 2-3 Hz in the power spectrogram (Figure 2.3e, f). At the same time, the fMRI signal also fluctuated similarly

with changes of pupil size (Figure 2.2). In particular, the 1st derivative of pupil size time course (Figure 2.3b), indicating the change of pupil size (positive value for the change when the pupil starts dilating and negative values when constricting), showed global negative correlations with fMRI signals in the cortex but positive correlations in brainstem regions (Figure 2.3c).

These results indicate that the brain state fluctuates in a resting state even under anesthesia, and fMRI signals are tightly linked with the brain state dynamics.

2.3.2 Correlations of fMRI signals and pupil size

To investigate the correlation between pupil size and whole-brain functional data, voxel-wise correlation analysis was performed. The resting-state fMRI signals showed global negative correlations with pupil size fluctuation (Figure 2.4a). In particular, these negative correlations were more robust in the cortical and thalamic regions, including the cingulate cortex (Figure 2.4c). Interestingly, when the 1^{st} derivative of pupil size fluctuation was correlated with all voxels of fMRI signals, global negative correlations appeared in the cortical and thalamic regions. Similar to the pupil size fluctuations (Fig. 2.4b, c). However, positive correlations emerged in the brainstem regions, most robustly in A5 pontine tegmentum (Figure 2.4b, c, d).

2.3.3 Brain state-dependent correlations of fMRI signals and pupil size

To investigate the brain state-dependent effect on the correlations between whole-brain fMRI signals and pupil size, we evaluated Ca^{2+} signals from the ACC. The strongest wave of Ca^{2+} signal was found between the 2-3 Hz (Figure 2.5c). This result was also consistently observed in electrophysiology assessment (Figure 2.5b, g). These analyses indicated that electrophysiology and Ca^{2+} signal recordings were complementary to each other. The cross-frequency analysis demonstrated that the power of 2-3 Hz Ca^{2+} signals coupled with the baseline fluctuation (0-0.5 Hz) of Ca^{2+} signals in

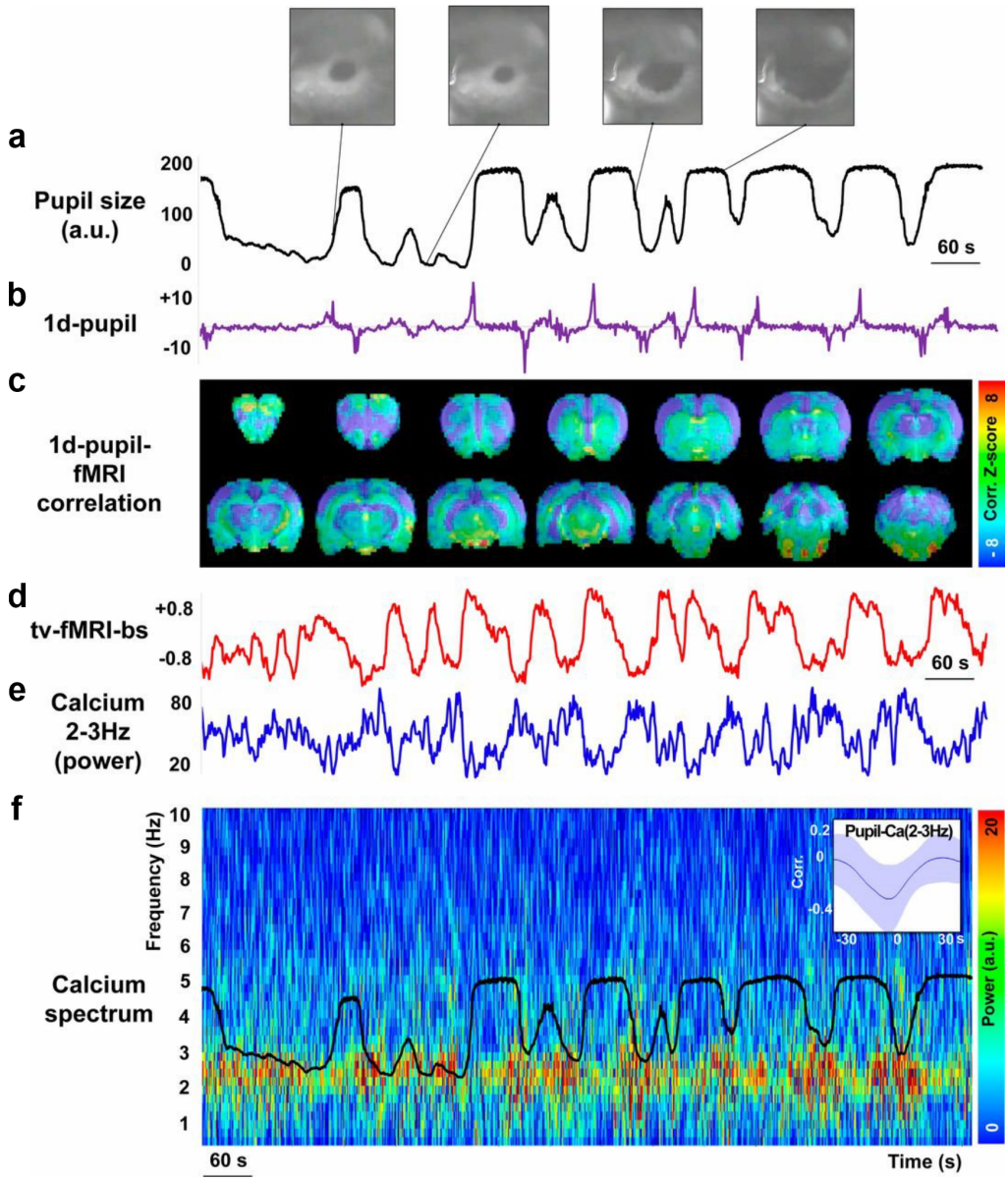

Figure 2.3 A representative example of temporal dynamics in pupil size, fMRI signal, and Ca^{2+} signal. a) Pupil size fluctuation across 15 min of a resting state. b) The 1st derivative of pupil size. c) Correlations between 1st derivative of pupil size and the whole fbrain regions. d) The trace of time-varying fMRI-inferred brain state (tv-fMRI-bs), e) The power of Ca^{2+} signals between 2-3 Hz. f) Power spectrogram of Ca^{2+} signals along with pupil size fluctuations (black trace) (Adapted from Pais-Roldán et al., 2020) [10].

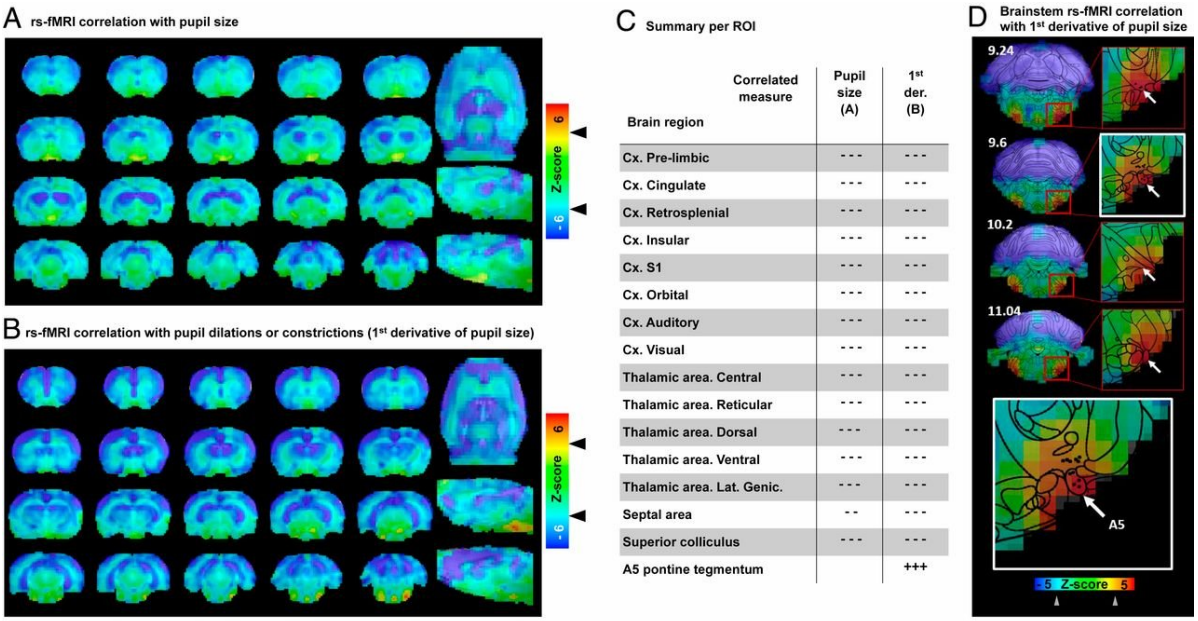

Figure 2.4 Voxel-wise correlations between resting-state fMRI signals and pupil size. a) The whole-brain voxel-wise fMRI correlation map with pupil size fluctuation and b) 1st derivative of pupil size fluctuation) across all trials ($n = 71$, 10 animals). c) A table showing statistical significance of correlations between specific brain regions and pupil size fluctuation and 1st derivative of pupil size fluctuation. d) The brainstem fMRI correlation map with 1st derivative of pupil size fluctuation. White arrows indicate the noradrenergic cell group 5 (A5) region *Note*: [--] $p < 0.005$, [+++]&[---] $p < 0.001$ (Adapted from Pais-Roldán et al., 2020) [10].

39.4 % of trials (n= 28) but did not in the rest of 60.6 % of trials (n= 43; Figure 2.5h). Interestingly, whole-brain fMRI correlation map showed that the 1st derivative of the pupil size was positively correlated with fMRI signals in the brainstem, particularly A5 regions, among trials when the 2-3 Hz and baseline Ca^{2+} signal did not couple (Figure 2.5i). However, these robust positive correlations in the A5 regions were not observed among 2-3 Hz/baseline coupled trials.

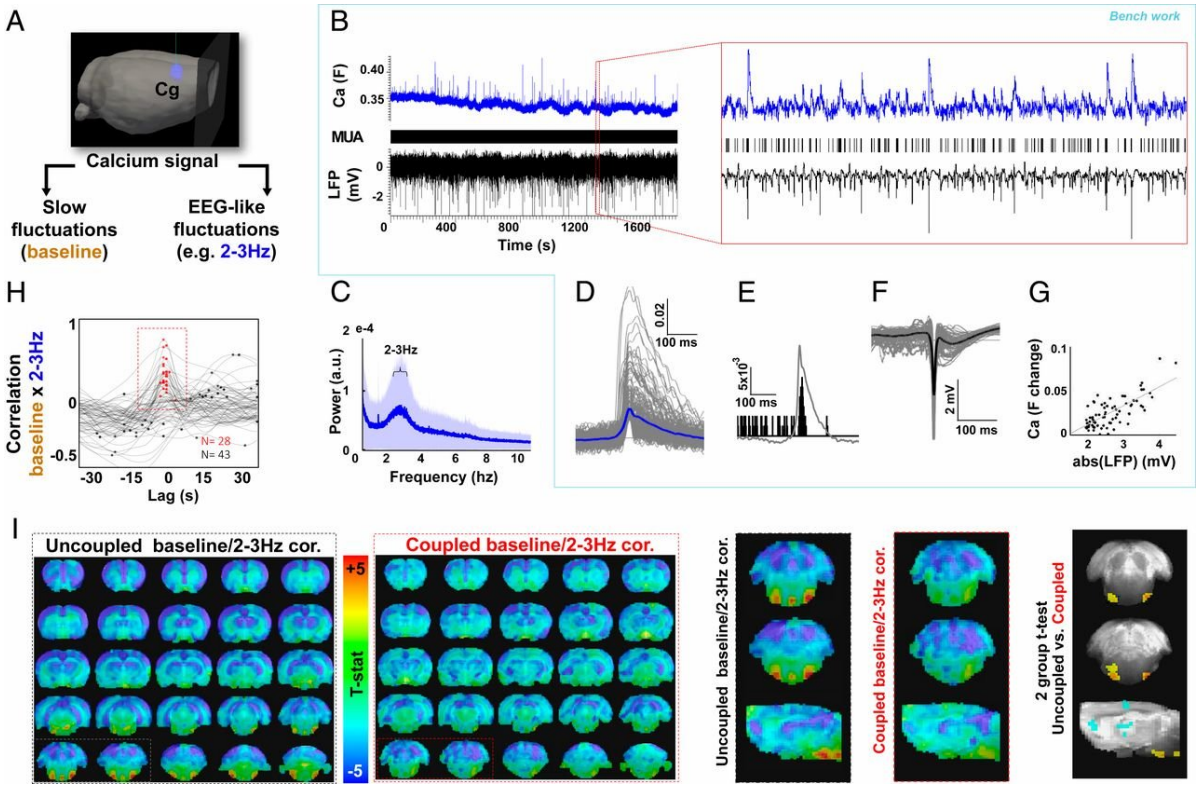

Figure 2.5 Brain state-dependent correlations of fMRI signals and pupil size based on Ca^{2+} signals. a) A schematic showing that the Ca^{2+} signal was separated into 2-3 Hz and slow fluctuations. b) An example of simultaneous LFP and Ca^{2+} recordings for 30 min. The enlarged picture shows 25 s of the time window. c) Power spectral density of Ca^{2+} signal from all animals (n=64, 10 animals). d) Each peak of Ca^{2+} signals (grey trace) and its average (blue trace) within a trial. e) Averaged MUA at each peak of Ca^{2+} signals. f) Each peak of LFP signals (grey trace) and its average (black trace). g) Linear correlation of Ca^{2+} and LFP signals. h) Cross-frequency coupling analysis between baseline (0-0.5 Hz) Ca^{2+} signals and 2-3 Hz power of Ca^{2+} signals. i) Voxel-wise fMRI correlation map with 1st derivative of pupil size from 2-3Hz/baseline uncoupled (left) and coupled trials (right), as well sagittal and coronal views of brainstem regions (Adapted from Pais-Roldán et al., 2020) [10].

2.4 Discussion

In the work of Chapter II, we measured fiber photometry neuronal Ca^{2+}, whole-brain BOLD fMRI signals, and pupil size simultaneously to identify brain state-dependent correlations between pupil size and whole brain activity in anesthetized animals. Changes in pupil size (the first derivative of the time course of pupil size) were negatively correlated with the whole-brain fMRI signals globally but positively with noradrenergic A5 regions in the brainstem in a trial-specific manner. The positive correlation in the A5 region appeared only under a specific brain state that showed decoupling between fluctuations of the baseline Ca^{2+} signal (below 0.5 Hz) and 2-3 Hz Ca^{2+} power in cross-frequency analysis. These results demonstrate that distinct correlation features between pupil size and brain activity are observable under different brain states of anesthesia, particularly in pupil- and arousal- related neuromodulatory regions.

Fluctuation of pupil size is associated with dynamics of cortical activity, presenting changes in the degree of arousal during wakefulness, sleep, or anesthesia in animals [9, 16, 17, 20]. In consistency with these studies, our results also demonstrated that pupil size spontaneously fluctuated (dilation and constriction of pupil size recurring) during 15 min of resting state under anesthesia (Figure 2.3a, b). Furthermore, the changes of pupil size also coincided with the fluctuation of low frequency Ca^{2+} power at the ACC (Figure 2.3f), similar to a previous sleep study demonstrating that pupil size oscillation correlates with power fluctuation of low frequency LFP bands under unconsciousness [20].

Our observation indicated that the changes of pupil size were also associated with the fluctuations of BOLD fMRI signals (Figure 2.4a). The global BOLD fMRI signal was negatively correlated with both the pupil size and the first derivative of pupil size, more robustly in the cortical and thalamic regions (Figure 2.4a, b), similar to a previous report demonstrating that the cortical resting-state fMRI signal is negatively correlated with arousal fluctuation of eye movements (opening and closing of eyes) [12]. Despite these global negative correlations, the first derivative of pupil size was positively correlated with the noradrenergic A5 region (Figure 2.4c, d). The noradrenergic neurons in the

A5 region project to other arousal-regulating regions such as the parabrachial nucleus and periaqueductal gray [171, 172]. Neuronal activity of the A5 region is known to vary under different brain states of unconsciousness [173], and their neurons project to other arousal-regulating regions such as the parabrachial nucleus and periaqueductal gray [171, 172], suggesting that the A5 activity may possibly be involved in regulating brain states and pupil size. This strong positive correlation in the A5 region appeared only with the first derivative of the pupil size change, e.g., changes in dilation or constriction, rather than with the direct fluctuations of the pupil size (Figure 2.4a, b). This fact suggests that A5 activity may contribute more to brain state transitions instead of brain state maintenance, although further investigations are necessary to understand the link between pupil size and A5 activity, e.g., direct activation of A5 neurons using optogenetics and measurement of pupil size concurrently.

The GCaMP6f-mediated neuronal Ca^{2+} signal from fiber photometry represents comparable neuronal activity from the electrophysiology recording (Figure 2.5b, e, g), consistent with the previous studies [140, 174]. Therefore, simultaneous measurements of Ca^{2+} and BOLD fMRI signals can be a useful setup to evaluate state-dependent whole brain activity. From our acquired Ca^{2+} signals, we observed that the baseline Ca^{2+} signal fluctuation (below 0.5 Hz) coupled with the 2-3 Hz Ca^{2+} power in 40 % of trials but decoupled in the rest of 60 % in the cross-frequency analysis (Figure 2.5h), suggesting the presence of distinct brain states since the coupling features of low- and high- frequency bands switch in a brain state transition [11]. Interestingly, the positive correlation between pupil size and the A5 region emerged only in trials where baseline Ca^{2+} fluctuation uncoupled with 2-3 Hz Ca^{2+} power (Figure 2.5i), demonstrating that coupling features of pupil size and A5 activity are brain state-dependent.

As discussed in Chapter I, the classification of distinct brain states is still controversial, especially in the context of anesthesia. However, brain state transitions clearly appear under anesthesia, coinciding with neuronal signal and/or pupil size changes [11, 16–19]. These fluctuations also appear under sleep or wakefulness in the same manner [9, 20]. These different brain states are often distinguishable from exploratory

analysis across cross-scale recording techniques, e.g., correlations between pupil size and electrophysiology/fMRI signals [12, 20, 23]. Although we have to take into account the fact that interpretation of brain state fluctuations differs from ones without anesthetics, our study here could distinguish different correlation patterns between changes of pupil size and BOLD fMRI fluctuation under distinct brain states of anesthesia.

In summary, this study reported unique coupling features across the fields of fMRI, Ca^{2+} signal, and pupil size responses. We demonstrated the brain state-dependent positive correlation features between changes of pupil size and A5 activity in fMRI signal that varies depending on coupling features of baseline Ca^{2+} signal fluctuation with 2-3 Hz Ca^{2+} power. Although further investigation of the coupling mechanisms in brain states without anesthesia might be necessary for future research, this study can contribute to understanding brain state-dependent pupil regulation in a whole brain perspective.

3 Chapter III: Evaluation of the brain state through lateral hypothalamic activities

3.1 Introduction

All work in this Chapter III has been already posted in bioRxiv (an open access preprint server) in 2021 [175]. The work can be published in a peer-reviewed journal in the future.

Although Chapter II provides a solid platform to evaluate the brain-state dependent correlations between pupil size and regional/whole brain activities, the study still lacks of evaluation to understand more specific brain states such as an indication of different arousal levels and compare the attributes with electrophysiology. One possible approach for brain state evaluation can be to investigate the interactivity between dynamics of pupil size and LH/ACC signals since interactions between pupil dynamics and fluctuation of cortical electrophysiology amplitudes appear with negative correlations during a low arousal state of unconsciousness [20]. As mentioned in Chapter I, multiple subcortical and brainstem regions, including the LH and LC, are involved in regulating the brain state [39, 49, 50, 59]. Noradrenergic interactions between the LC and ACC especially play an important role in adjusting pupil size and different degrees of arousal such as wakefulness and various sleep stages [39, 45, 50, 63, 90, 93]. This attribute indicates that the ACC's activity can reflect pupil dynamics and might be key

to evaluate arousal-related brain states. Although the contribution of the LC-ACC noradrenergic projection to brain state and pupil size regulations is vital, other subcortical regions and neuronal projections are also involved in the change of brain state and pupil size by interacting with ACC [46, 48, 63]. In fact, neuronal activity of ACC correlates positively and negatively with pupil size changes depending on trials [46]. Hence, a more convoluted mechanism involving subcortical regions could be involved in pupil size and brain state changes.

One key region that regulates pupil size and brain states is the LH since neuronal discharges of different cell types in the LH mediate distinct brain states [65, 74, 79, 80]. Moreover, the LH contributes to pupil size regulation through neural circuits to the LC and EWN [59, 86, 176]. Interestingly, the LH also contains neuronal projections to the ACC [84], but functional attributes of the ACC and LH relations have not been thoroughly understood especially in regard to the roles of concurrent brain state and pupil size regulations. Hence, the aim of Chapter III is to evaluate brain state-dependent variations of correlation features between pupil size and whole brain activity by investigating the interaction between ACC and LH activities.

In this study, we performed two independent multi-modal brain signal recordings in anesthetized animals to evaluate brain state-dependent pupil dynamics: 1) simultaneous measurements of pupil size and electrophysiological signals at the ACC and LH, 2) simultaneous measurements of pupil size, GCaMP-mediated Ca^{2+} signals at the ACC, and whole-brain BOLD fMRI. In the multi-modal electrophysiology study, we first detected two phases of correlation patterns (positive and negative correlations) between dynamics of pupil size and LFP power at the ACC and LH across recording trials. To further investigate in-depth features of these positive and negative correlation trials, we conducted cross-frequency analyses and characterized two different brain states. For instance, higher phase-amplitude coupling values (coupling of delta phase with theta/alpha/beta/gamma amplitude) from the ACC appeared in trials that showed negative correlations between pupil size and LH LFP delta power, indicating a low arousal state within unconsciousness. In the multi-modal fMRI study, a consistent

distinction of correlation features between dynamics of pupil size and Ca^{2+} power in the ACC was identified by looking at the correlations between pupil size and LH fMRI signal fluctuations, characterizing analogous brain states from LH activity between fMRI and electrophysiology recordings. This study portrayed unique distinction of brain states under anesthesia based on LH-ACC circuit-specific coupling features with pupil size.

3.2 Methods

3.2.1 Subjects

Nine Sprague Dawley rats (Strain: Crl:CD(SD), Sex: Male, Charles River Laboratories, Sulzfeld, Germany) were used for multi-modal fMRI experiments and nine Sprague Dawley rats for multi-modal electrophysiology experiments. The age of rats at the time of experiments was between 3-6 months.

3.2.2 Surgical procedures for multi-modal electrophysiology experiments

All surgical details for cannulation of the femoral artery and vein are described in Chapter II (see 2.2.3 Method) since the same operations were performed in this experiment. Once the cannulation surgeries were complete, the animal was moved to a stereotactic device pronely for electrode insertion in the ACC and LH. The animal's head was fixed on the stereotactic device with earpieces and a bite bar, and then the head hairs were shaved. The shaved area was cleaned with 70 % alcohol. A sagittal midline incision was made on the cleaned area to expose the skull. A craniotomy (< 1 mm diameter) was performed on the surface of the skull above the ACC (A/P= +1.20 mm, M/L= +0.50 mm) and LH (A/P= -3.20 mm, M/L= +1.50 mm). A tungsten electrode (1 MΩ resistance; FHC Inc) was inserted into -1.50 mm depth above the ACC and -7.80 mm above the LH respectively from the surface of the brain by using the stereotactic device. Then, an intravenous infusion of alpha-chloralose anesthesia (a bolus of ($\backsim$ 80 mg/kg) was performed through the catheter connected to the femoral vein, and inhalation of isoflurane was stopped at the same time. The body temperature of the animal was constantly monitored and maintained between 37-38 °C using a warm water heating pad. Throughout the experiment, alpha-chloralose anesthesia ($\backsim$ 25 mg/kg/h) and pancuronium ($\backsim$ 2 mg/kg/h) were provided through the catheter in the femoral vein using an infusion pump.

3.2.3 Data acquisition in electrophysiology experiments

Electrophysiology signals were acquired from LH and ACC using a single-channel tungsten electrode in each brain region. In addition to these recording electrodes, a silver wire was positioned in the space between skin and skull above the cerebellar areas for the purpose of ground and reference. Each electrode was connected to a custom-built preamplifier (25x gain and 0.1 Hz high pass) through a wire cable inside of a Faraday cage. This preamplifier was connected to an amplifier (MCP-Plus 8, Alpha Omega LTD; 20x gain and 10 kHz low pass), located outside of the cage. Signals from the amplifier were converted from analog to digital by using CED Power1401-3A (Cambridge Electronic Design). These digitally converted signals were recorded in the Spike 2 software (Cambridge Electronic Design). By combining the amplification factors from the preamplifier and amplifier, electrophysiology signals were acquired with a total amplification of 500 times at a sampling rate of 25 kHz. Additionally, the onset time for electrophysiology recording was controlled by MacroRecoder software in order to maintain the exact same onset time between electrophysiology and pupil size measurements.

3.2.4 Surgical procedures and data acquisition for multi-modal fMRI experiments

All details for stereotaxic injection of viral vectors and measurements of fMRI and Ca^{2+} signals are described in Chapter II (see Method 2.2.2, 2.2.3, 2.2.4, and 2.2.6) since the same surgical procedures were performed in this study.

3.2.5 Extraction of pupil diameter in pupillometry

All details of pupillometry for fMRI experiments are described in Chapter II (see Method 2.2.5) since the same methodological procedures were used. For the recording of pupil size in electrophysiology experiments, OBS studio was used to record the video with the following parameters: 30 frames/second, 8 bits per pixel in RGB24, and 628x586 pixels. By using the DeepLabCut toolbox [168, 169], four points were diagonally marked

on the edge of the pupil from 200 frames in each animal (Figure 2.1a). Then, an artificial network was trained based on these labeled frames using k-means clustering. This trained network computed the four points of all frames from all videos in each animal (Figure 2.1b, c). From the extracted four points, the pupil size was calculated with the above equation, mentioned in Chapter II (See Equation 2.1).

3.2.6 Electrophysiology analysis

All acquired data from Spike 2 software was first converted to the .mat file in order to perform data analysis in Matlab. Spectral analysis was first performed using the wavelet decomposition with a specification of 0.5-100 Hz frequency band and 2 s sliding window on the raw data of electrophysiology signals. From the outcome of spectral analysis, the LFP power was extracted between 0.5-100 Hz. This LFP power was filtered, using the filtfilt function of Matlab, into six different frequency bands of neuronal oscillations: delta wave (1-4 Hz), theta wave (4-7 Hz), alpha wave (7-14 Hz), beta wave (15-30 Hz), low gamma wave (30-60 Hz), and high gamma wave (60-100 Hz) according to the classification of neuronal oscillations in sleep from an animal study [20]. The power time series of each frequency band was smoothed with a 10 point moving average window, using the filtfilt function of Matlab.

Correlation analysis

Correlation analysis evaluates the degree of similarity between two variables of measurement. In our correlation analysis, pupil size and LFP power fluctuations were compared using the corrcoef function of Matlab.

Phase locking value

The phase locking value (PLV) analysis assesses phase synchronization of brain signals from two different recording electrodes (ACC and LH) in this study. The outcome indicates the functional connectivity between two brain regions [177]. Before performing the PLV analysis, the original electrophysiology data from the ACC and LH were first

downsampled from the sampling rate 25 kHz to 5 kHz. From the downsampled data, phase angles were calculated by applying the Morlet wavelet and fast Fourier transform. These phase angles were used to calculate the PLV using the following equation:

$$PLV = \left| \frac{\sum_{t=1}^{n} e^{i\left(\phi_{LH(t)} - \phi_{ACC(t)}\right)}}{n} \right| \tag{3.3}$$

In the Equation 3.3, $\phi_{LH(t)}$ and $\phi_{ACC(t)}$ depict phase angles in the time series from the LH and ACC, e^i depicts the complex exponential function, n depicts the number of sampling points.

Coherence

Coherence analysis evaluates the degree of synchronization between two different recording electrodes in the frequency domain [178]. To perform the coherence analysis, the original electrophysiology data from the ACC and LH with a sampling rate of 25 kHz were first downsampled to a sampling rate of 5 kHz. The magnitude-squared coherence was evaluated by applying these downsampled data in the Matlab mscohere function with a specification of 2 s Hanning window and 1s overlap. By using the mscohere function, functional connectivity has been previously investigated in electrophysiology analysis [179].

Phase-amplitude coupling

Phase-amplitude coupling analysis assesses a degree of synchronization between the phase of low frequency band and amplitude of high frequency band from electrophysiology signals and suggests brain state modulation [180, 181]. First, phase angles of delta band was calculated using the angle and hilbert functions of Matlab. The amplitude of higher frequency bands (theta, alpha, beta, low gamma, and high gamma bands) was calculated using the envelope function of Matlab. To perform the phase-amplitude coupling analysis, the modulation index (MI) [181] was evaluated from the calculated phase angles and amplitudes using the modulation_index function

(`https://github.com/pierremegevand/modulation_index`) in Matlab.

3.2.7 Calcium signal analysis

To extract Ca^{2+} power, spectral analysis was performed using the wavelet decomposition with a specification of 0.5-100 Hz frequency band and 2 s sliding window from the raw data of Ca^{2+} signals. From the outcome of spectral analysis, the Ca^{2+} power was extracted between 0.5-10 Hz frequency. The extracted Ca^{2+} power was filtered to 1-4 Hz (the same frequency range as the LFP delta band) by using the Matlab filtfilt function. The extracted 1-4 Hz Ca^{2+} power was used for correlation analysis with pupil size and fMRI signals using the corr and corrcoef functions of Matlab.

3.2.8 fMRI analysis

All details for preprocessing of fMRI data are described in Chapter II (see Method 2.2.8) since the same analytical procedures were performed in this study. The preprocessed fMRI data were first filtered between 0.01 and 0.1 Hz using the filtfilt function of Matlab. The filtered fMRI data were used for correlation analysis with pupil size and 1-4 Hz Ca^{2+} power fluctuations, using the corr function of Matlab. By using the calculated correlation coefficient, t-values for voxel-wise correlation were computed in Matlab to compare the fMRI correlation maps with previous studies [10, 165]:

$$t = \frac{r\sqrt{n-2}}{\sqrt{1-r^2}} \tag{3.4}$$

In the Equation 3.4, t depicts t-value, n depicts the number of sampling points, r depicts correlation coefficients. The t-value fMRI map from each trial was overlaid on the anatomical scan using AFNI [170]. To identify brain regions of the t-value fMRI map, anatomical images with t-values were additionally overlaid on the rat brain atlas [167]

3.2.9 Thresholding to distinguish positive and negative correlations in each correlation analysis

Electrophysiology and pupil size correlation

To determine the thresholds of positive, no, and negative correlations between LFP band power and pupil size fluctuations, correlations between the randomized time course of pupil size and delta power with 10,000 permutations were first calculated with the corrcoef and randperm functions of Matlab. Then, 95 % confidence intervals from the null distribution of these 10,000 correlations were computed (Figure S2). If correlation coefficients of experimental trials exceeded above the upper limit of 95 % confidence interval (above 0.065 correlation coefficients), the trials were considered as a positive correlation. If correlation coefficients of experimental trials fell below the lower limit of 95 % confidence interval (below -0.065 correlation coefficients), the trials were considered as a negative correlation. The remaining trials ($-0.05 <$ correlation coefficients < 0.065) were considered as no correlation. The null distribution of 10,000 correlations between the randomized time course of pupil size and delta power exhibited a normal distribution and differed from the distribution of experimentally acquired correlations between pupil size and delta power (Figure S2). These results indicated that the correlation between LFP delta power and pupil size fluctuations was not generated by random chance.

Ca^{2+} and pupil size correlation

In the same manner as the determination of thresholds for positive, no, and negative correlations between LFP band power and pupil size fluctuations, correlations between the randomized time course of pupil size and 1-4 Hz Ca^{2+} power with 10,000 permutations were also calculated with the corrcoef and randperm functions of Matlab. Then, 95 % confidence intervals from the null distribution of these 10,000 correlations were computed (Figure S6). If correlation coefficients of experimental trials exceeded above the upper limit of 95 % confidence interval (above 0.065 correlation coefficients), the trials were considered as a positive correlation. If correlation coefficients of experimen-

tal trials fell below the lower limit of 95 % confidence interval (below -0.065 correlation coefficients), the trials were considered as a negative correlation. The remaining trials ($-0.065 <$ correlation coefficients < 0.065) were considered as no correlation. The null distribution of 10,000 correlations between the randomized time course of pupil size and 1-4 Hz Ca^{2+} power exhibited normal distribution and differed from the distribution of experimentally acquired correlations between pupil size and 1-4 Hz Ca^{2+} power (Figure S6). These results indicated that the correlation between 1-4 Hz Ca^{2+} power and pupil size fluctuations was not generated by a random chance.

Pupil size and fMRI correlation

To determine the thresholds of positive, no, and negative correlations between pupil size and fMRI signal fluctuations, correlation between the randomized time course of pupil size and fMRI in the LH was also calculated with the corr and randperm functions of Matlab. Then, t-value for the correlation was computed based on the Equation 3.4, and 10,000 permutations were performed. The ROI for the LH was selected from a coronal slice of anatomical scans (A/P = -3.2mm, 33 voxels), the same location where LFP recording for the LH was conducted. From the obtained 10,000 t-values for correlation, 95 % confidence intervals of the null distribution were computed (Figure S10). If the t-value from experimental trials exceeded above the upper limit of 95 % confidence interval (t-value$>$ 1.96), the t-value was considered as a positive correlation. If the t-value from experimental trials fell below the lower limit of 95 % confidence interval (t-value$<$ -1.96), the t-value was considered as a negative correlation. The remaining t-values ($-1.96 <$ t-value < 1.96) were considered as no correlation. The null distribution of 10,000 t-values between the randomized time course of pupil size and fMRI exhibited normal distribution and differed from the distribution of experimentally acquired t-values between pupil size and fMRI (Figure S10). Furthermore, the false discovery rate (FDR) correction was applied for the statistical correction of a t-value correlation map between fMRI voxel (20,022 voxels) and pupil size, using the FDR function in Matlab with alpha 0.05 (`https://www.mathworks.com/`

matlabcentral/fileexchange/71734-fdr-false-discovery-rat). After the FDR correction, the threshold of positive correlation was t-value > 2.54 and negative correlation was t-value < -2.54 in the whole-brain t-value correlation map (Figure 3.4c,Figure S9).

Ca^{2+} and fMRI correlation

T-value correlation map for fMRI and 1-4 Hz Ca^{2+} power was computed in the same manner as the t-value correlation map of pupil size and fMRI signal as described in the above section 3.2.9 "Pupil size and fMRI correlation".

3.3 Results

3.3.1 Relationship between pupil size and LFP signals at the LH and ACC

Electrophysiology signals were recorded from tungsten electrodes placed on the LH and ACC of anesthetized animals with simultaneous pupil size measurements for 15 min (Figure 3.1a). The power spectrogram of the electrophysiology signals showed the strongest power in the range of LFP 1-4 Hz (Figure 3.1b). In parallel, the pupil size also fluctuated similarly with the change of LFP 1-4 Hz power (Figure 3.1b). Interestingly, this coupling of pupil size and LFP power appeared with positive, no, and negative correlations across different trials in both ACC and LH ($n = 89$, 9 animals; Figure 3.1c, d). These unique variations of correlation patterns were also confirmed across different trials of each animal (Figure S1). Since the 1-4 Hz power was the strongest frequency band that we could observe under anesthesia, we performed in-depth examinations of delta (1-4 Hz) power and pupil size fluctuation. The positive and negative correlations of LFP delta power in the LH and pupil size fluctuations were more uniformly distributed ([positive corr]: 52 % ($n = 46$), [no corr]: 4 % ($n = 4$), [negative corr]: 44 % ($n = 39$); Figure 3.1e, left). However, the correlation pattern was more negatively distributed in the ACC LFP recording ([positive corr]: 13 % ($n = 12$), [no corr]: 8 % ($n = 7$), [- corr]: 79 % ($n = 70$); Figure 3.1e, right). The thresholds to determine the positive and negative correlations were calculated by 95 % confidence intervals of null distribution from 10,000 permuted correlations between the randomized time course of pupil size and delta power (See Method 3.2.9 and Figure S2). The two-sample Kolmogorov-Smirnov test [182] showed that distributions of the correlation between the ACC and LH were significantly different ($p = 5.1 \times 10^{-7}$; Figure 3.1f). When pupil size and LH delta power fluctuations showed negative correlations (LFP-Group 1), pupil size and ACC delta power correlations were always negative (Figure 3.1g). However, when pupil size and LH delta power fluctuations showed positive correlations (LFP-Group 2), pupil size and ACC delta power were both positively and negatively correlated (Figure 3.1g). These

correlations between pupil size and ACC delta power of LFP-Group 1 and 2 differed significantly in the evaluation of two-sample t-tests ($p = 5.2 \times 10^{-10}$; Figure 3.1g). These results suggest that the correlation feature between pupil size and LH activity may indicate differences in the brain state.

3.3.2 Identifying different brain states from time–frequency analysis

To characterize different brain states based on the correlations of pupil size and LH delta power fluctuations (LFP-Group 1 and 2), time-frequency analysis was performed. First, the power spectral analysis exhibited the peak of LFP mean power on both the LH and ACC at 2 Hz in LFP-Group 1 but 3 Hz in LFP-Group 2 (Figure 3.2a, Figure S3). Similarly, the PLV analysis also presented differences on phase synchronization of LH and ACC LFP signals: the PLV was higher at 2 Hz in LFP-Group 1 but at 3 Hz in LFP-Group 2 (Figure 3.2b, c and Table S1). The PLV between LFP-Group 1 and 2 differed significantly at 2 Hz ($p = 4.8 \times 10^{-7}$) and 3 Hz ($p = 8.8 \times 10^{-7}$) in the evaluation of two-sample t-tests. In consistency with the PLV analysis, the coherence between LFP signals of ACC and LH also exhibited the highest synchronization in the frequency domain at 2 Hz in LFP-Group 1 but 3 Hz in LFP-Group 2 (Figure 3.2d and Figure S4). Furthermore, the phase-amplitude coupling analysis indicated that MI between the phase of low frequency band (delta) and amplitude of higher frequency bands (theta, alpha, beta, low gamma, and high gamma) in the ACC showed higher values in LFP-Group 1 compared to LFP-Group 2 (Figure 3.2e and Table S2). The two-sample t-tests also confirmed that the MI between LFP-Group 1 and 2 for the ACC differs significantly ($p = 1.9 \times 10^{-12}$ for delta-theta, $p = 4.6 \times 10^{-12}$ for delta-alpha, $p = 1.9 \times 10^{-11}$ for delta-beta, $p = 1.5 \times 10^{-5}$ for delta-low gamma, $p = 5.9 \times 10^{-8}$ for delta-high gamma). Similarly, comparable results were also observed in the LH that the MI in LFP-Group 1 showed significantly higher values compared to LFP-Group 2 except delta-low gamma interactions ($p = 2.6 \times 10^{-8}$ for delta-theta, $p = 2.4 \times 10^{-7}$ for delta-alpha, $p = 3.2 \times 10^{-8}$ for delta-beta, $p = 0.0013$ for delta-high gamma; Figure S5 and Table S3). These examinations suggest different neural coupling mechanisms

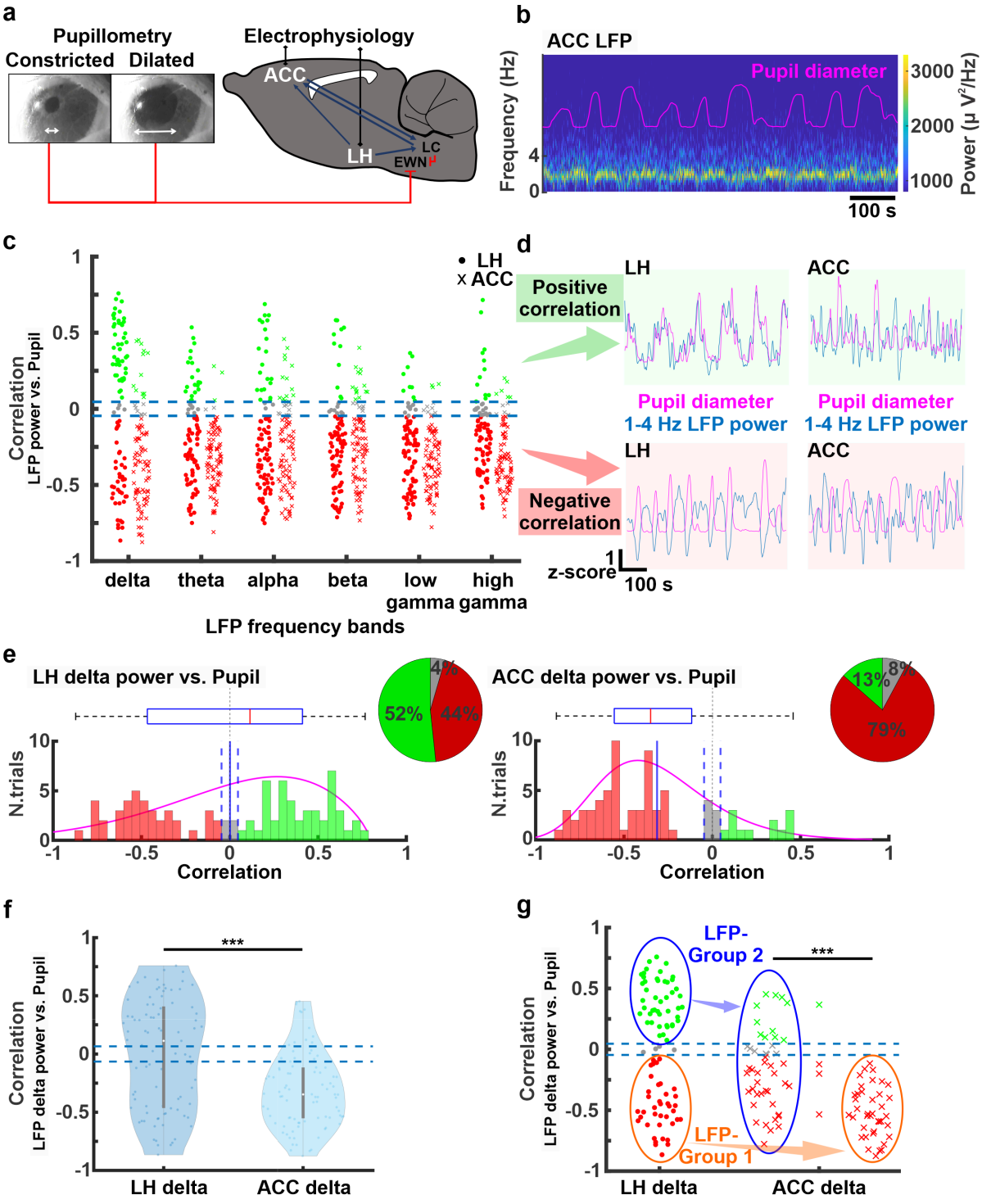

Figure 3.1 Correlation analysis between pupil size and LFP power band fluctuations. a) A diagram showing the locations of the ACC and LH where the electrodes were placed for electrophysiological signal recording as well as image examples of pupil dilation and constriction. b) A representative example of power spectrogram from a 15 min LFP recording at the ACC. The pink trace depicts changes in pupil diameter. c) Correlations between pupil size and each LFP power band fluctuations at the LH (circle markers) and ACC (cross markers) (89 trials, 9 animals). (the caption continues to the next page)

Figure 3.1 The positive correlation is depicted by green markers, no correlation by gray markers, and negative correlation by red markers. d) Representative examples of pupil size (pink trace) and LFP delta power (blue trace) fluctuations at the LH (left Figures) and ACC (right Figures), showing positive (upper Figures) and negative (lower Figures) correlations. e) Correlations between pupil size and delta power at the LH (left) and ACC (right) across all trials (89 trials from 9 animals). The positive correlation is depicted by green markers, no correlation by gray markers, and negative correlation by red markers. The boxplots and pink traces depict the distribution of correlations. The pie charts depict the percentage of positive, no, and negative correlations across trials. f) The distribution of correlations between pupil size and delta power at the ACC and LH in violin plots. g) Grouping the correlations based on trials when LH delta power and pupil size fluctuations were positively (named LFP-Group 1, orange circle) or negatively (named LFP-Group 2, blue circle) correlated. The blue dashed lines depict the thresholds of positive (correlation coefficents = 0.046) and negative (correlation coefficents = -0.046) correlations. Note: *** $p < 0.001$, ** $p < 0.01$, * $p < 0.05$ (Adapted from Takahashi et al., 2021) [175].

between ACC and LH under the two different states of anesthesia, similar to previous studies of different brain states in sleep [183–185].

3.3.3 Examination of Ca^{2+} signal coupling with pupil size and whole brain fMRI signal

Here, simultaneous recording of pupil size, BOLD fMRI, and Ca^{2+} signal was conducted to investigate the coupling features between whole-brain activity and pupil size, which vary depending on the brain state (Figure 3.3a). The Ca^{2+} signal, recorded from GCaMP expressing neurons through fiber photometry, showed the strongest power in the range of 1-4 Hz in the power spectrogram (Figure 3.3b), similar to the power spectrogram of LFP (Figure 3.1b). In parallel, the pupil size also fluctuated with the change of Ca^{2+} 1-4 Hz power (Figure 3.3b). The coupling of pupil size and Ca^{2+} power appeared with positive, no, and negative correlations across different trials in the ACC but showed a more negative distribution ([positive corr]: 11 % ($n = 7$), [no corr]: 20 % ($n = 12$), [negative corr]: 69 % ($n = 42$), 9 animals; Figure 3.3c, d), similar to the correlation

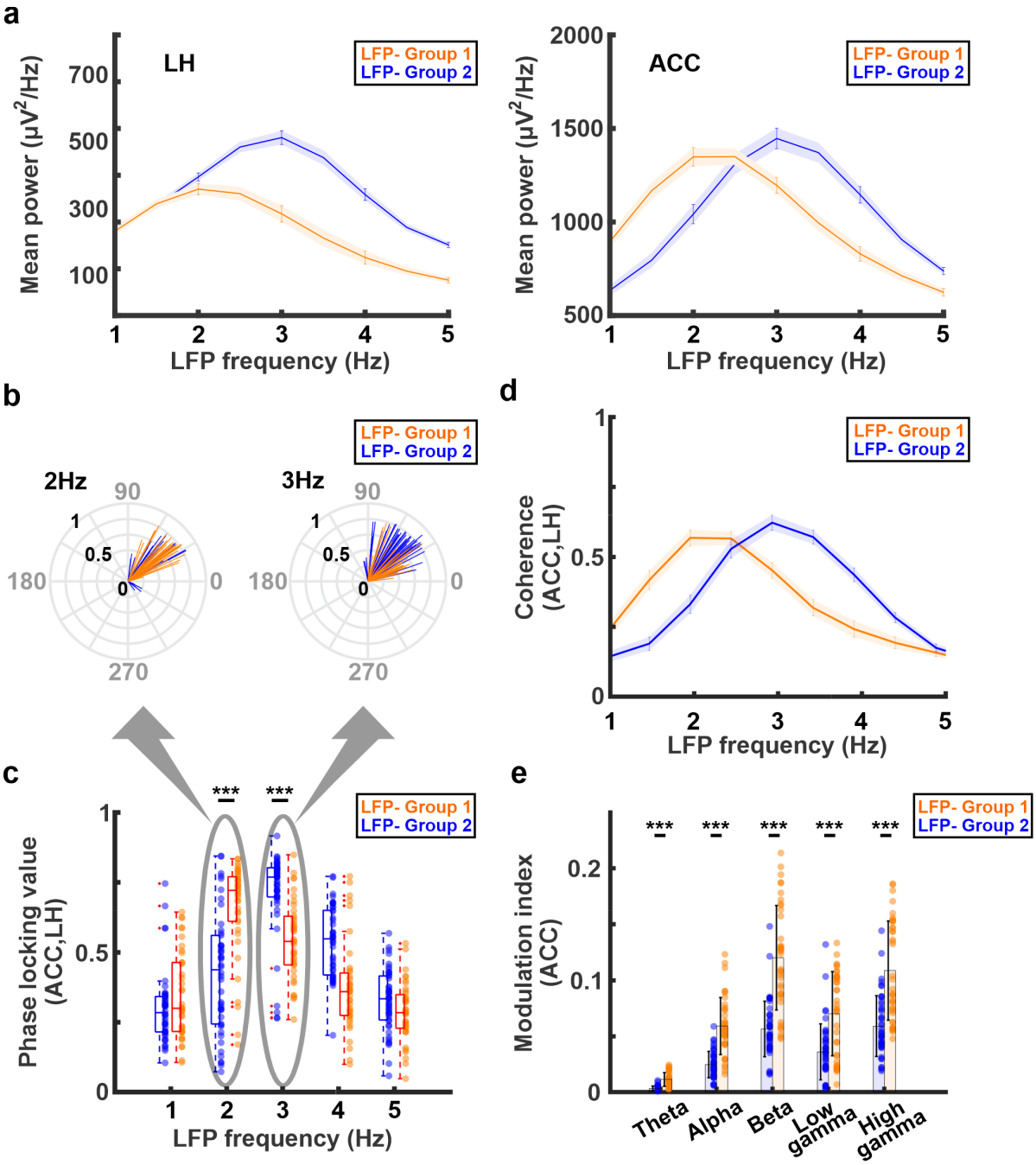

Figure 3.2 Power spectrum and cross frequency analyses. a) The distribution of LFP power from the ACC(right) and LH(left). The orange lines indicate trials when LH delta power and pupil size showed negative correlations (LFP-Group 1). The blue lines indicate trials when LH delta power and pupil size showed positive correlations (LFP-Group 2). The standard error of the mean is indicated by the shaded regions. b) Polar plots of phase-locking values from 2 and 3 Hz electrophysiology signals between the ACC and LH in the LFP-Group 1 (orange) and 2 (blue). c) Phase-locking values from 1-5 Hz electrophysiology signals between ACC and LH in LFP-Group 1 (orange) and 2 (blue). (the caption continues to the next page)

Figure 3.2 d) Coherence of electrophysiology signals between the ACC and LH in LFP-Group 1 (orange) and 2 (blue). The standard error of mean is indicated by shaded regions. e) MI between phase angles of delta band and amplitudes of theta, alpha, beta, low gamma, and high gamma bands from ACC in LFP-Group 1 (orange) and 2 (blue). The standard deviation is depicted by error bars. Note: *** $p < 0.001$, ** $p < 0.01$, * $p < 0.05$. (Adapted from Takahashi et al., 2021) [175].

analysis of LFP delta power and pupil size (Figure 3.1e). The thresholds to determine these positive and negative correlations were calculated by 95 % confidence intervals of null distribution from 10,000 permuted correlations between the randomized time course of pupil size and Ca^{2+} 1-4 Hz power (See Method 3.2.9 and Figure S6). The Ca^{2+} 1-4 Hz power from the ACC also exhibited both positive and negative correlations with fMRI signals over different trials and brain regions (Figure S7). These positive and negative correlations appeared more robustly under the trials when the Ca^{2+} 1-4 Hz power fluctuation was negatively correlated with pupil size (Figure 3.3f), compared to the rest of trials (Figure S8). Particularly, positive correlations were more apparent in the cortical and thalamic regions, but negative correlations were more apparent in the brainstem and subcortcial regions, including the LH (Figure 3.3f, Figure S7). These results suggest that ACC Ca^{2+} and fMRI coupling features can vary depending on different brain states of anesthesia.

3.3.4 Characterizing different brain states from the coupling of pupil size and LH BOLD fMRI

To investigate different brain states based on the correlations between LH activity and pupil size in shaping the whole brain view and compare the results with LFP data analysis (See Result 3.3.1 and 3.3.2), correlations between BOLD fMRI signal and pupil size were evaluated. The whole brain fMRI correlation map with pupil size appeared to have more negative correlations in the cortical and thalamic regions (Figure S9). The correlation between dynamics of pupil size and fMRI signals appeared positively and negatively depending on trials and brain regions (Figure 3.4a, b). In the LH, 33 %($n =$

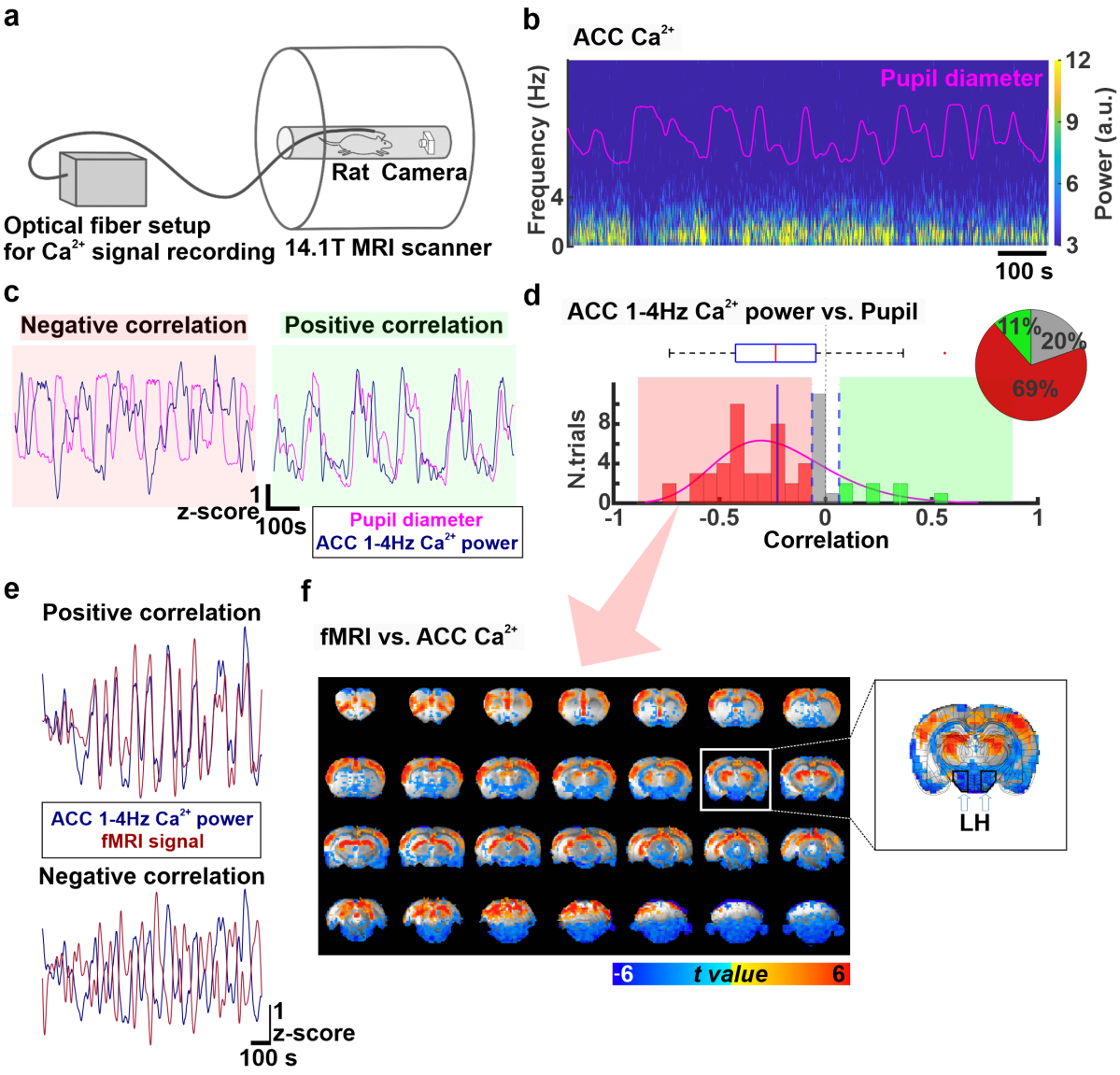

Figure 3.3 Correlation analysis from multi-modal fMRI recordings. a) Simultaneous recordings of pupil size, fMRI, and Ca^{2+} signals. b) A representative example of a power spectrogram from a 15 min Ca^{2+} signal recording at the ACC. The pink trace depicts the changes in pupil diameter. c) Representative examples of pupil size (pink trace) and Ca^{2+} 1-4 Hz power (blue trace) fluctuations at the ACC, showing positive (right Figure) and negative (left Figure) correlations. d) Correlations between Ca^{2+} 1-4 Hz power at the ACC and pupil size across all trials (61 trials from 9 animals). The boxplots and pink traces depict the distribution of correlations. The pie charts depict the percentage of positive (green), no (gray), and negative (red) correlations across trials ([positive corr]: 11 % ($n = 7$), [no corr]: 20 % ($n = 12$), [negative corr]: 69 % ($n = 42$)). e) Representative examples of Ca^{2+} 1-4 Hz power at the ACC (blue trace) and fMRI signal (brown trace) fluctuations, showing positive (upper Figure) and negative (lower Figure) correlations. (the caption continues to the next page)

Figure 3.3 f) A t-value correlation map between fMRI voxels and Ca^{2+} 1-4 Hz power at the ACC from the trials when Ca^{2+} 1-4 Hz power fluctuation was negatively correlated with pupil size (69 %, $n = 42$). On the overlaid correlation map, only the t-values above 2.25 and below -2.25 are displayed to demonstrate positive and negative correlations. The magnified photo displays the position of LH (A/P= -3.2mm), indicated by black polygons and white arrows. (Adapted from Takahashi et al., 2021) [175].

20) of trials showed positive correlations between dynamics of LH fMRI signals and pupil size and 67 %($n = 41$) no correlation, shown by t-values of correlations(Figure 3.4b). The thresholds to determine these positive and negative correlations were calculated by 95 % confidence intervals of null distribution from 10,000 permuted correlations between the randomized time course of pupil size and LH fMRI signals (See Method 3.2.9 and Figure S10). These positive correlation trials were named as fMRI-Group 1 and negative as fMRI-Group 2. In the fMRI-Group 1 trials, pupil dynamics were positively correlated with fMRI signals in the subcortical and brainstem areas but negatively in cortical and thalamic areas (Figure 3.4c). However, a significant correlation was not observed at the whole brain level under the fMRI-Group 2 trials (Figure 3.4c). Furthermore, correlations between dynamics of pupil size and Ca^{2+} 1-4 Hz power at the ACC always appeared with the negative sign in the fMRI-Group 1 trials but with random correlation patterns in the fMRI-Group 2 trials (Figure 3.4d, e), demonstrating the compatible results with the LFP analysis (See Result 3.1g). These t-values of correlations for dynamics of pupil size and ACC Ca^{2+} power between fMRI-Group 1 and 2 differed significantly in the evaluation of two-sample t-tests ($p = 3.7 \times 10^{-4}$; Figure 3.4d). Although the positive correlation between pupil size and LH fMRI activity predicted the negative correlation of pupil size and ACC Ca^{2+} power, the negative correlation between pupil size and LH LFP delta activity predicted the negative correlation of pupil size and ACC LFP delta power. This relationship may possibly be resulted from an opposite correlation feature between LFP delta power and fMRI signals in the LH (See Discussion 3.4). Moreover, correlations between dynamics of ACC Ca^{2+} power and whole-brain fMRI signal appeared more significantly in the fMRI-Group 1 trials than the fMRI-Group 2

(Figure 3.4f). These results suggest that the correlation feature between fluctuations of pupil size and LH fMRI signal can characterize different brain states, in consistence with brain state differences from the LH LFP and pupil size relationship.

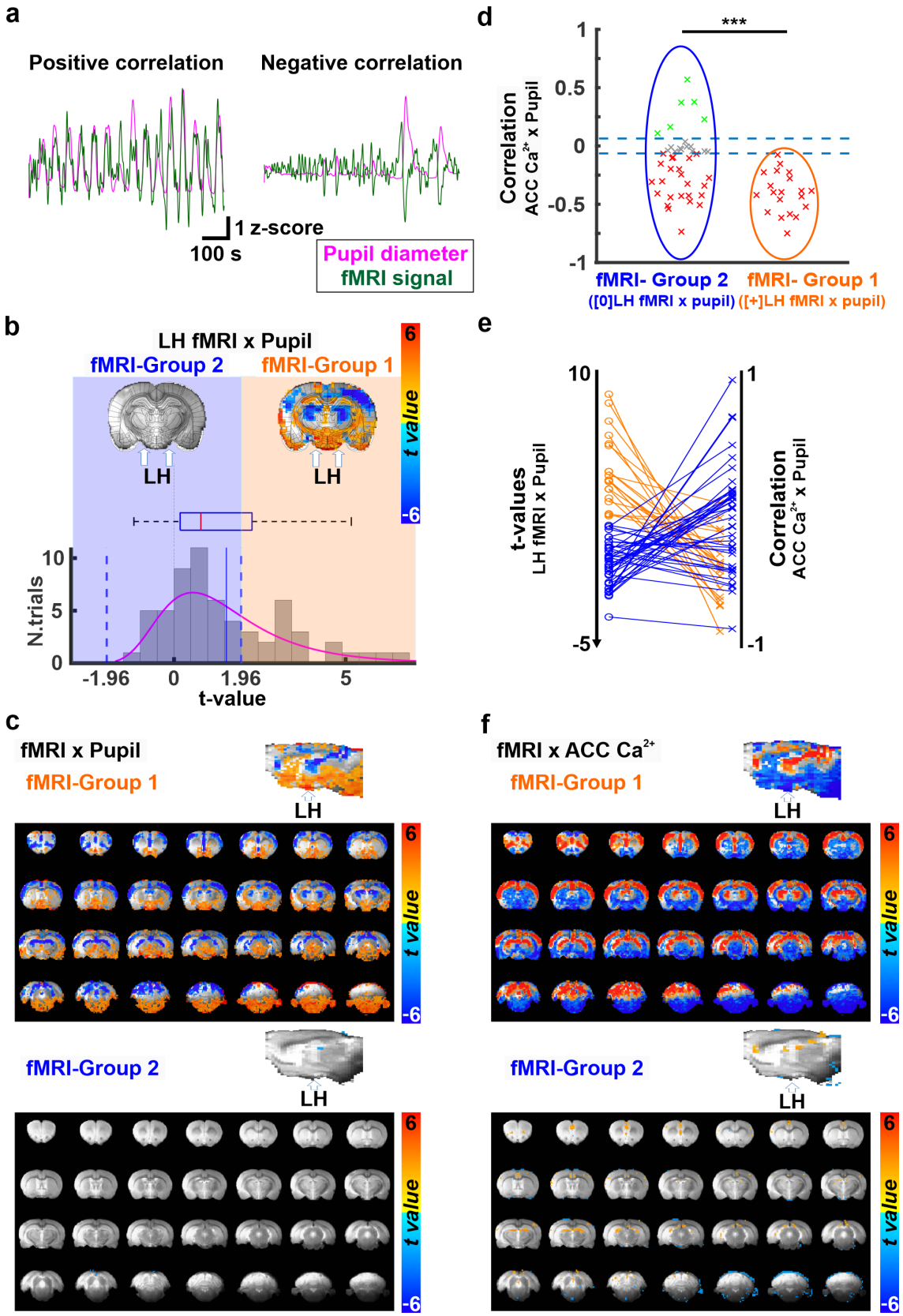

Figure 3.4 a) Representative examples of pupil size (pink trace) and fMRI signal (green trace) fluctuations, showing positive (left Figure) and negative (right Figure) correlations. (the caption continues to the next page)

Figure 3.4 b) Bar plots for correlations between pupil size and LH fMRI BOLD signal across all trials (61 trials from 9 animals). The boxplots and pink curve depict the distribution of correlations. The orange shaded color box shows trials with the positive correlation (33 %, $n = 20$), named fMRI-Group 1. The blue shaded color box shows trials with no correlation (67 %, $n = 41$), named fMRI-Group 2. c) A t-value correlation map between fMRI voxels and pupil size from the trials when the LH fMRI signal was positively (fMRI-Group 1, top Figure) and not (fMRI-Group 2, bottom Figure) correlated with pupil size. On the overlaid correlation map, only the t-values above 2.54 and below -2.54 are displayed to demonstrate positive and negative correlations. The sagittal photo displays the position of LH, indicated by a white arrow. d) Correlations between Ca^{2+} 1-4 Hz power at the ACC and pupil size from the trials when the LH fMRI signal was positively (fMRI-Group 1, orange circle, $n = 20$) and not (fMRI-Group 2, blue circle, $n = 41$) correlated with pupil size. e) Plots demonstrating the association between two correlation analyses. The scatter plot on the left shows t-values of correlations between pupil size and LH fMRI BOLD signal from the trials (33 %, $n = 20$). The scatter plot on the right shows correlations between Ca^{2+} 1-4 Hz power at the ACC and pupil size (67 %, $n = 41$). The orange color indicates the trials when the LH fMRI signal was positively correlated (fMRI-Group 1) and the blue color indicates the trials when the LH fMRI signal was not correlated (fMRI-Group 2). f) A t-value correlation map between fMRI voxels and Ca^{2+} 1-4 Hz power at the ACC from the trials when the LH fMRI signal was positively (fMRI-Group 1, top Figure) and not (fMRI-Group 2, bottom Figure) correlated with pupil size. On the overlaid correlation map, only the t-values above 2.54 and below -2.54 are displayed to demonstrate positive and negative correlations. The sagittal photo displays the position of LH, indicated by a white arrow. Note: *** $p < 0.001$, ** $p < 0.01$, * $p < 0.05$ (Adapted from Takahashi et al., 2021) [175].

3.4 Discussion

This Chapter III demonstrated brain state-dependent coupling features between dynamics of pupil size and whole-brain activity by investigating the LH and ACC of anesthetized animals in multi-modal brain signal measures. In the electrophysiology study, fluctuation of ACC LFP delta power was always negatively correlated with pupil dynamics in trials when LH LFP delta power and pupil dynamics exhibited negative correlations. On the other hand, correlations of ACC LFP delta power with pupil size varied unpredictably in positive correlation trials between LH LFP delta power and pupil dynamics. Based on these distinctive correlation features, we characterized two distinct brain states (Named as LFP-Group 1 and 2) by performing cross-frequency coupling analyses. Furthermore, these unique LH/ACC-pupil correlation patterns were compatibly identified in the fMRI study, demonstrated by the appearance of the negative correlation between dynamics of ACC 1-Ca^{2+} power with pupil size in all trials when LH fMRI signal and pupil dynamics exhibited positive correlations. Overall, we identified two different brain states from interactions of pupil and LH activity, confirmed by the cross-frequency coupling analyses from LFP signals and correlations among pupil size, LFP, Ca^{2+}, and whole-brain fMRI signals.

Dynamics of pupil size are known to indicate changes in arousal levels, reflected in brain signals from electrophysiology and fMRI signals [9, 12, 20, 23, 45]. However, correlation features among dynamics of pupil size, electrophysiology, and fMRI signals often vary across trials due to underlying brain state differences [20, 23, 46, 47, 153]. Our results also exhibited varied correlation patterns between fluctuations of pupil size and LFP power in the ACC and LH of anesthetized animals across different recording trials (Figure 3.1c, d). Anesthetized brain states express similar features of brain signals from distinct sleep stages, possibly sharing common apparatus of brain state regulation [21, 22]. These brain states during anesthesia, sleep, and wakefulness are commonly regulated by subcortical and brainstem regions such as the LH [15, 49, 65, 66]. For instance, neuronal activity of arousal-regulating cells in the LH decreases under anesthesia and slow-wave sleep [65, 73]. Furthermore, optogenetic stimulation of these

arousal-regulating LH neurons leads to a brain state transition from anesthesia or sleep to wakefulness [15, 74]. On the other hand, the neuronal activity of MCH cells, sleep-promoting neurons, does not change under anesthesia [65]. Thus, LH activity alters depending on the underlying brain state. The LH is also involved in modulating pupil size through neuronal projections to pupil-regulating circuits [59, 86]. These factors suggest that the varied LH activities under different brain states of anesthesia might have produced different correlation patterns between dynamics of pupil size and LFP power in our result (Figure 3.1c, d).

In addition to the interaction of LH activity with pupil dynamics, we observed that ACC activity is also linked with pupil dynamics as well as LH activity (Figure 3.1e and 3.2c,d). The ACC appears in the default mode network in both animals and humans [91], and the activity of ACC varies depending on the underlying brain state since the default mode network under a low arousal state exhibits a reduced involvement of ACC activity in comparison to a high arousal state [24, 92]. The ACC mediates brain states through bidirectional projections to the LC and also contributes to modulating pupil size since noradrenergic neurons in the LC are key neurotransmitters for both brain state and pupil size regulation [10, 41, 90, 186]. However, correlations between dynamics of pupil size and ACC activity in our study showed both positive and negative correlations across different recording trials (Figure 3.1c, d, e). This observation of variation in correlations suggests that interaction between pupil size and ACC activity is not simply caused by noradrenergic innervation of LC. Since both ACC and LC receive projections from the LH that also mediates both pupil size and brain states [13, 83, 84], we propose that the varied interaction features between pupil size and ACC activity are mediated by the LH.

Our observation for correlations between fluctuations of pupil size and ACC delta power always showed negative correlations among trials when LH delta power was negatively correlated with pupil size, named as LFP-Group 1 (Figure 3.1g). However, these interactions of ACC and pupil appeared more randomly, showing positive and negative correlations, among trials when LH delta power was positively correlated with pupil size, named as LFP-Group 2 (Figure 3.1g). Correlation features between dynamics of

pupil size and brain signals in electrophysiology or fMRI vary depending on underlying brain states [20, 23]. Particularly, stronger negative correlations between the power of low frequency electrophysiology signal and pupil size fluctuations indicate a lower arousal state during unconsciousness [20]. Thus, our results indicate that LFP-Group 1 represents a low arousal state under anesthesia. In fact, the power spectral density of electrophysiology signals from the ACC and LH showed the peak power at 2 Hz in LFP-Group 1 but 3 Hz in LFP-Group 2 (Figure 3.2a), showing similar tendencies as in sleep studies where the peak frequency appears around 2 Hz during a lower arousal state of unconsciousness but 2.5-3 Hz during a higher arousal state of unconsciousness in cortical areas [184, 185, 187, 188]. Furthermore, phase-amplitude coupling values (See Method 3.2.6) in LFP-Group 1 were higher than LFP-Group 2, also demonstrating that LFP-Group 1 is a lower arousal state since a deeper state of unconsciousness (anesthesia and sleep) expresses higher phase-amplitude coupling values [180, 183, 189]. Between LFP-Group 1 and 2, functional connectivity of ACC and LH also switched as both PLV and magnitude-squared coherence appeared with different synchronization frequencies (2 Hz in LFP-Group 1 but 3 Hz in LFP-Group 2), in consistence with previous studies showing changes of PLV and coherence upon brain state alteration during sleep or anesthesia) [190–192]. Therefore, we demonstrated brain state differences under anesthesia (LFP-Group 1 vs. 2) by performing cross-frequency analysis from electrophysiology signals at the LH and ACC.

To track brain state fluctuations, changes of pupil size are commonly monitored together with fMRI [12, 23, 165]. In Chapter II 2.3.2, we demonstrated the global BOLD fMRI signal correlates negatively with changes of pupil size (See Figure 2.4a, b). This observation is in consistence with previous reports demonstrating the negative correlation between dynamics of pupil size and cortical low frequency LFP power during anesthesia and sleep [16, 20]. However, the correlation patterns in both electrophysiology and fMRI measurements vary under different brain states [10, 20, 23]. Our results also exhibited various correlations between dynamics of pupil size and electrophysiology/fMRI signals across trials (Figure 3.1c,d,e, and 3.4a,b). Similar to the observation of vari-

ous correlations between LH LFP and pupil dynamics, the LH BOLD fMRI signal also showed varied correlation features with pupil dynamics among different trials: 33 % of positive correlation and 67 % of no correlation (Figure 3.4b). Interestingly, under the condition of these positive correlation trials (fMRI-Group 1), dynamics of Ca^{2+} 1-4 Hz power were always negatively correlated with pupil size fluctuation (Figure 3.4d). This observation was consistent with the findings from the correlation analysis of LH LFP with pupil dynamics (Figure 3.1g). These results demonstrated that compatible brain states were distinguished between electrophysiology and fMRI signals based on pupil size and LH activity. Furthermore, fMRI-Group 1 feasibly indicated a lower arousal state compared to fMRI-Group 2. Under the condition of fMRI-Group 1, robust negative correlations between dynamics of pupil size and fMRI signal in cortical and thalamic areas were mainly observed and positive correlations in subcortical and brainstem areas (Figure 3.4c). However, these correlations did not appear in fMRI-Group 2 (Figure 3.4c), suggesting a transition of brain states from the interaction of pupil size and LH fMRI signal.

In spite of the fact that correlation analysis between fluctuations of pupil size and electrophysiology/fMRI signals is a well-established method to track brain states, the correlation feature also varies depending on underlying brain states, different frequency ranges of LFP signals, or brain regions [127, 150–152]. For instance, correlation strength between fMRI and neuronal signals in the cortex appears stronger during a deep unconscious state compared to high arousal state [153]. Our result also exhibited the positive correlation between fluctuations of fMRI signal and Ca^{2+} 1-4 Hz power (Figure 3.3f, 3.4f and Figure S7). However, the negative correlation emerged in subcortical and brainstem regions such as the striatum and LH (Figure 3.3f, 3.4f and Figure S7). This observation is similar to previous reports demonstrating that activity in subcortical regions (e.g., striatum) expresses the negative correlation between LFP power from a low frequency band (e.g., delta) and fMRI signal [154, 155]. These results indicate that vascular and neuronal interactions diversify across brain regions and states.

Overall, this Chapter III demonstrates diverse correlation patterns that vary un-

der distinct brain states, among different brain regions (e.g., ACC and LH), and across cross-scale recordings (e.g., correlations among pupil size, LFP, Ca^{2+} signal, and fMRI as well as cross-frequency couplings). In particular, interactions between pupil size and ACC/LH activity from electrophysiology and fMRI signals provide a unique perspective to evaluate brain arousal states. Thus, this approach may contribute to a deeper understanding of neuronal dynamics in brain arousal state research.

4 Chapter IV: Manipulation of pupil size and brain state by lateral hypothalamic stimulation

4.1 Introduction

All work in this Chapter IV may be published in a peer-reviewed journal in the future since we are currently in preparation for publication at the time of this thesis submission.

The study from Chapter III demonstrated unique correlation features (positive vs. negative) between dynamics of pupil size and LH/ACC activities that varied depending on the underlying brain state. In fact, previous studies also reported trial-dependent variability of correlations between pupil size and neuronal activities of pupil-regulating regions such as the LC and ACC perhaps because of the impact of brain state differences [10, 46, 47]. Since the LH carries neuronal projections to the pupil-regulatory circuits and also modulates brain states [13, 83, 84], LH may play a key role in understanding the variations of correlations.

The pupil regulating networks, embracing multiple brain regions such as the LC, also receive inputs from the LH [13, 83], and interactions within the circuit such as LH-LC functional interactivity mediate brain states as well[85, 193]. The LH is known to regulate brain arousal states since optogenetics in various arousal-modulating neurons of the LH promotes a transition of brain states [15, 74, 79]. The modulation of brain

states by optogenetics of the LH is induced depending on stimulation frequencies: higher stimulation frequencies (≥ 5 Hz) can cause a brain state transition with more probability [15, 74, 81, 82]. In fact, each neuronal population in the LH shows selective behaviors of neural discharges depending on given stimulation frequencies, which can lead to the release of distinct neurotransmitters that mediate brain states [194]. Moreover, brain state transitions induced by optogenetics are also affected by a fundamental brain state by the time of stimulation, showing distinct success rates of brain state modulations under different initial brain states [15]. Hence, investigation of the LH on concurrent pupil size and brain state modulations may contribute to elucidating varied correlation features of neuronal activity in arousal-regulatory areas with pupil size.

In this Chapter IV, optogenetic stimulation with frequencies between 1-20 Hz was conducted in LH neurons to evaluate the attributes of concurrent changes in brain states and pupil size. Activation of the LH enlarged pupil diameter and diminished LFP delta power of the ACC and LH. In addition, a higher increment in pupil size and a decrement in LFP delta power of the ACC and LH with exponential hallmarks appeared as stimulation frequencies increased, indicating that LH-induced alteration of pupil size and brain states contains unique frequency-dependent features. The exponential feature for delta power decrement emerged only under one state when the delta power of ACC from the pre-stimulation phase was in a middle state of brain arousal during anesthesia. Yet, the exponential feature for pupil dilation appeared similarly under all brain states. These observations indicate that pupil size modulation by the LH is independently mediated from the regulation of brain states.

4.2 Methods

4.2.1 Subjects

Five Sprague Dawley rats (Strain: Crl:CD(SD), Sex: Male, Charles River Laboratories, Sulzfeld, Germany) were used for multi-modal electrophysiology experiments with optogenetics. The age of rats was 4-5 weeks at the start of the experiment when the intracranial virus-vector injection was conducted. The age of rats at the time of electrophysiology experiments was 3-6 months.

4.2.2 Stereotaxic injection of viral constructs

All surgical details for stereotaxic injection of viral vectors are described in Chapter II (see Method 2.2.2) since the same operations were performed. However, instead of using the viral construct of GCaMP, a viral vector of channelrhodopsin (AAV5.CaMKII.ChR2.mCherry) was injected at the LH (A/P= -3.20 mm, M/L= +1.50 mm, D/V= -7.70 mm) with the portion of 600 nL at a rate of 100 nL/min for optogenetic experiments.

4.2.3 Surgical procedures for multi-modal electrophysiology experiments with optogenetics

Surgical details for cannulation of the femoral artery and vein are described in Chapter II (see Method 2.2.3) and for electrode insertion in Chapter III (see Method 3.2.2) since the same operations were performed. However, an optical fiber (200 µm diameter, FT200-EMT, Thorlabs) was attached to one electrode, which was placed at the LH before insertion into the brain in order to perform optogenetics.

4.2.4 Extraction of pupil diameter in pupillometry

All details for the acquisition of pupil size are described in Chapter III (see Method 3.2.5) since the same methodological procedures were used in this experiment.

4.2.5 Electrophysiology data acquisition and analysis

Experimental details for data acquisition of electrophysiological signals are described in Chapter III (see Method 3.2.3) since the same experimental setups were used.

All acquired data from Spike 2 software was first converted to the .mat file in order to perform data analysis in Matlab. Spectral analysis was first performed using the wavelet decomposition with a specification of 0.5-100 Hz frequency band and 2 s sliding window from the raw data of electrophysiological signals. From the outcome of spectral analysis, the LFP power was extracted between 0.5-100 Hz. By using the Matlab filtfilt function, the extracted LFP power was filtered between 1-4 Hz (delta band) according to the classification of neuronal oscillations in sleep from an animal study[20].

Model fitting for exponential function and linear regression

An increment of pupil diameter and a decrement of LFP delta power with various optogenetic frequencies were evaluated by fitting values into the exponential equation using the fit function of Matlab as follows:

$$f(x) = a - b \cdot e^{-\lambda \cdot x} \tag{4.5}$$

$f(x)$ depicts LFP delta power and x depicts frequencies and optogenetic stimulation.

To compare fitting models of the same data with linear regression about changes of pupil diameter and LFP delta power, the fitlm function of Matlab was used. Furthermore, these fit and fitlm functions of Matlab computed both Akaike information criterion and adjusted R^2.

Thresholding to distinguish different brain states under anesthesia

The bootstrap method was applied to evaluate if the 5 s-averaged delta power during pre-stimulation time was due to random noise or not. Within each animal, both minimum and maximum numbers of delta power were calculated. Between these minimum

and maximum numbers, random values were produced with 10,000 times of repetition by the randi function of Matlab. Then, the average of random values was also computed with 10,000 repetitions. Finally, the distribution from randomly generated values was drawn to compare with the distribution of 5 s-averaged delta power from pre-stimulation time.

4.3 Results

4.3.1 Modulations of pupil size and electrophysiological signal by optogenetic stimulation of the LH

Optogenetics was conducted on CaMKII$^+$ neurons of the LH in five anesthetized animals with stimulation frequencies of 1 Hz, 3 Hz, 5 Hz, 10 Hz, and 20 Hz to modulate pupil size and brain states 4.1a, Figure S12). Changes of brain signals were detected through electrophysiological signals at the ACC and LH, and concurrently pupil size was monitored (Figure 4.1a, b, c). During pre-stimulation period (resting state), the power spectrogram of LFP signals from the ACC exhibited the strongest frequency between 1 and 4 Hz (Figure 4.1d). This intensity of power between 1 and 4 Hz at the ACC decreased after optogenetic stimulation at the LH was performed (Figure 4.1d). These results demonstrated that activation of LH neurons induces pupil dilation and alters ACC activity.

4.3.2 Frequency-dependent optogenetic stimulation of the LH for pupil size and brain state modulations

Here, frequency-dependent LFP reduction and pupil dilation were further evaluated to understand how the LH contributes to the simultaneous modulation of pupil size and brain states. 4 s of optogenetic stimulation at the LH induced pupil dilation, and the pupil dilated larger as the stimulation frequencies increased between 1 and 20 Hz (Maximum pupil diameter: 1 Hz $<$ 3 Hz $<$ 5 Hz $<$ 10 Hz $<$ 20 Hz, Figure 4.2a). As soon as the LH was stimulated by laser light, pupil dilation began instantly and continued through the post-stimulation period for 1.5 s(1 Hz), 7.5 s (3 Hz), 7.3 s (5 Hz), 7.5 s (10 Hz), and 8.1 s (20 Hz) (Figure 4.2a). Two-sample t-tests also confirmed that pupil diameters between pre- and post-stimulation periods differed significantly among all frequencies of stimulation ($p < 0.001$, Figure 4.2b). In particular, the maximum diameter of the pupil enlarged exponentially with an increase in stimulation frequencies between 1 and

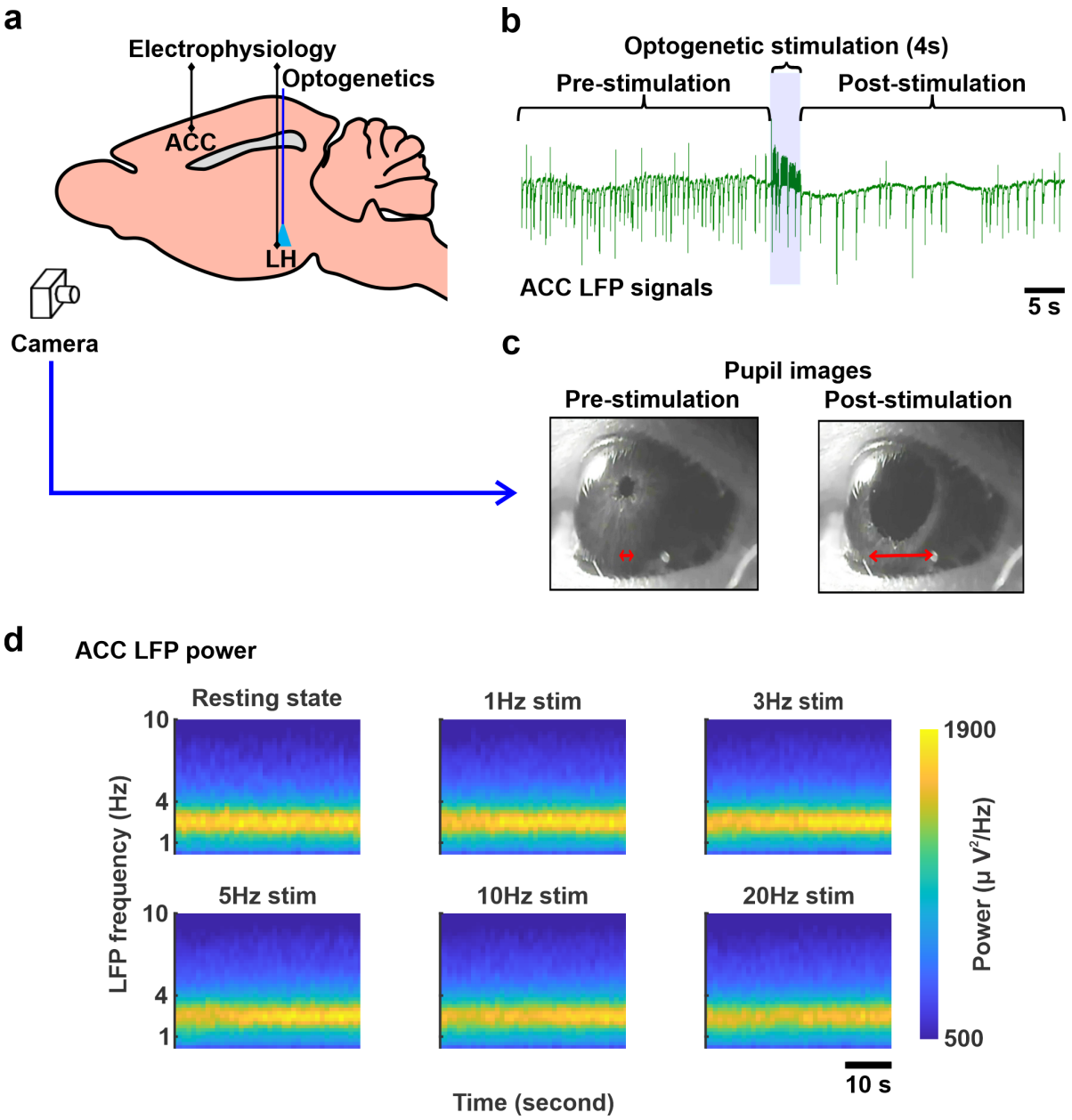

Figure 4.1 Illustrations of LFP and pupil size modulations upon optogenetic stimulation. a) The experimental setup for simultaneous electrophysiology and pupil size recordings with optogenetic stimulation. b) An representative example of ACC electrophysiological signal modulation in the ACC by optogenetic stimulation of the LH. c) sample pictures of pupil size from pre- (left) and post- (right) optogenetic stimulation periods. d) Power spectrograms of electrophysiological signals from the ACC during resting state (top left; 213 trials, 5 animals) and after 1 Hz (top middle; 355 trials, 5 animals), 3 Hz (top right; 355 trials, 5 animals), 5 Hz (bottom left; 355 trials, 5 animals), 10 Hz (bottom center; 355 trials, 5 animals), and 20 Hz (bottom right; 355 trials, 5 animals) optogenetic stimulation. The duration of the x-axis is depicted with 40 s window.

20 Hz (Figure 4.2c and Figure S13). This exponential hallmark appears stronger during pupil dilation, approximately 0-20 s of post-stimulation period (Figure S14). In fact, the adjusted R^2 for exponential function in pupil dilation exhibited higher values compared to linear regression up to 25-30 s (Table S4), indicating a better exponential fit compared to linear regression until 25-30 s. Furthermore, Akaike information criterion from a linear fit exhibited greater values in the early post-stimulation time but smaller in the late post-stimulation time (Figure S14 and Table S4), indicating that a fit model altered to linear as the post-stimulation time proceeded.

Similar to instant dilation of the pupil, optogenetic stimulation also induced LFP delta power reduction at the ACC and LH after the LH was stimulated (Figure 4.2d and Figure S15a). Moreover, the delta power decreased more with an increase in stimulation frequencies especially under a similar time span when pupil dilation occurred (Figure 4.1d, 4.2d, e, and Figure S15a, b). Two-sample t-tests confirmed that LFP delta power at the ACC from pre- stimulation period differed significantly from the duration of pupil dilation in stimulation frequencies of 5 Hz(7 s), 10 Hz(8 s), and 20 Hz(8 s) but did not differ in 1 Hz(2 s) and 3 Hz(8 s) (Figure 4.2e). Two-sample t-tests also confirmed that LFP delta power at the LH from pre-stimulation period differed significantly from the duration of pupil dilation in stimulation frequencies of 3 Hz(8 s), 5 Hz(7 s), 10 Hz(8 s), and 20 Hz(8 s) but did not differ in 1 Hz(2 s) (Figure S15b). This reduction of LFP delta power at the LH and ACC also exhibited the exponential attribute with an increase in stimulation frequencies between 1 and 20 Hz (Figure 4.2f and Figure S15c). The exponential hallmark appeared stronger for approximately 0-20 s of post-stimulation period at the ACC and 0-10 s at the LH (Figure S16a, c). The adjusted R^2 for exponential function in LFP delta power reduction exhibited higher values compared to linear regression up to 20-25 s at the ACC (Table S5), indicating a better exponential fit compared to linear regression until 25-30 s. In consistence with evaluation of the adjusted R^2, Akaike information criterion for linear regression, showing the quality of the model in a linear fit, diminished as the time proceeded from an early to late phase of post-stimulation, demonstrating that a linear model fits better in the late post-stimulation phase but not

in the early phase (Figure S16 and Table S5, S6). These findings indicate that activation frequencies of LH affect the degree of pupil dilation and cortical signal changes with the exponential trait.

4.3.3 Influence of underlying brain state differences on pupil size and LFP modulation upon optogenetics at the LH

In Section 4.3.2 when optogenetics at the LH led to pupil dilation and LFP reduction, a large variation of the maximum pupil diameter (ranging between 19-313 pixels) was observed across different recording trials but within the same stimulation frequency paradigm (355 trials in each frequency; Figure 4.3a), suggesting the existence of different brain states since pupil size is an arousal indicator. In fact, delta power in the pre-stimulation phase diversified widely across different trials within the same animal (Animal 1: 350 trials, Animal 2: 200 trials, Animal 3: 300 trials, Animal 4: 300 trials, Animal 5: 625 trials; Figure 4.3b and Figure S17). Since the magnitude of delta power or amplitude demonstrates a level of arousal under unconsciousness [1], the trials showing above 0.5 SD on the magnitude of delta power during the pre-stimulation phase were categorized as State 1, between 1 and -1 SD as State 2, and below -1 SD as State 3 within each animal (Figure 4.3b and Figure S17). Among these three states, pupil size was biggest under State 1 ($\mu = 86.27$, $S.E. = 2.75$), medium under State 2 ($\mu = 61.99$, $S.E. = 1.35$), and smallest under State 3 ($\mu = 41.51$, $S.E. = 2.70$) (Figure 4.3c). In fact, an analysis of one-way analysis of variance (ANOVA) illustrated that pupil sizes under the three states were significantly different ($p < 0.001$, $F(2, 1772) = 67.33$). In addition, the means of pupil size between State 1 and 2 or 3 ($p < 0.001$) exhibited significant differences as well as between State 2 and 3 ($p < 0.001$) upon the Tukey's HSD test (Post-hoc comparisons). The analysis of pupil size is consistent with previous reports describing that pupil size appears smaller under a low arousal state but bigger under a high arousal state [9, 195].

Among these three different states, the exponential decrement of LFP delta power at the LH and ACC emerged more notably in State 2 in comparison with State 1 and

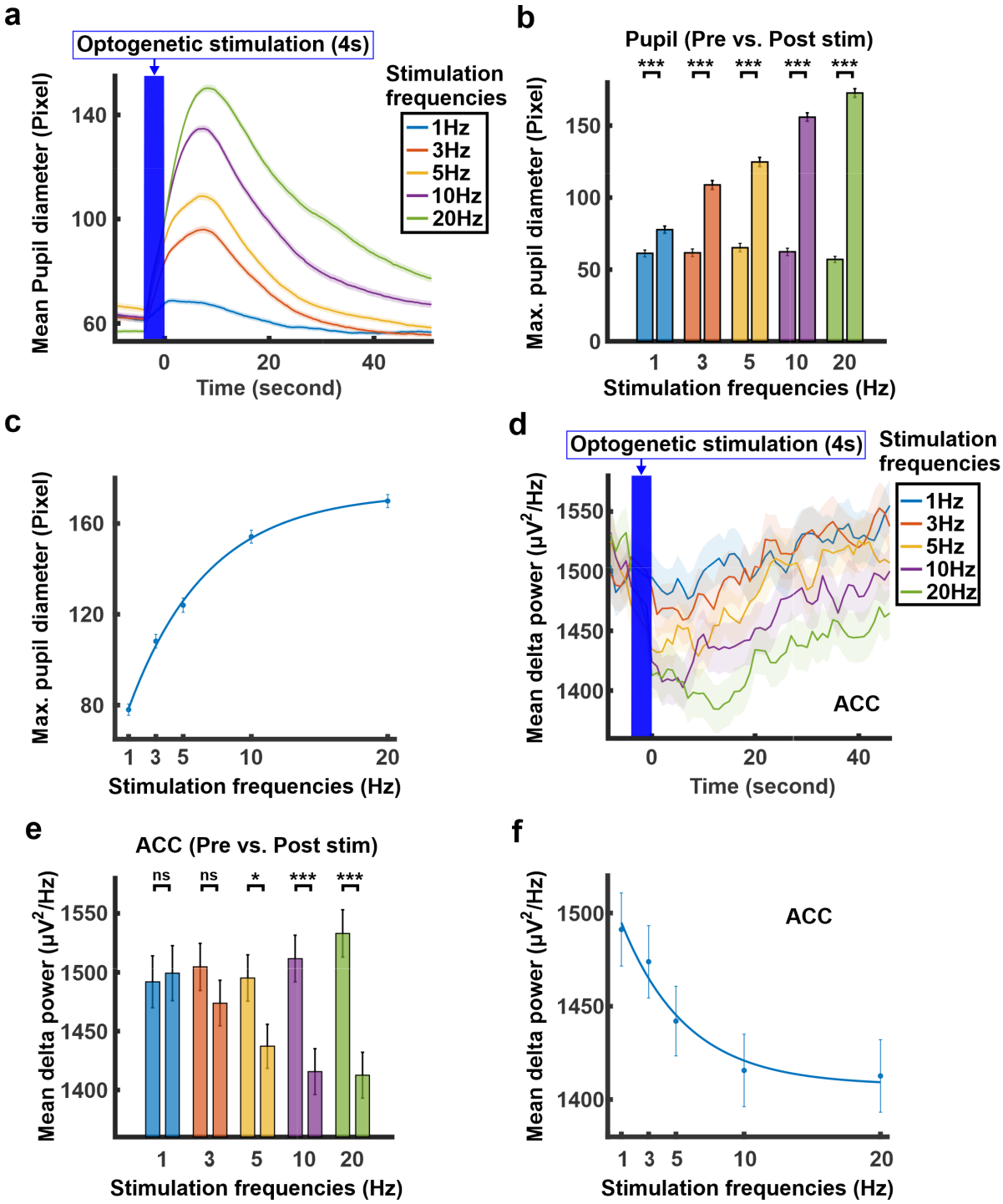

Figure 4.2 a) Mean pupil diameter upon optogenetics with different stimulation frequencies (4 s, blue:1 Hz, orange:3 Hz, yellow:5 Hz, purple:10 Hz, green:20 Hz). The standard error of mean is indicated by shaded regions. b) Bar plots of maximum pupil diameters comparing between pre- (8 s) and post- (8 s) stimulation periods (355 trials on each stimulation frequency, 5 animals). The standard error of mean is illustrated by error bars. c) Exponential fit of maximum pupil diameters from post-stimulation period (355 trials on each stimulation frequency, 5 animals). The standard error of mean is illustrated by error bars. (the caption continues to the next page)

Figure 4.2 d) Mean LFP delta power from the ACC upon optogenetics with different stimulation frequencies (4 s, blue: 1 Hz, orange: 3 Hz, yellow: 5 Hz, purple: 10 Hz, green: 20 Hz). The standard error of mean is indicated by shaded regions. e) Bar plots of LFP delta power changes from the ACC comparing between pre- (8 s) and post- (8 s) stimulation periods (355 trials on each stimulation frequency, 2 s average for 1 Hz, 8 s average for 3 Hz, 7 s average for 5 Hz, 8 s average for 10 Hz, 8 s average for 20 Hz). The standard error of mean is illustrated by error bars. f) Exponential fit of mean LFP delta power at ACC from post-stimulation period (355 trials on each stimulation frequency, 5 animals). The standard error of mean is illustrated by error bars. Note: *** $p < 0.001$, ** $p < 0.01$, * $p < 0.05$, ns: not significant.

3 (Figure 4.3d, Figure S19, and Table S7). When fitting the data into linear regression, the adjusted R^2 appeared with lower values in comparison with the exponential fit during the early post-stimulation time (Figure S20 and Table S8), demonstrating that exponential model fits better for State 2 during the early phase. In consistence with the adjusted R^2 analysis, Akaike information criterion from linear fitting diminished as the time proceeded from an early to late phase of post-stimulation, demonstrating that a linear model fits better in the late post-stimulation phase compared to the early phase (Figure S21 and Table S8). On the other hand, the adjusted R^2 of linear fitting under State 1 and 3 appeared with larger values in comparisonl with the exponential fit during the post-stimulation time(Figure S20 and Table S8), demonstrating that the linear model fits better than the exponential function during the post-stimulation time for State 1 and 3. These analyses demonstrated that differences in the initial brain state (prior to optogenetic stimulation) affected the exponential feature of LFP delta power reduction.

The exponential hallmark for an increment of maximum pupil size by optogenetics, however, emerged comparably across the three states (Figure 4.3e, f and Figure S22). This feature comprised of pupil dilation period (an early stage of post-stimulation phase) since the growth rate of exponential fit (λ in Equation 4.5) in pupil size (5 s mean) reduced in the late phase of post-stimulation time (Figure S23 and Table S10). In fact, the adjusted R^2 for 5s-averaged pupil size in linear regression appeared with lower values

in comparison with the exponential fit during the early post-stimulation time (Figure S23 and Table S11). Akaike information criterion from linear fitting also diminished as the time proceeded from an early to late stage of post-stimulation, demonstrating that a linear model fits better in the late post-stimulation phase compared to the early phase (Table S11). These outcomes illustrate that brain state differences prior to LH stimulation influence the exponential decrement of LFP delta power but leave the exponential increment of pupil size unaffected.

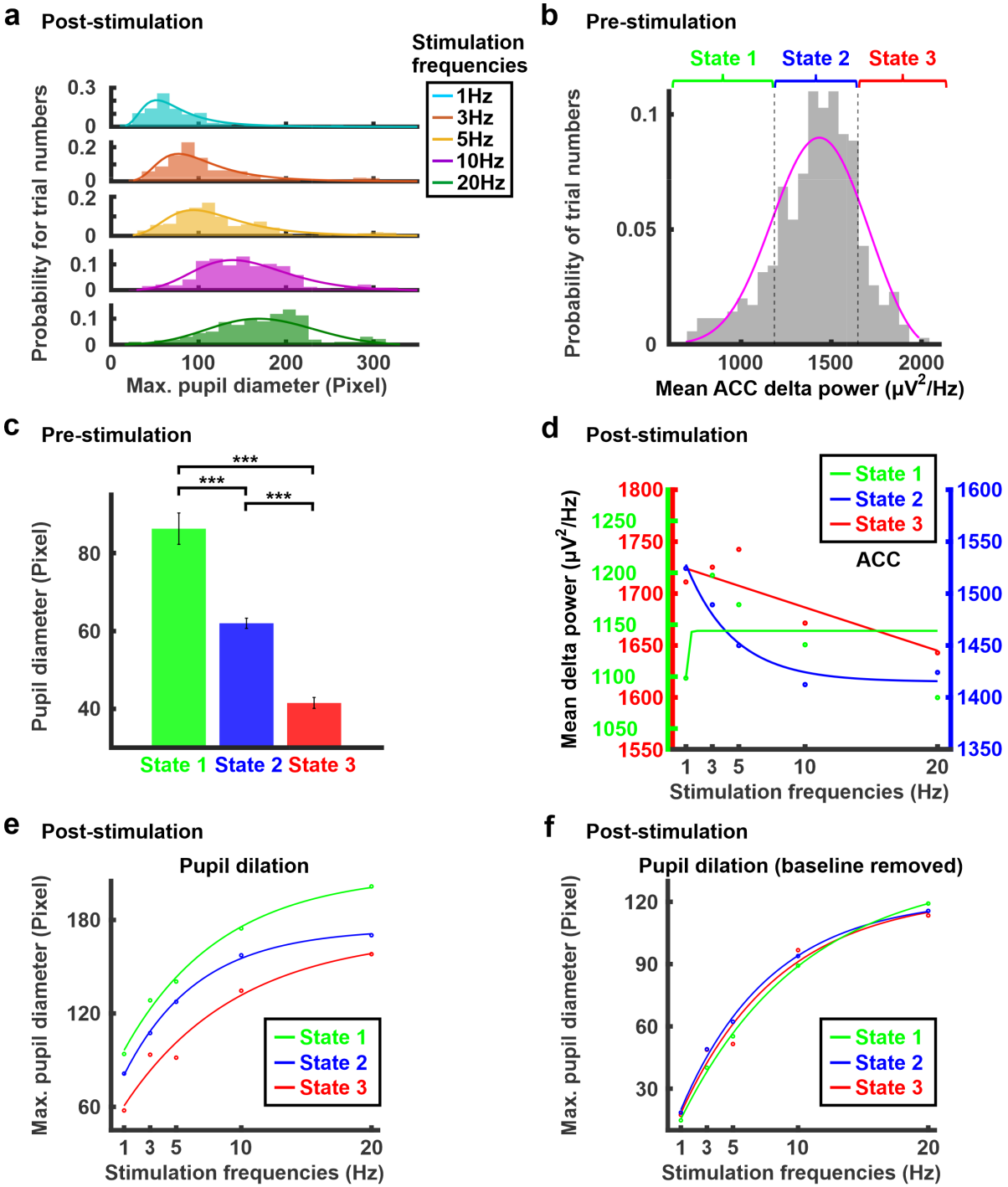

Figure 4.3 Evaluating the influence of underlying brain states on exponential increase of pupil size and decrease of LFP delta power upon optogenetics at the LH. a) The maximum pupil diameters across recording trials after optogenetics of the LH with different stimulation frequencies (light blue: 1 Hz, orange: 3 Hz, yellow: 5 Hz, purple: 10 Hz, green: 20 Hz, n=355 for each stimulation frequency). b) Delta power averaged over 5 s of pre-stimulation phase in one representative rat (350 trials). Trials below 0.5 SD are defined as State 1 (green), between 0.5 and -0.5 SD as State 2 (blue), and above 0.5 SD as State 3 (red). (the caption continues to the next page)

Figure 4.3 c) Mean pupil diameter during 5 s of the pre-stimulation phase (State 1: 547 trials, State 2: 657 trials, State 3: 571 trials). The standard error of mean is illustrated by error bars. d) Exponential fit of mean LFP delta power at ACC from post-stimulation period under the three different underlying brain states from all five animals. The number of trials is described in Table S12. e) Exponential fit of maximum pupil diameters from post-stimulation period under the three different underlying brain states in all five animals. The number of trials is described in Table S12. f) Removal of baseline pupil diameter from Figure 4.3e. Note: *** $p < 0.001$, ** $p < 0.01$, * $p < 0.05$.

4.4 Discussion

This Chapter IV provided evidence that activation of the LH by optogenetics caused an increment in pupil size and decrement in ACC LFP delta power simultaneously in anesthetized animals. The degree of these changes appeared exponentially larger as stimulation frequencies increased, demonstrating that the LH-mediated modulation of pupil size and ACC signals are activation frequency-dependent. Moreover, the exponential feature for the decrement of ACC delta power was observed upon a medium stage of arousal under anesthesia. On the other hand, the exponential hallmark of maximum pupil size always appeared in all conditions of brain arousal states. These observations indicate that pupil size regulation through the LH is independent of the underlying brain state, but modulation of the ACC signals depends on the underlying brain state.

Subcortical and brainstem regions, including the LH and LC, play an important role in tuning brain states through various neuromodulators such as orexin and noradrenergic cells [26, 157, 193]. Brain states transit from one to another spontaneously during anesthesia, sleep, or wakefulness, and these different states are commonly monitored and distinguished by concurrent physiological measurements such as fMRI, electrophysiology, and pupillometry (e.g., observation of slow wave electrophysiological signals and smaller pupil size simultaneously during a low arousal state) [5, 9, 10, 20, 196]. Thus, both pupil size and brain states are often mediated through the same regulatory pathway. For example, activation of LC neurons leads to concurrent changes of brain states and pupil size [61, 62]. Nevertheless, correlations between pupil size and neuronal activity in the LC vary across different temporal scales probably due to the impact of brain state differences [46, 47]. These indications imply that other brain regions such as the hypothalamus may contribute to mediating pupil size and brain states [63].

Pupil-regulating circuits (e.g., the LC) receive inputs from other brain state-mediating regions such as the LH [13, 83]. The LH regulates brain states through various neuronal populations (e.g., orexin and VGAT neurons) [26, 64, 157]. In spite of the fact that direct activation of arousal-mediating neurons in LH by optogenetics alters brain states [15, 74, 82, 197], the influence of LH activation on pupil size modulation is concealed.

In our study, activation of the LH neurons by optogenetics induced both pupil dilation and modulated LFP signal at the ACC (Figure 4.1b, c, 4.2a, d). The ACC is involved in brain state and pupil size regulations through interactions with neuronal projections from LC [90, 93, 198]. In addition, default mode network analysis shows that activity of the ACC varies under different brain arousal states [24]. Interestingly, the ACC also receives anatomical inputs from the LH [84]. Thus, activation of LH neurons indicates a potential to modulate both pupil size and ACC activity.

Despite evidence that the LH activation causes brain state modulation, this transition can be triggered more likely when a high stimulation frequency ($\geq 5\,\mathrm{Hz}$) is given at the LH [15, 74, 82]. In fact, our optogenetic stimulation of the LH also modulated LFP delta power at the ACC in trials when higher stimulation frequencies were given (Figure 4.2d, e). The reason behind this phenomenon of frequency-dependent changes could be due to different activation features of individual neuromodulatory populations in the LH since different stimulation frequencies lead to releasing distinct types of neurotransmitters [194]. Furthermore, our result demonstrated that this frequency-dependent modulation of ACC signal appeared as an exponential decay with the increment of stimulation frequencies (Figure 4.2f). Similar to this exponential decay, pupil dilation also showed an exponential modulation with the increment of stimulation frequencies (Figure 4.2c). Therefore, the LH regulates pupil size and ACC brain signals with similar regulatory mechanisms.

The regulatory mechanism of brain state transitions through the LH is not only influenced by stimulation frequencies of LH but also the underlying brain arousal state [15]. The brain arousal state oscillates during sleep, wakefulness, or anesthesia [1, 9, 10]. Thus, the brain holds different arousal states at every moment of each trial when optogenetic stimulation is performed. In our result, the delta power of LFP signals (indication of different arousal levels [20, 20, 199]) at the ACC appeared with large variations during pre-stimulation time (Figure 4.3b and Figure S17). Moreover, pupil size appeared smaller in the trials showing high delta power (named as State 3) but bigger in the trials showing low delta power (named as State 1) (Figure 4.3b, c). Since

both relatively low delta power/amplitude and large pupil size indicate a higher arousal state [195], our results demonstrated that the baseline arousal level varied across trials in the pre-stimulation phase.

The brain state at the time of stimulation has an impact on feasibility to cause brain state transitions upon optogenetics at the LH. For example, optogenetic stimulation of arousal-promoting neurons in the LH induces a brain state transition to high arousal during NREM sleep but it does not during REM sleep [15]. Furthermore, these underlying brain state differences give rise to different capability of behavioral performances or cortical neuronal activities, which depends on the momentum state of performance within an inverted U-shape of arousal phase [5, 9, 200, 201]. Within our spectrum of different brain states under anesthesia (Figure 4.3b), ACC responses upon optogenetcis at the LH also appeared differently, exhibiting the exponential feature of delta power reduction only under an intermediate range of anesthetized brain arousal states but the linear feature under a high or low range (Figure 4.3d). Unlike differences of different ACC responses, the exponential hallmark for pupil dilation appeared similarly under all three different brain states (Figure 4.3e, f). These observations suggest that LH-induced pupil size and brain state modulations can be driven by distinct regulatory pathways.

Overall, this Chapter IV demonstrated unique regulatory features of pupil size and brain states through LH activation. Pupil dilation and ACC LFP delta power reduction, induced by LH stimulation, showed a greater degree of modulations exponentially with the increase of stimulation frequencies. Furthermore, these exponential hallmarks were observed under an intermediate brain arousal state of anesthesia for modulation of ACC signals but under all for pupil dilation. The work here may add information on revealing unexplained variations of correlations between neuronal activities of the pupil-regulatory circuit and pupil dynamics.

5 Summary

This dissertation described three strategies aimed to better comprehend brain state and pupil size regulations through multi-modal experimental design. In Chapter II, a novel approach to track brain states was demonstrated by establishing a multi-modal setup for simultaneous fMRI, Ca^{2+} signal, and pupil size recordings. The investigation showed a unique functional network, involving pupil and arousal regulations from correlations among fMRI signal, 2-3 Hz Ca^{2+} power at the ACC, and pupil size changes. The whole brain network especially highlighted the strong correlation in the noradrenergic A5 region, which varied depending on brain states.

To further explore brain state-dependent coupling features between pupil size and whole brain fMRI signals, the study in Chapter III investigated the interactions of pupil size with LH and ACC activities since the LH shows evidence of neuronal projections to pupil- and brain state- regulatory circuits such as the ACC. Using multi-modal datasets from pupillometry, fMRI, electrophysiology, and fiber photometry Ca^{2+} recordings, we first identified that correlations of pupil dynamics with LFP and Ca^{2+} signal in the ACC or whole-brain fMRI signals depended on LH activity. Two groups of trials that showed positive or negative correlations of the LH activity with pupil dynamics presented clear differentiation for LH-ACC coupling features such as phase-locking and phase-amplitude coupling and also for the correlations among pupil size, 1-4 Hz Ca^{2+} power at the ACC, and whole-brain fMRI. The results of both electrophsiological and fMRI measurements converged to characterize distinct brain states based on pupil size and LH activity.

To investigate the contribution of LH on unique interactions between pupil size and ACC/LH activity for distinguishing different brain states, the study in Chapter

IV evaluated brain state and pupil size modulations by direct stimulation of the LH. Optogenetic stimulation of the LH led to pupil dilation and ACC LFP delta power reduction, showing clear evidence that the LH directly modulates pupil size and ACC activity. Furthermore, pupil size increased and ACC delta power decreased exponentially as a function of an increase in optogenetic stimulation frequencies between 1 and 20 Hz. This exponential attribute of ACC delta power reduction became visible only under an intermediate arousal range of anesthetized brain states at the time of stimulation. However, the exponential increase of pupil size was not influenced by differences in the underlying brain states. These outcomes suggest that LH-induced brain state and pupil size modulations are differently mediated.

Although this dissertation presented cross-scale investigations of different brain states, all findings in the evaluations here were studied under anesthesia. This might restrict the interpretation of natural brain states without anesthesia. Thus, further investigation should be performed in future research to obtain comparable results in awake animals and to validate these brain state differences without using anesthesia. Overall, exploration of brain state evaluation in this dissertation may help to disclose the diversity of brain state-dependent correlations between pupil size and neuronal activity of arousal- and pupil- mediating brain regions. This claim can be of interest to future research evaluating the nature of brain state dynamics.

6 References

[1] Brown EN, Lydic R, Schiff ND. General anesthesia, sleep, and coma. *N Engl J Med*, 2010;363(27):2638–50. doi:10.1056/NEJMra0808281

[2] Cirelli C, Tononi G. Is Sleep Essential? *PLoS Biology*, 2008;6(8):e216. doi:10.1371/journal.pbio.0060216

[3] Eban-Rothschild A, Appelbaum L, de Lecea L. Neuronal Mechanisms for Sleep/Wake Regulation and Modulatory Drive. *Neuropsychopharmacology*, 2018;43(5):937–952. doi:10.1038/npp.2017.294

[4] Anafi RC, Kayser MS, Raizen DM. Exploring phylogeny to find the function of sleep. *Nat Rev Neurosci*, 2019;20(2):109–116. doi:10.1038/s41583-018-0098-9

[5] McCormick DA, Nestvogel DB, He BJ. Neuromodulation of Brain State and Behavior. *Annu Rev Neurosci*, 2020;43:391–415. doi:10.1146/annurev-neuro-100219-105424

[6] Kringelbach ML, Deco G. Brain States and Transitions: Insights from Computational Neuroscience. *Cell Rep*, 2020;32(10):108128. doi:10.1016/j.celrep.2020.108128

[7] Steriade M, McCormick DA, Sejnowski TJ. Thalamocortical oscillations in the sleeping and aroused brain. *Science*, 1993;262(5134):679–85. doi:10.1126/science.8235588

[8] Neville KR, Haberly LB. Beta and gamma oscillations in the olfactory system of

the urethane-anesthetized rat. *J Neurophysiol*, 2003;90(6):3921–30. doi:10.1152/jn.00475.2003

[9] McGinley MJ, David SV, McCormick DA. Cortical Membrane Potential Signature of Optimal States for Sensory Signal Detection. *Neuron*, 2015;87(1):179–192. doi:10.1016/j.neuron.2015.05.038

[10] Pais-Roldan P, Takahashi K, Sobczak F, et al. Indexing brain state-dependent pupil dynamics with simultaneous fMRI and optical fiber calcium recording. *Proceedings of the National Academy of Sciences of the United States of America*, 2020;117(12):6875–6882. doi:10.1073/pnas.1909937117

[11] Poskanzer KE, Yuste R. Astrocytes regulate cortical state switching in vivo. *Proceedings of the National Academy of Sciences*, 2016;113(19). doi:10.1073/pnas.1520759113

[12] Chang C, Leopold DA, Scholvinck ML, et al. Tracking brain arousal fluctuations with fMRI. *Proc Natl Acad Sci U S A*, 2016;113(16):4518–23. doi:10.1073/pnas.1520613113

[13] Saper CB, Fuller PM, Pedersen NP, Lu J, Scammell TE. Sleep State Switching. *Neuron*, 2010;68(6):1023–1042. doi:10.1016/j.neuron.2010.11.032

[14] Fuller PM, Sherman D, Pedersen NP, Saper CB, Lu J. Reassessment of the structural basis of the ascending arousal system. *J Comp Neurol*, 2011;519(5):933–56. doi:10.1002/cne.22559

[15] Herrera CG, Cadavieco MC, Jego S, Ponomarenko A, Korotkova T, Adamantidis A. Hypothalamic feedforward inhibition of thalamocortical network controls arousal and consciousness. *Nat Neurosci*, 2016;19(2):290–8. doi:10.1038/nn.4209

[16] Blasiak T, Zawadzki A, Lewandowski MH. Infra-slow oscillation (ISO) of the pupil size of urethane-anaesthetised rats. *PLoS One*, 2013;8(4):e62430. doi:10.1371/journal.pone.0062430

[17] Kum JE, Han HB, Choi JH. Pupil Size in Relation to Cortical States during Isoflurane Anesthesia. *Experimental Neurobiology*, 2016;25(2):86–92. doi:10.5607/en.2016.25.2.86

[18] Takahashi H, Tokushige H, Shiramatsu T, Noda T, Kanzaki R. Covariation of pupillary and auditory cortical activity in rats under isoflurane anesthesia. *Neuroscience*, 2015;300:29–38. doi:10.1016/j.neuroscience.2015.05.004

[19] Purdon PL, Sampson A, Pavone KJ, Brown EN. Clinical Electroencephalography for Anesthesiologists: Part I: Background and Basic Signatures. *Anesthesiology*, 2015;123(4):937–60. doi:10.1097/ALN.0000000000000841

[20] Yuzgec O, Prsa M, Zimmermann R, Huber D. Pupil Size Coupling to Cortical States Protects the Stability of Deep Sleep via Parasympathetic Modulation. *Curr Biol*, 2018;28(3):392–400 e3. doi:10.1016/j.cub.2017.12.049

[21] Vacas S, Kurien P, Maze M. Sleep and Anesthesia - Common mechanisms of action. *Sleep Med Clin*, 2013;8(1):1–9. doi:10.1016/j.jsmc.2012.11.009

[22] Clement EA, Richard A, Thwaites M, Ailon J, Peters S, Dickson CT. Cyclic and sleep-like spontaneous alternations of brain state under urethane anaesthesia. *PLoS One*, 2008;3(4):e2004. doi:10.1371/journal.pone.0002004

[23] Yellin D, Berkovich-Ohana A, Malach R. Coupling between pupil fluctuations and resting-state fMRI uncovers a slow build-up of antagonistic responses in the human cortex. *Neuroimage*, 2015;106:414–427. doi:10.1016/j.neuroimage.2014.11.034

[24] Tarun A, Wainstein-Andriano D, Sterpenich V, et al. NREM sleep stages specifically alter dynamical integration of large-scale brain networks. *iScience*, 2021; 24(1):101923. doi:10.1016/j.isci.2020.101923

[25] Paasonen J, Stenroos P, Salo RA, Kiviniemi V, Grohn O. Functional connectivity under six anesthesia protocols and the awake condition in rat brain. *Neuroimage*, 2018;172:9–20. doi:10.1016/j.neuroimage.2018.01.014

[26] Saper CB, Scammell TE, Lu J. Hypothalamic regulation of sleep and circadian rhythms. *Nature*, 2005;437(7063):1257–63. doi:10.1038/nature04284

[27] Moruzzi G, Magoun HW. Brain stem reticular formation and activation of the EEG. *Electroencephalogr Clin Neurophysiol*, 1949;1(4):455–73

[28] Lindsley DB, Bowden JW, Magoun HW. Effect Upon the Eeg of Acute Injury to the Brain Stem Activating System. *Electroencephalography and Clinical Neurophysiology*, 1949;1(4):475–486. doi:10.1016/0013-4694(49)90068-1

[29] Starzl TE, Taylor CW, Magoun HW. COLLATERAL AFFERENT EXCITATION OF RETICULAR FORMATION OF BRAIN STEM. *Journal of Neurophysiology*, 1951;14(6):479–496. doi:10.1152/jn.1951.14.6.479

[30] Edlow BL, Takahashi E, Wu O, et al. Neuroanatomic connectivity of the human ascending arousal system critical to consciousness and its disorders. *J Neuropathol Exp Neurol*, 2012;71(6):531–46. doi:10.1097/NEN.0b013e3182588293

[31] Chandler DJ, Jensen P, McCall JG, Pickering AE, Schwarz LA, Totah NK. Redefining Noradrenergic Neuromodulation of Behavior: Impacts of a Modular Locus Coeruleus Architecture. *The Journal of Neuroscience*, 2019;39(42):8239–8249. doi:10.1523/JNEUROSCI.1164-19.2019

[32] Jones BE. Arousal and sleep circuits. *Neuropsychopharmacology*, 2020;45(1):6–20. doi:10.1038/s41386-019-0444-2

[33] Mashour GA, Alkire MT. Consciousness, anesthesia, and the thalamocortical system. *Anesthesiology*, 2013;118(1):13–5. doi:10.1097/ALN.0b013e318277a9c6

[34] Crunelli V, Hughes SW. The slow (<1 Hz) rhythm of non-REM sleep: a dialogue between three cardinal oscillators. *Nat Neurosci*, 2010;13(1):9–17. doi:10.1038/nn.2445

[35] McCormick DA, McGinley MJ, Salkoff DB. Brain state dependent activity in the

cortex and thalamus. *Curr Opin Neurobiol*, 2015;31:133–40. doi:10.1016/j.conb.2014.10.003

[36] Tsunematsu T, Patel AA, Onken A, Sakata S. State-dependent brainstem ensemble dynamics and their interactions with hippocampus across sleep states. *Elife*, 2020;9. doi:10.7554/eLife.52244

[37] Swift KM, Gross BA, Frazer MA, et al. Abnormal Locus Coeruleus Sleep Activity Alters Sleep Signatures of Memory Consolidation and Impairs Place Cell Stability and Spatial Memory. *Current Biology*, 2018;28(22):3599–+. doi:10.1016/j.cub.2018.09.054

[38] Larsen RS, Waters J. Neuromodulatory Correlates of Pupil Dilation. *Front Neural Circuits*, 2018;12:21. doi:10.3389/fncir.2018.00021

[39] Liu Y, Rodenkirch C, Moskowitz N, Schriver B, Wang Q. Dynamic Lateralization of Pupil Dilation Evoked by Locus Coeruleus Activation Results from Sympathetic, Not Parasympathetic, Contributions. *Cell Rep*, 2017;20(13):3099–3112. doi:10.1016/j.celrep.2017.08.094

[40] Corneil BD, Munoz DP. Overt responses during covert orienting. *Neuron*, 2014;82(6):1230–43. doi:10.1016/j.neuron.2014.05.040

[41] Joshi S, Gold JI. Pupil Size as a Window on Neural Substrates of Cognition. *Trends in Cognitive Sciences*, 2020;24(6):466–480. doi:10.1016/j.tics.2020.03.005

[42] Mathot S. Pupillometry: Psychology, Physiology, and Function. *J Cogn*, 2018;1(1):16. doi:10.5334/joc.18

[43] Nobukawa S, Shirama A, Takahashi T, et al. Identification of attention-deficit hyperactivity disorder based on the complexity and symmetricity of pupil diameter. *Scientific Reports*, 2021;11(1):8439. doi:10.1038/s41598-021-88191-x

[44] Aston-Jones G, Cohen JD. An integrative theory of locus coeruleus-norepinephrine

function: adaptive gain and optimal performance. *Annu Rev Neurosci*, 2005; 28:403–50. doi:10.1146/annurev.neuro.28.061604.135709

[45] Reimer J, McGinley MJ, Liu Y, et al. Pupil fluctuations track rapid changes in adrenergic and cholinergic activity in cortex. *Nat Commun*, 2016;7:13289. doi: 10.1038/ncomms13289

[46] Joshi S, Li Y, Kalwani RM, Gold JI. Relationships between Pupil Diameter and Neuronal Activity in the Locus Coeruleus, Colliculi, and Cingulate Cortex. *Neuron*, 2016;89(1):221–234. doi:10.1016/j.neuron.2015.11.028

[47] Megemont M, McBurney-Lin J, Yang H. Pupil diameter is not an accurate real-time readout of locus coeruleus activity. *Elife*, 2022;11. doi:10.7554/eLife.70510

[48] DiNuzzo M, Mascali D, Moraschi M, et al. Brain Networks Underlying Eye's Pupil Dynamics. *Frontiers in Neuroscience*, 2019;13. doi:10.3389/fnins.2019.00965

[49] Saper CB, Chou TC, Scammell TE. The sleep switch: hypothalamic control of sleep and wakefulness. *Trends Neurosci*, 2001;24(12):726–31. doi:10.1016/s0166-2236(00)02002-6

[50] Carter ME, Yizhar O, Chikahisa S, et al. Tuning arousal with optogenetic modulation of locus coeruleus neurons. *Nat Neurosci*, 2010;13(12):1526–33. doi: 10.1038/nn.2682

[51] Liu X, de Zwart JA, Schölvinck ML, et al. Subcortical evidence for a contribution of arousal to fMRI studies of brain activity. *Nature Communications*, 2018;9(1):395. doi:10.1038/s41467-017-02815-3

[52] Lindsley D, Schreiner L, Knowles W, Magoun H. Behavioral and EEG changes following chronic brain stem lesions in the cat. *Electroencephalography and Clinical Neurophysiology*, 1950;2(1-4):483–498. doi:10.1016/0013-4694(50)90086-1

[53] Villablanca J. The electrocorticogram in the chronic cerveau isolé cat. *Elec-*

troencephalography and Clinical Neurophysiology, 1965;19(6):576–586. doi:10.1016/0013-4694(65)90243-9

[54] Taylor NE, Van Dort CJ, Kenny JD, et al. Optogenetic activation of dopamine neurons in the ventral tegmental area induces reanimation from general anesthesia. *Proceedings of the National Academy of Sciences*, 2016;113(45):12826–12831. doi:10.1073/pnas.1614340113

[55] Cho JR, Treweek JB, Robinson JE, et al. Dorsal Raphe Dopamine Neurons Modulate Arousal and Promote Wakefulness by Salient Stimuli. *Neuron*, 2017;94(6):1205–1219.e8. doi:10.1016/j.neuron.2017.05.020

[56] de Lecea L. Optogenetic control of hypocretin (orexin) neurons and arousal circuits. *Curr Top Behav Neurosci*, 2015;25:367–78. doi:10.1007/7854_2014_364

[57] Tyree S, Luis De Lecea. Optogenetic Investigation of Arousal Circuits. *International Journal of Molecular Sciences*, 2017;18(8):1773. doi:10.3390/ijms18081773

[58] Solt K, Van Dort CJ, Chemali JJ, Taylor NE, Kenny JD, Brown EN. Electrical Stimulation of the Ventral Tegmental Area Induces Reanimation from General Anesthesia. *Anesthesiology*, 2014;121(2):311–319. doi:10.1097/ALN.0000000000000117

[59] Szabadi E. Functional Organization of the Sympathetic Pathways Controlling the Pupil: Light-Inhibited and Light-Stimulated Pathways. *Front Neurol*, 2018;9:1069. doi:10.3389/fneur.2018.01069

[60] Nattie E, Li A. Respiration and autonomic regulation and orexin. In *Progress in Brain Research*, volume 198, pages 25–46. Elsevier. ISBN 978-0-444-59489-1, 2012;doi:10.1016/B978-0-444-59489-1.00004-5

[61] Hayat H, Regev N, Matosevich N, et al. Locus coeruleus norepinephrine activity mediates sensory-evoked awakenings from sleep. *Sci Adv*, 2020;6(15):eaaz4232. doi:10.1126/sciadv.aaz4232

[62] Lovett-Barron M, Andalman AS, Allen WE, et al. Ancestral Circuits for the Coordinated Modulation of Brain State. *Cell*, 2017;171(6):1411–1423 e17. doi: 10.1016/j.cell.2017.10.021

[63] Costa VD, Rudebeck PH. More than Meets the Eye: the Relationship between Pupil Size and Locus Coeruleus Activity. *Neuron*, 2016;89(1):8–10. doi:10.1016/j.neuron.2015.12.031

[64] Bonnavion P, Mickelsen LE, Fujita A, de Lecea L, Jackson AC. Hubs and spokes of the lateral hypothalamus: cell types, circuits and behaviour. *J Physiol*, 2016; 594(22):6443–6462. doi:10.1113/JP271946

[65] Kelz MB, Sun Y, Chen J, et al. An essential role for orexins in emergence from general anesthesia. *Proc Natl Acad Sci U S A*, 2008;105(4):1309–14. doi:10.1073/pnas.0707146105

[66] Yin L, Li L, Deng J, et al. Optogenetic/Chemogenetic Activation of GABAergic Neurons in the Ventral Tegmental Area Facilitates General Anesthesia via Projections to the Lateral Hypothalamus in Mice. *Front Neural Circuits*, 2019;13:73. doi:10.3389/fncir.2019.00073

[67] Sakurai T, Amemiya A, Ishii M, et al. Orexins and orexin receptors: a family of hypothalamic neuropeptides and G protein-coupled receptors that regulate feeding behavior. *Cell*, 1998;92(4):573–85. doi:10.1016/s0092-8674(00)80949-6

[68] de Lecea L, Kilduff TS, Peyron C, et al. The hypocretins: hypothalamus-specific peptides with neuroexcitatory activity. *Proc Natl Acad Sci U S A*, 1998;95(1):322–7. doi:10.1073/pnas.95.1.322

[69] Chemelli RM, Willie JT, Sinton CM, et al. Narcolepsy in orexin knockout mice: molecular genetics of sleep regulation. *Cell*, 1999;98(4):437–51. doi: 10.1016/s0092-8674(00)81973-x

[70] Lin L, Faraco J, Li R, et al. The sleep disorder canine narcolepsy is caused by

a mutation in the hypocretin (orexin) receptor 2 gene. *Cell*, 1999;98(3):365–376. doi:10.1016/S0092-8674(00)81965-0

[71] Peyron C, Faraco J, Rogers W, et al. A mutation in a case of early onset narcolepsy and a generalized absence of hypocretin peptides in human narcoleptic brains. *Nat Med*, 2000;6(9):991–7. doi:10.1038/79690

[72] Thannickal TC, Moore RY, Nienhuis R, et al. Reduced number of hypocretin neurons in human narcolepsy. *Neuron*, 2000;27(3):469–74. doi:10.1016/s0896-6273(00)00058-1

[73] Lee MG, Hassani OK, Jones BE. Discharge of identified orexin/hypocretin neurons across the sleep-waking cycle. *J Neurosci*, 2005;25(28):6716–20. doi:10.1523/JNEUROSCI.1887-05.2005

[74] Adamantidis AR, Zhang F, Aravanis AM, Deisseroth K, de Lecea L. Neural substrates of awakening probed with optogenetic control of hypocretin neurons. *Nature*, 2007;450(7168):420–4. doi:10.1038/nature06310

[75] Tsunematsu T, Kilduff TS, Boyden ES, Takahashi S, Tominaga M, Yamanaka A. Acute Optogenetic Silencing of Orexin/Hypocretin Neurons Induces Slow-Wave Sleep in Mice. *Journal of Neuroscience*, 2011;31(29):10529–10539. doi:10.1523/JNEUROSCI.0784-11.2011

[76] Wang RF, Guo H, Jiang SY, et al. Control of wakefulness by lateral hypothalamic glutamatergic neurons in male mice. *J Neurosci Res*, 2021;99(6):1689–1703. doi:10.1002/jnr.24828

[77] Broberger C, De Lecea L, Sutcliffe JG, Hokfelt T. Hypocretin/orexin- and melanin-concentrating hormone-expressing cells form distinct populations in the rodent lateral hypothalamus: relationship to the neuropeptide Y and agouti gene-related protein systems. *J Comp Neurol*, 1998;402(4):460–74

[78] Hassani OK, Lee MG, Jones BE. Melanin-concentrating hormone neurons dis-

charge in a reciprocal manner to orexin neurons across the sleep-wake cycle. *Proc Natl Acad Sci U S A*, 2009;106(7):2418–22. doi:10.1073/pnas.0811400106

[79] Konadhode RR, Pelluru D, Blanco-Centurion C, et al. Optogenetic stimulation of MCH neurons increases sleep. *J Neurosci*, 2013;33(25):10257–63. doi:10.1523/JNEUROSCI.1225-13.2013

[80] Hassani OK, Lee MG, Henny P, Jones BE. Discharge Profiles of Identified GABAergic in Comparison to Cholinergic and Putative Glutamatergic Basal Forebrain Neurons across the Sleep-Wake Cycle. *Journal of Neuroscience*, 2009; 29(38):11828–11840. doi:10.1523/Jneurosci.1259-09.2009

[81] Jego S, Glasgow SD, Herrera CG, et al. Optogenetic identification of a rapid eye movement sleep modulatory circuit in the hypothalamus. *Nat Neurosci*, 2013; 16(11):1637–43. doi:10.1038/nn.3522

[82] Carter ME, Adamantidis A, Ohtsu H, Deisseroth K, de Lecea L. Sleep homeostasis modulates hypocretin-mediated sleep-to-wake transitions. *J Neurosci*, 2009; 29(35):10939–49. doi:10.1523/JNEUROSCI.1205-09.2009

[83] Mahler SV, Moorman DE, Smith RJ, James MH, Aston-Jones G. Motivational activation: a unifying hypothesis of orexin/hypocretin function. *Nat Neurosci*, 2014;17(10):1298–303. doi:10.1038/nn.3810

[84] Jin J, Chen Q, Qiao Q, et al. Orexin neurons in the lateral hypothalamus project to the medial prefrontal cortex with a rostro-caudal gradient. *Neurosci Lett*, 2016; 621:9–14. doi:10.1016/j.neulet.2016.04.002

[85] Tyree SM, de Lecea L. Lateral Hypothalamic Control of the Ventral Tegmental Area: Reward Evaluation and the Driving of Motivated Behavior. *Frontiers in Systems Neuroscience*, 2017;11:50. doi:10.3389/fnsys.2017.00050

[86] RANSON SW, MAGOUN HW. RESPIRATORY AND PUPILLARY REACTIONS: INDUCED BY ELECTRICAL STIMULATION OF THE HYPOTHA-

LAMUS. *Archives of Neurology & Psychiatry*, 1933;29(6):1179–1194. doi: 10.1001/archneurpsyc.1933.02240120002001

[87] Johansson B, Balkenius C. A computational model of pupil dilation. *Connection Science*, 2018;30(1):5–19. doi:10.1080/09540091.2016.1271401

[88] van Heukelum S, Mars RB, Guthrie M, et al. Where is Cingulate Cortex? A Cross-Species View. *Trends in Neurosciences*, 2020;43(5):285–299. doi:10.1016/j.tins.2020.03.007

[89] Stevens FL, Hurley RA, Taber KH. Anterior cingulate cortex: unique role in cognition and emotion. *J Neuropsychiatry Clin Neurosci*, 2011;23(2):121–5. doi: 10.1176/appi.neuropsych.23.2.121

[90] Gompf HS, Mathai C, Fuller PM, et al. Locus ceruleus and anterior cingulate cortex sustain wakefulness in a novel environment. *J Neurosci*, 2010;30(43):14543–51. doi:10.1523/JNEUROSCI.3037-10.2010

[91] Lu HB, Zou QH, Gu H, Raichle ME, Stein EA, Yang YH. Rat brains also have a default mode network. *Proceedings of the National Academy of Sciences of the United States of America*, 2012;109(10):3979–3984. doi:10.1073/pnas.1200506109

[92] Horovitz SG, Braun AR, Carr WS, et al. Decoupling of the brain's default mode network during deep sleep. *Proceedings of the National Academy of Sciences of the United States of America*, 2009;106(27):11376–11381. doi:10.1073/pnas.0901435106

[93] Rudebeck PH, Putnam PT, Daniels TE, et al. A role for primate subgenual cingulate cortex in sustaining autonomic arousal. *Proceedings of the National Academy of Sciences of the United States of America*, 2014;111(14):5391–5396. doi:10.1073/pnas.1317695111

[94] Duyn JH. EEG-fMRI Methods for the Study of Brain Networks during Sleep. *Frontiers in Neurology*, 2012;3. doi:10.3389/fneur.2012.00100

[95] Lee JH, Durand R, Gradinaru V, et al. Global and local fMRI signals driven by neurons defined optogenetically by type and wiring. *Nature*, 2010;465(7299):788–792. doi:10.1038/nature09108

[96] Desai M, Kahn I, Knoblich U, et al. Mapping brain networks in awake mice using combined optical neural control and fMRI. *Journal of Neurophysiology*, 2011; 105(3):1393–1405. doi:10.1152/jn.00828.2010

[97] Senzai Y, Fernandez-Ruiz A, Buzsáki G. Layer-Specific Physiological Features and Interlaminar Interactions in the Primary Visual Cortex of the Mouse. *Neuron*, 2019;101(3):500–513.e5. doi:10.1016/j.neuron.2018.12.009

[98] Einevoll GT, Kayser C, Logothetis NK, Panzeri S. Modelling and analysis of local field potentials for studying the function of cortical circuits. *Nature Reviews Neuroscience*, 2013;14(11):770–785. doi:10.1038/nrn3599

[99] Timofeev I, Chauvette S. Thalamocortical Oscillations: Local Control of EEG Slow Waves. *Current Topics in Medicinal Chemistry*, 2011;11(19):2457–2471. doi: 10.2174/156802611797470376

[100] Tanaka T, Nakamura KC. Focal inputs are a potential origin of local field potential (LFP) in the brain regions without laminar structure. *PLOS ONE*, 2019; 14(12):e0226028. doi:10.1371/journal.pone.0226028

[101] Brazhnik E, McCoy AJ, Novikov N, Hatch CE, Walters JR. Ventral Medial Thalamic Nucleus Promotes Synchronization of Increased High Beta Oscillatory Activity in the Basal Ganglia–Thalamocortical Network of the Hemiparkinsonian Rat. *The Journal of Neuroscience*, 2016;36(15):4196–4208. doi: 10.1523/JNEUROSCI.3582-15.2016

[102] Schiff ND, Shah SA, Hudson AE, Nauvel T, Kalik SF, Purpura KP. Gating of attentional effort through the central thalamus. *Journal of Neurophysiology*, 2013; 109(4):1152–1163. doi:10.1152/jn.00317.2011

[103] Magill PJ, Sharott A, Bolam JP, Brown P. Brain State–Dependency of Coherent Oscillatory Activity in the Cerebral Cortex and Basal Ganglia of the Rat. *Journal of Neurophysiology*, 2004;92(4):2122–2136. doi:10.1152/jn.00333.2004

[104] Avila I, Parr-Brownlie LC, Brazhnik E, Castañeda E, Bergstrom DA, Walters JR. Beta frequency synchronization in basal ganglia output during rest and walk in a hemiparkinsonian rat. *Experimental Neurology*, 2010;221(2):307–319. doi:10.1016/j.expneurol.2009.11.016

[105] Lemaire N, Hernandez LF, Hu D, Kubota Y, Howe MW, Graybiel AM. Effects of dopamine depletion on LFP oscillations in striatum are task- and learning-dependent and selectively reversed by l -DOPA. *Proceedings of the National Academy of Sciences*, 2012;109(44):18126–18131. doi:10.1073/pnas.1216403109

[106] Goldberg JA. Spike Synchronization in the Cortex-Basal Ganglia Networks of Parkinsonian Primates Reflects Global Dynamics of the Local Field Potentials. *Journal of Neuroscience*, 2004;24(26):6003–6010. doi:10.1523/JNEUROSCI.4848-03.2004

[107] Carus-Cadavieco M, Gorbati M, Ye L, et al. Gamma oscillations organize top-down signalling to hypothalamus and enable food seeking. *Nature*, 2017;542(7640):232–236. doi:10.1038/nature21066

[108] Noritake A, Ninomiya T, Isoda M. Representation of distinct reward variables for self and other in primate lateral hypothalamus. *Proc Natl Acad Sci U S A*, 2020;117(10):5516–5524. doi:10.1073/pnas.1917156117

[109] Sere P, Zsigri N, Raffai T, et al. Activity of the Lateral Hypothalamus during Genetically Determined Absence Seizures. *Int J Mol Sci*, 2021;22(17). doi:10.3390/ijms22179466

[110] Vergnes M, Marescaux C, Depaulis A. Mapping of spontaneous spike and wave

discharges in Wistar rats with genetic generalized non-convulsive epilepsy. *Brain Res*, 1990;523(1):87–91. doi:10.1016/0006-8993(90)91638-w

[111] Florin E. *Causality Measures Between Neural Signals from Invasively and Non-invasively Obtained Local Field Potentials in Humans*. Forschungszentrum, Zentralbibliothek, 2010. ISBN 978-3-89336-646-0

[112] Katzner S, Nauhaus I, Benucci A, Bonin V, Ringach DL, Carandini M. Local origin of field potentials in visual cortex. *Neuron*, 2009;61(1):35–41. doi:10.1016/j.neuron.2008.11.016

[113] Rasch M, Logothetis NK, Kreiman G. From neurons to circuits: linear estimation of local field potentials. *J Neurosci*, 2009;29(44):13785–96. doi:10.1523/JNEUROSCI.2390-09.2009

[114] Berens P, Keliris GA, Ecker AS, Logothetis NK, Tolias AS. Feature selectivity of the gamma-band of the local field potential in primate primary visual cortex. *Front Neurosci*, 2008;2(2):199–207. doi:10.3389/neuro.01.037.2008

[115] Kajikawa Y, Schroeder CE. How Local Is the Local Field Potential? *Neuron*, 2011;72(5):847–858. doi:10.1016/j.neuron.2011.09.029

[116] Juergens E, Guettler A, Eckhorn R. Visual stimulation elicits locked and induced gamma oscillations in monkey intracortical- and EEG-potentials, but not in human EEG. *Exp Brain Res*, 1999;129(2):247–59. doi:10.1007/s002210050895

[117] Konno D, Ikegaya Y, Sasaki T. Weak representation of awake/sleep states by local field potentials in aged mice. *Scientific Reports*, 2022;12(1):7766. doi:10.1038/s41598-022-11888-0

[118] Abhang PA, Gawali BW, Mehrotra SC. Technological Basics of EEG Recording and Operation of Apparatus. In *Introduction to EEG- and Speech-Based Emotion Recognition*, pages 19–50. Elsevier. ISBN 978-0-12-804490-2, 2016;doi:10.1016/B978-0-12-804490-2.00002-6

[119] Sazgar M, Young MG. Normal EEG Awake and Sleep. In *Absolute Epilepsy and EEG Rotation Review*, pages 127–139. Springer International Publishing, Cham. ISBN 978-3-030-03510-5 978-3-030-03511-2, 2019;doi:10.1007/978-3-030-03511-2_6

[120] Sanchez-Vives MV, McCormick DA. Cellular and network mechanisms of rhythmic recurrent activity in neocortex. *Nat Neurosci*, 2000;3(10):1027–34. doi:10.1038/79848

[121] Ogawa S, Lee TM, Kay AR, Tank DW. Brain magnetic resonance imaging with contrast dependent on blood oxygenation. *Proceedings of the National Academy of Sciences*, 1990;87(24):9868–9872. doi:10.1073/pnas.87.24.9868

[122] Logothetis NK. What we can do and what we cannot do with fMRI. *Nature*, 2008;453(7197):869–878. doi:10.1038/nature06976

[123] Arthurs OJ, Boniface S. How well do we understand the neural origins of the fMRI BOLD signal? *Trends in Neurosciences*, 2002;25(1):27–31. doi:10.1016/S0166-2236(00)01995-0

[124] Biswal B, Yetkin FZ, Haughton VM, Hyde JS. Functional connectivity in the motor cortex of resting human brain using echo-planar MRI. *Magn Reson Med*, 1995;34(4):537–41. doi:10.1002/mrm.1910340409

[125] Raichle ME, Snyder AZ. A default mode of brain function: A brief history of an evolving idea. *NeuroImage*, 2007;37(4):1083–1090. doi:10.1016/j.neuroimage.2007.02.041

[126] Logothetis NK, Pauls J, Augath M, Trinath T, Oeltermann A. Neurophysiological investigation of the basis of the fMRI signal. *Nature*, 2001;412(6843):150–7. doi:10.1038/35084005

[127] Magri C, Schridde U, Murayama Y, Panzeri S, Logothetis NK. The amplitude and timing of the BOLD signal reflects the relationship between local field potential

power at different frequencies. *J Neurosci*, 2012;32(4):1395–407. doi:10.1523/JNEUROSCI.3985-11.2012

[128] Pais-Roldán P, Edlow BL, Jiang Y, Stelzer J, Zou M, Yu X. Multimodal assessment of recovery from coma in a rat model of diffuse brainstem tegmentum injury. *NeuroImage*, 2019;189:615–630. doi:10.1016/j.neuroimage.2019.01.060

[129] Biswal BB, Kylen JV, Hyde JS. Simultaneous assessment of flow and BOLD signals in resting-state functional connectivity maps. *NMR in Biomedicine*, 1997;10(4-5):165–170. doi:10.1002/(SICI)1099-1492(199706/08)10:4/5<165::AID-NBM454>3.0.CO;2-7

[130] Stosiek C, Garaschuk O, Holthoff K, Konnerth A. *In vivo* two-photon calcium imaging of neuronal networks. *Proceedings of the National Academy of Sciences*, 2003;100(12):7319–7324. doi:10.1073/pnas.1232232100

[131] Adelsberger H, Garaschuk O, Konnerth A. Cortical calcium waves in resting newborn mice. *Nature Neuroscience*, 2005;8(8):988–990. doi:10.1038/nn1502

[132] Shimomura O, Johnson FH, Saiga Y. Extraction, Purification and Properties of Aequorin, a Bioluminescent Protein from the Luminous Hydromedusan,Aequorea. *Journal of Cellular and Comparative Physiology*, 1962;59(3):223–239. doi:10.1002/jcp.1030590302

[133] Nakai J, Ohkura M, Imoto K. A high signal-to-noise Ca2+ probe composed of a single green fluorescent protein. *Nature Biotechnology*, 2001;19(2):137–141. doi:10.1038/84397

[134] Chen TW, Wardill TJ, Sun Y, et al. Ultrasensitive fluorescent proteins for imaging neuronal activity. *Nature*, 2013;499(7458):295–300. doi:10.1038/nature12354

[135] Barnett LM, Hughes TE, Drobizhev M. Deciphering the molecular mechanism responsible for GCaMP6m's Ca2+-dependent change in fluorescence. *PLOS ONE*, 2017;12(2):e0170934. doi:10.1371/journal.pone.0170934

[136] Kerr JND, Denk W. Imaging in vivo: watching the brain in action. *Nature Reviews Neuroscience*, 2008;9(3):195–205. doi:10.1038/nrn2338

[137] Mank M, Santos AF, Direnberger S, et al. A genetically encoded calcium indicator for chronic in vivo two-photon imaging. *Nature Methods*, 2008;5(9):805–811. doi:10.1038/nmeth.1243

[138] Homma R, Baker BJ, Jin L, et al. Wide-field and two-photon imaging of brain activity with voltage- and calcium-sensitive dyes. *Philosophical Transactions of the Royal Society B: Biological Sciences*, 2009;364(1529):2453–2467. doi:10.1098/rstb.2009.0084

[139] Schulz K, Sydekum E, Krueppel R, et al. Simultaneous BOLD fMRI and fiber-optic calcium recording in rat neocortex. *Nat Methods*, 2012;9(6):597–602. doi:10.1038/nmeth.2013

[140] Wang MS, He Y, Sejnowski TJ, Yu X. Brain-state dependent astrocytic Ca2+ signals are coupled to both positive and negative BOLD-fMRI signals. *Proceedings of the National Academy of Sciences of the United States of America*, 2018;115(7):E1647–E1656. doi:10.1073/pnas.1711692115

[141] Boyden ES, Zhang F, Bamberg E, Nagel G, Deisseroth K. Millisecond-timescale, genetically targeted optical control of neural activity. *Nat Neurosci*, 2005;8(9):1263–8. doi:10.1038/nn1525

[142] Deisseroth K. Optogenetics. *Nature Methods*, 2011;8(1):26–29. doi:10.1038/nmeth.f.324

[143] Deisseroth K. Optogenetics: 10 years of microbial opsins in neuroscience. *Nature Neuroscience*, 2015;18(9):1213–1225. doi:10.1038/nn.4091

[144] Yizhar O, Fenno L, Davidson T, Mogri M, Deisseroth K. Optogenetics in Neural Systems. *Neuron*, 2011;71(1):9–34. doi:10.1016/j.neuron.2011.06.004

[145] Nagel G, Ollig D, Fuhrmann M, et al. Channelrhodopsin-1: A Light-Gated Proton Channel in Green Algae. *Science*, 2002;296(5577):2395–2398. doi:10.1126/science.1072068

[146] Matsuno-Yagi A, Mukohata Y. Two possible roles of bacteriorhodopsin; a comparative study of strains of Halobacterium halobium differing in pigmentation. *Biochemical and Biophysical Research Communications*, 1977;78(1):237–243. doi:10.1016/0006-291X(77)91245-1

[147] Packer AM, Roska B, Häusser M. Targeting neurons and photons for optogenetics. *Nature Neuroscience*, 2013;16(7):805–815. doi:10.1038/nn.3427

[148] Parr-Brownlie LC, Bosch-Bouju C, Schoderboeck L, Sizemore RJ, Abraham WC, Hughes SM. Lentiviral vectors as tools to understand central nervous system biology in mammalian model organisms. *Frontiers in Molecular Neuroscience*, 2015;8. doi:10.3389/fnmol.2015.00014

[149] Cazettes F, Reato D, Morais JP, Renart A, Mainen ZF. Phasic Activation of Dorsal Raphe Serotonergic Neurons Increases Pupil Size. *Current Biology*, 2021;31(1):192–197.e4. doi:10.1016/j.cub.2020.09.090

[150] Mukamel R, Gelbard H, Arieli A, Hasson U, Fried I, Malach R. Coupling between neuronal firing, field potentials, and fMR1 in human auditory cortex. *Science*, 2005;309(5736):951–954. doi:10.1126/science.1110913

[151] Conner CR, Ellmore TM, Pieters TA, DiSano MA, Tandon N. Variability of the Relationship between Electrophysiology and BOLD-fMRI across Cortical Regions in Humans. *Journal of Neuroscience*, 2011;31(36):12855–12865. doi:10.1523/Jneurosci.1457-11.2011

[152] He BJ, Snyder AZ, Zempel JM, Smyth MD, Raichle ME. Electrophysiological correlates of the brain's intrinsic large-scale functional architecture. *Proc Natl Acad Sci U S A*, 2008;105(41):16039–44. doi:10.1073/pnas.0807010105

[153] Scholvinck ML, Maier A, Ye FQ, Duyn JH, Leopold DA. Neural basis of global resting-state fMRI activity. *Proc Natl Acad Sci U S A*, 2010;107(22):10238–43. doi:10.1073/pnas.0913110107

[154] Hutchison RM, Hashemi N, Gati JS, Menon RS, Everling S. Electrophysiological signatures of spontaneous BOLD fluctuations in macaque prefrontal cortex. *Neuroimage*, 2015;113:257–67. doi:10.1016/j.neuroimage.2015.03.062

[155] Jaime S, Gu H, Sadacca BF, et al. Delta Rhythm Orchestrates the Neural Activity Underlying the Resting State BOLD Signal via Phase-amplitude Coupling. *Cereb Cortex*, 2019;29(1):119–133. doi:10.1093/cercor/bhx310

[156] Watson BO, Ding M, Buzsaki G. Temporal coupling of field potentials and action potentials in the neocortex. *Eur J Neurosci*, 2018;48(7):2482–2497. doi:10.1111/ejn.13807

[157] Lee SH, Dan Y. Neuromodulation of brain states. *Neuron*, 2012;76(1):209–22. doi:10.1016/j.neuron.2012.09.012

[158] Liu X, Yanagawa T, Leopold DA, et al. Arousal transitions in sleep, wakefulness, and anesthesia are characterized by an orderly sequence of cortical events. *NeuroImage*, 2015;116:222–231. doi:10.1016/j.neuroimage.2015.04.003

[159] Sobczak F, Pais-Roldán P, Takahashi K, Yu X. Decoding the brain state-dependent relationship between pupil dynamics and resting state fMRI signal fluctuation. *eLife*, 2021;10:e68980. doi:10.7554/eLife.68980

[160] Fox MD. Clinical applications of resting state functional connectivity. *Frontiers in Systems Neuroscience*, 2010;doi:10.3389/fnsys.2010.00019

[161] Dacosta-Aguayo R, Graña M, Savio A, et al. Prognostic value of changes in resting-state functional connectivity patterns in cognitive recovery after stroke: A 3T fMRI pilot study. *Human Brain Mapping*, 2014;35(8):3819–3831. doi:10.1002/hbm.22439

[162] Jandric D, Doshi A, Scott R, et al. A Systematic Review of Resting-State Functional MRI Connectivity Changes and Cognitive Impairment in Multiple Sclerosis. *Brain Connectivity*, 2021;page brain.2021.0104. doi:10.1089/brain.2021.0104

[163] Cabral J, Kringelbach ML, Deco G. Exploring the network dynamics underlying brain activity during rest. *Progress in Neurobiology*, 2014;114:102–131. doi:10.1016/j.pneurobio.2013.12.005

[164] Vincent JL, Patel GH, Fox MD, et al. Intrinsic functional architecture in the anaesthetized monkey brain. *Nature*, 2007;447(7140):83–86. doi:10.1038/nature05758

[165] Schneider M, Hathway P, Leuchs L, Samann PG, Czisch M, Spoormaker VI. Spontaneous pupil dilations during the resting state are associated with activation of the salience network. *Neuroimage*, 2016;139:189–201. doi:10.1016/j.neuroimage.2016.06.011

[166] Murphy PR, O'Connell RG, O'Sullivan M, Robertson IH, Balsters JH. Pupil diameter covaries with BOLD activity in human locus coeruleus. *Human Brain Mapping*, 2014;35(8):4140–4154. doi:10.1002/hbm.22466

[167] Paxinos G, Watson C. *The rat brain in stereotaxic coordinates*. Academic Press/Elsevier, Amsterdam ; Boston ;, 6th edition, 2007. ISBN 9780125476126 (spiral binding) 0125476124 (spiral binding) 9780123737212 (CD-ROM) 0123737214 (CD-ROM)

[168] Mathis A, Mamidanna P, Cury KM, et al. DeepLabCut: markerless pose estimation of user-defined body parts with deep learning. *Nat Neurosci*, 2018;21(9):1281–1289. doi:10.1038/s41593-018-0209-y

[169] Nath T, Mathis A, Chen AC, Patel A, Bethge M, Mathis MW. Using DeepLabCut for 3D markerless pose estimation across species and behaviors. *Nature Protocols*, 2019;14(7):2152–2176. doi:10.1038/s41596-019-0176-0

[170] Cox RW. AFNI: software for analysis and visualization of functional magnetic

resonance neuroimages. *Comput Biomed Res*, 1996;29(3):162–73. doi:10.1006/cbmr.1996.0014

[171] Bruinstroop E, Cano G, Vanderhorst VG, et al. Spinal projections of the A5, A6 (locus coeruleus), and A7 noradrenergic cell groups in rats. *The Journal of Comparative Neurology*, 2012;520(9):1985–2001. doi:10.1002/cne.23024

[172] Byrum CE, Guyenet PG. Afferent and efferent connections of the A5 noradrenergic cell group in the rat. *The Journal of Comparative Neurology*, 1987;261(4):529–542. doi:10.1002/cne.902610406

[173] Fenik V, Marchenko V, Janssen P, Davies RO, Kubin L. A5 cells are silenced when REM sleep-like signs are elicited by pontine carbachol. *Journal of Applied Physiology*, 2002;93(4):1448–1456. doi:10.1152/japplphysiol.00225.2002

[174] He Y, Wang M, Chen X, et al. Ultra-Slow Single-Vessel BOLD and CBV-Based fMRI Spatiotemporal Dynamics and Their Correlation with Neuronal Intracellular Calcium Signals. *Neuron*, 2018;97(4):925–939 e5. doi:10.1016/j.neuron.2018.01.025

[175] Takahashi K, Sobczak F, Pais-Roldán P, Yu X. Characterizing pupil dynamics coupling to brain state fluctuation based on lateral hypothalamic activity. preprint, Neuroscience, 2021. doi:10.1101/2021.09.22.461385

[176] Hagan JJ, Leslie RA, Patel S, et al. Orexin A activates locus coeruleus cell firing and increases arousal in the rat. *Proc Natl Acad Sci U S A*, 1999;96(19):10911–6. doi:10.1073/pnas.96.19.10911

[177] Lachaux JP, Rodriguez E, Martinerie J, Varela FJ. Measuring phase synchrony in brain signals. *Hum Brain Mapp*, 1999;8(4):194–208. doi:10.1002/(sici)1097-0193(1999)8:4<194::aid-hbm4>3.0.co;2-c

[178] Nunez PL, Srinivasan R, Westdorp AF, et al. EEG coherency. I: Statistics, reference electrode, volume conduction, Laplacians, cortical imaging, and interpretation at multiple scales. *Electroencephalogr Clin Neurophysiol*, 1997;103(5):499–515.

doi:10.1016/s0013-4694(97)00066-7

[179] Chapeton JI, Haque R, Wittig JH, Inati SK, Zaghloul KA. Large-Scale Communication in the Human Brain Is Rhythmically Modulated through Alpha Coherence. *Current Biology*, 2019;29(17):2801–+. doi:10.1016/j.cub.2019.07.014

[180] Mukamel EA, Wong KF, Prerau MJ, Brown EN, Purdon PL. Phase-based measures of cross-frequency coupling in brain electrical dynamics under general anesthesia. *Annu Int Conf IEEE Eng Med Biol Soc*, 2011;2011:1981–4. doi: 10.1109/IEMBS.2011.6090558

[181] Tort ABL, Komorowski R, Eichenbaum H, Kopell N. Measuring Phase-Amplitude Coupling Between Neuronal Oscillations of Different Frequencies. *Journal of Neurophysiology*, 2010;104(2):1195–1210. doi:10.1152/jn.00106.2010

[182] Marsaglia G, Tsang WW, Wang J. Evaluating Kolmogorov's Distribution. *2003*, 2003;8(18):4 %J Journal of Statistical Software. doi:10.18637/jss.v008.i18

[183] Nair J, Klaassen AL, Poirot J, Vyssotski A, Rasch B, Rainer G. Gamma band directional interactions between basal forebrain and visual cortex during wake and sleep states. *Journal of Physiology-Paris*, 2016;110(1-2):19–28. doi:10.1016/j.jphysparis.2016.11.011

[184] Benoit O, Daurat A, Prado J. Slow (0.7-2 Hz) and fast (2-4 Hz) delta components are differently correlated to theta, alpha and beta frequency bands during NREM sleep. *Clinical Neurophysiology*, 2000;111(12):2103–2106. doi: 10.1016/S1388-2457(00)00470-3

[185] Olbrich E, Rusterholz T, LeBourgeois MK, Achermann P. Developmental Changes in Sleep Oscillations during Early Childhood. *Neural Plast*, 2017;2017:6160959. doi:10.1155/2017/6160959

[186] Ebitz RB, Platt ML. Neuronal activity in primate dorsal anterior cingulate cortex signals task conflict and predicts adjustments in pupil-linked arousal. *Neuron*,

2015;85(3):628–40. doi:10.1016/j.neuron.2014.12.053

[187] Rodenbeck A, Binder R, Geisler P, et al. A review of sleep EEG patterns. Part I: A compilation of amended rules for their visual recognition according to Rechtschaffen and Kales. *Somnologie - Schlafforschung und Schlafmedizin*, 2006;10(4):159–175. doi:10.1111/j.1439-054X.2006.00100.x

[188] Bernardi G, Betta M, Ricciardi E, Pietrini P, Tononi G, Siclari F. Regional Delta Waves In Human Rapid Eye Movement Sleep. *J Neurosci*, 2019;39(14):2686–2697. doi:10.1523/JNEUROSCI.2298-18.2019

[189] Pal D, Silverstein BH, Sharba L, et al. Propofol, Sevoflurane, and Ketamine Induce a Reversible Increase in Delta-Gamma and Theta-Gamma Phase-Amplitude Coupling in Frontal Cortex of Rat. *Front Syst Neurosci*, 2017;11:41. doi:10.3389/fnsys.2017.00041

[190] Ishizawa Y, Ahmed OJ, Patel SR, et al. Dynamics of Propofol-Induced Loss of Consciousness Across Primate Neocortex. *J Neurosci*, 2016;36(29):7718–26. doi:10.1523/JNEUROSCI.4577-15.2016

[191] Migliorelli C, Bachiller A, Andrade AG, et al. Alterations in EEG connectivity in healthy young adults provide an indicator of sleep depth. *Sleep*, 2019;42(6). doi:10.1093/sleep/zsz081

[192] Miyamoto D, Hirai D, Fung CC, et al. Top-down cortical input during NREM sleep consolidates perceptual memory. *Science*, 2016;352(6291):1315–8. doi:10.1126/science.aaf0902

[193] Adamantidis A. Optogenetic deconstruction of sleep-wake circuitry in the brain. *Frontiers in Molecular Neuroscience*, 2010;2. doi:10.3389/neuro.02.031.2009

[194] Kosse C, Burdakov D. Fast and Slow Oscillations Recruit Molecularly-Distinct Subnetworks of Lateral Hypothalamic Neurons In Situ. *eNeuro*, 2018;5(1). doi:10.1523/ENEURO.0012-18.2018

[195] Vinck M, Batista-Brito R, Knoblich U, Cardin JA. Arousal and Locomotion Make Distinct Contributions to Cortical Activity Patterns and Visual Encoding. *Neuron*, 2015;86(3):740–754. doi:10.1016/j.neuron.2015.03.028

[196] Reimer J, Froudarakis E, Cadwell CR, Yatsenko D, Denfield GH, Tolias AS. Pupil fluctuations track fast switching of cortical states during quiet wakefulness. *Neuron*, 2014;84(2):355–62. doi:10.1016/j.neuron.2014.09.033

[197] Venner A, Anaclet C, Broadhurst RY, Saper CB, Fuller PM. A Novel Population of Wake-Promoting GABAergic Neurons in the Ventral Lateral Hypothalamus. *Curr Biol*, 2016;26(16):2137–43. doi:10.1016/j.cub.2016.05.078

[198] Koga K, Yamada A, Song Q, et al. Ascending noradrenergic excitation from the locus coeruleus to the anterior cingulate cortex. *Mol Brain*, 2020;13(1):49. doi:10.1186/s13041-020-00586-5

[199] Destexhe A, Contreras D, Steriade M. Spatiotemporal analysis of local field potentials and unit discharges in cat cerebral cortex during natural wake and sleep states. *J Neurosci*, 1999;19(11):4595–608

[200] Yerkes RM, Dodson JD. The relation of strength of stimulus to rapidity of habit-formation. *Journal of Comparative Neurology and Psychology*, 1908;18(5):459–482. doi:10.1002/cne.920180503

[201] Ciria LF, Suarez-Pinilla M, Williams AG, Jagannathan SR, Sanabria D, Bekinschtein TA. Different underlying mechanisms for high and low arousal in probabilistic learning in humans. *Cortex*, 2021;143:180–194. doi:10.1016/j.cortex.2021.07.002

7 Statement of contribution

All work in this dissertation was performed at Max Planck Institute for Biological Cybernetics in Tübingen, Germany.

Chapter II

Contributions: I assisted Dr. Patricia Pais-Roldán for multi-modal fMRI data acquisition and analysis. This study was supervised by Dr. Xin Yu. All work in this Chapter II has been already published in Proceedings of the National Academy of Sciences (PNAS) in 2020[10]. Therefore, all figures in this Chapter II were cited from PNAS.

Chapter III

Contributions: I performed all animal surgeries, experimental preparation, data acquisition, data analyses, and preparation of figures for the multi-modal electrophysiology experiment. I also assisted Dr. Patricia Pais-Roldán for multi-modal fMRI data acquisition. I analyzed all acquired data and generated all figures for the multimodal fMRI experiment with technical assistance from Dr. Filip Sobczak. This study was supervised by Dr. Xin Yu. All work in this Chapter III has been already posted in bioRxiv (an open access preprint server) in 2021[175]. Therefore, majority of figures in this Chapter III were cited from bioRxiv.

Chapter IV

Contributions: I performed all animal surgeries, experimental preparation, data acquisition, data analyses, and preparation of figures in this work. This study was supervised by Dr. Xin Yu. All work in this Chapter IV may be published in a peer-reviewed journal in the future since we are currently in preparation for publication.

8 Acknowledgement

First of all, I would like to thank my parents who always provided me full supports for my education. Without their support, I couldn't achieve my PhD. I can't express in words how much I appreciate for it. I would also like to express many thanks to my PhD supervisor, **Dr. Xin Yu**, who gave me an opportunity at the first place to perform scientific research and supports to pursue my scientific career. I feel grateful that I could receive many scientific advises. Special thanks to **Dr. Patricia Pais-Roldán** who kindly taught me everything I need to learn for scientific skills in my PhD research and continued to support me in every perspective even after leaving Tübingen. I would like to greatly thank to **Dr. Filip Sobczak** for offering me supports and advice for computational analyses. I would like to express sincere gratitude to **Prof. Dr. Klaus Scheffler** and **Ms. Tina Schröder** for arranging supports to complete my PhD career and to **Prof. Dr. Jan Born and Prof. Dr. Cornelius Schwarz** for offering me valuable advice and supports through advisory board meetings.

To all members of Xin's group, **Xuming, Hang, Yi, Qi, Choi, Yan, Yuanyuan**: Thanks a lot for helping me with experiments, analysis, and feedback. We had a lot of tough scientific time and discussion together, but I really enjoyed working with you all. It was also fun having activities together outside of work from time to time.

To all people from Kinderzimmer, **Sebastian, Praveen, Felix, Aaron, Dario, Emily, Nico**: I had so much fun spending time together and talking almost everyday at the office although my work had no relation to any of you. Many of you kindly offered me a lot of help for my analysis and writing, and my work quality was definitely improved. My mental quality was also maintained well because of many activities we had during or after work with delicious Swabian beers.

To all people from my office, **Kai.H, Rahel, Jiazheng, Anagha, Mark, Ali,**

Claudia, Rui, Anton: It was great sharing the office with you all. Although all of you also had no relation to my work, all of you still provided me a lot of help and inputs to my research. It was such a nice environment that I could easily ask questions at anytime when we were in the office. I also enjoyed spending lunch time together everyday.

To all other members of Klaus's group, **Marlon, Florian, Pavel, Edyta, Ju young, Vinod, Rebekka**: It was pleasure to have you all around and chat regularly for all kinds of topics. Also, many of you here offered me a lot of help for my experiments, analysis, and/or PhD-related issues.

To **Rolf, Jörn, Kai.B, Hildegard, Mihai, Timo, Elke, Rebecca**: I would like to thank for putting effort in maintenance of the scanner, preparation of experimental materials, help for animal protocols, and IT support. Without all dedicated work from you, I was not able to perform my research.

To all people from Goran's group **Tanja, Giussepe, Yulia, Liam, Gaoji, Goran**: I really appreciate that many of you also offered me supports and advice for my experiments. I also enjoyed activities together outside of work many times.

To members of electric workshops, **Oliver, Matthias, Joshi**: Thanks a lot for friendly offering me full supports whenever I needed for my experiments. All of you are so kind to spend time for improving my experimental setups.

Throughout my PhD study in Tübingen, I fully appreciate all supports that everyone offered me. Also, I am very happy that many of my colleagues have also become friends outside of work. My experience in Tübingen will be memorable for the rest of my life. At the end, I also would like to thank all my friends who I couldn't name here for giving me a lot of joy outside of work.

9 Supplementary figures

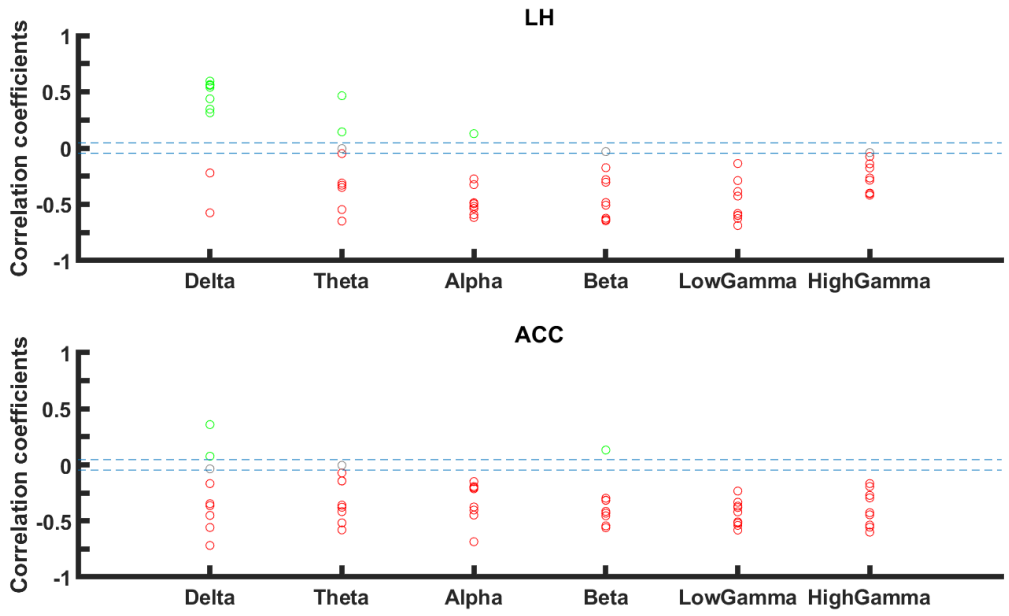

Figure S1 Correlations between pupil size and each LFP power band fluctuations at the ACC (bottom figure) and LH (top figure) in one representative animal. The positive correlation is depicted by green markers, no correlation by gray markers, and negative correlation by red markers. The blue dashed lines depict the thresholds of positive (correlation coefficents = 0.046) and negative (correlation coefficents = -0.046) correlations. (Adapted from Takahashi et al., 2021)[175].

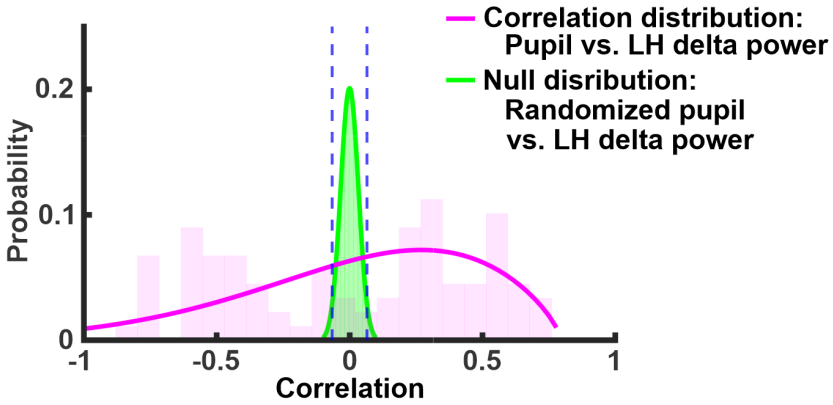

Figure S2 Distribution (pink curve) of correlations between pupil size and delta power at the LH across all trials (pink curve, 89 trials from 9 animals) and null distribution of correlations between randomized time course of pupil size and delta power with 10,000 permutations (green curve) to determine the thresholds of positive, no, and negative correlations between LFP delta power and pupil size fluctuations. 95 % confidence intervals of the null distribution for correlation coefficients were -0.046 and 0.046 (blue dashed lines). (Adapted from Takahashi et al., 2021)[175].

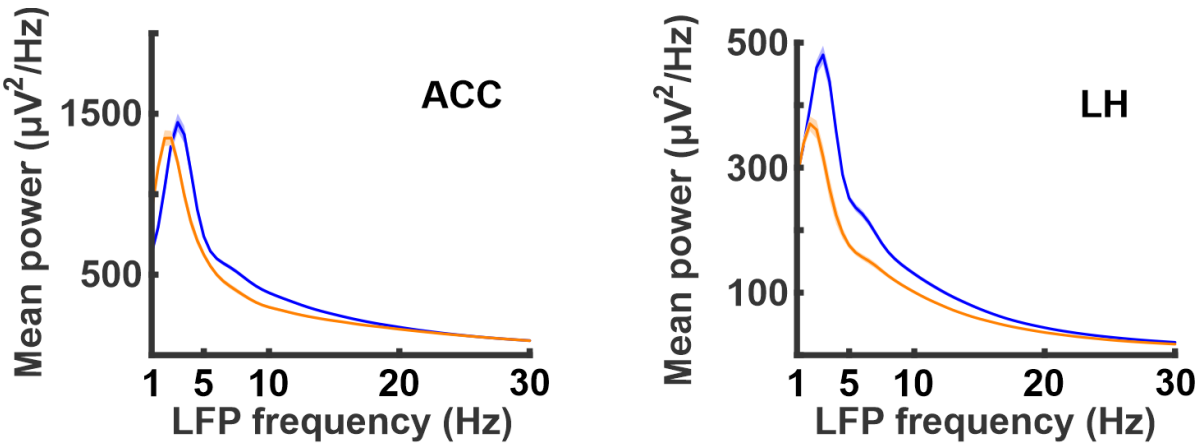

Figure S3 Power spectrum and cross frequency analyses between 1 and 30 Hz. The distribution of LFP power between 1 and 30 Hz from the ACC(left) and LH(right) are shown. The orange lines indicate trials when LH delta power and pupil size showed negative correlations (LFP-Group 1). The blue lines indicate trials when LH delta power and pupil size showed positive correlations (LFP-Group 2). The standard error of mean is indicated by shaded regions. (Adapted from Takahashi et al., 2021)[175].

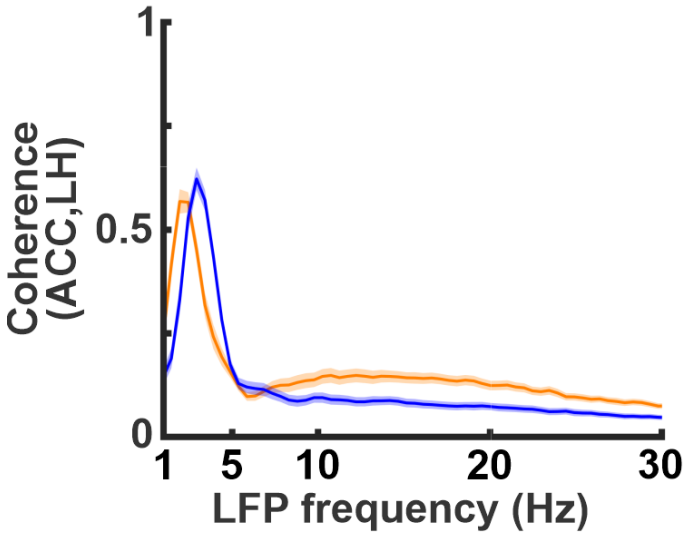

Figure S4 Coherence of electrophysiology signals in the frequency range of 1 and 30 Hz between the ACC and LH for LFP-Group 1 (orange) and 2 (blue). The standard error of mean is indicated by shaded regions. (Adapted from Takahashi et al., 2021)[175].

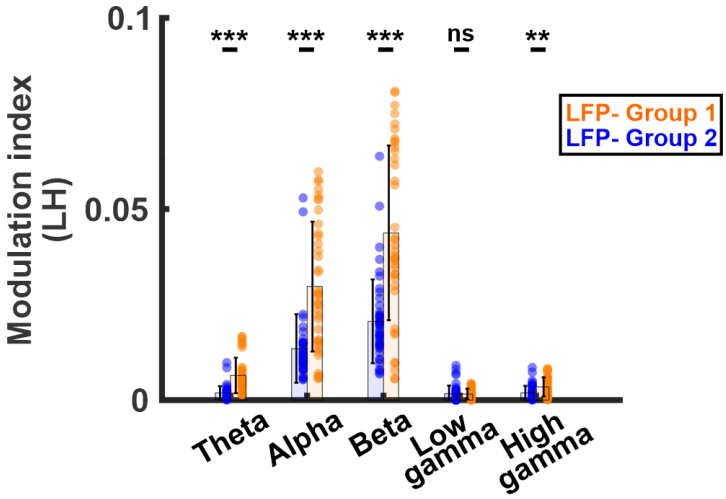

Figure S5 MI between phase angles of delta band and amplitudes of theta, alpha, beta, low gamma, and high gamma bands from LH in LFP-Group 1 (orange) and 2 (blue). The standard deviation is illustrated by error bars. Note: *** $p < 0.001$, ** $p < 0.01$, * $p < 0.05$.

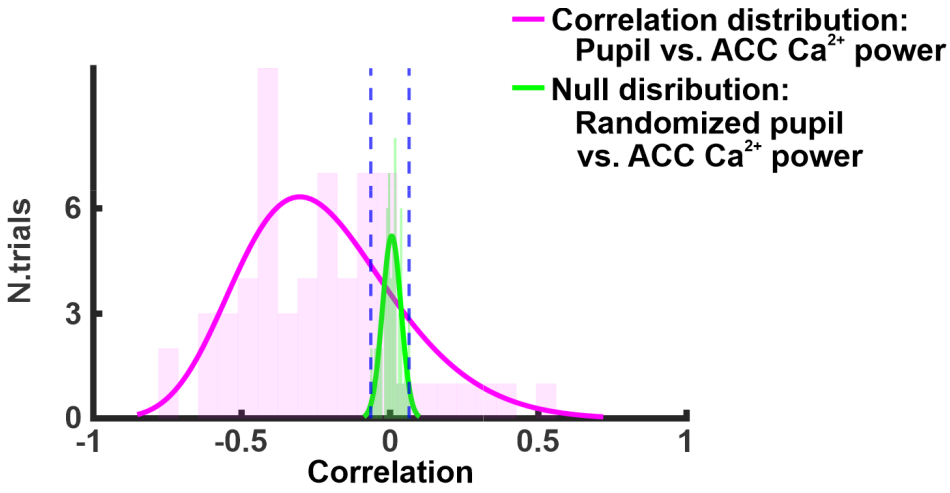

Figure S6 Distribution of correlations between pupil size and Ca^{2+} 1-4 Hz power at the ACC across all trials (pink curve, 61 trials from 9 animals) and null distribution (green curve) of correlations between randomized time course of pupil size and Ca^{2+} 1-4 Hz power at the ACC with 10,000 permutations (green curve) to determine the thresholds of positive, no, and negative correlations between ACC Ca^{2+} 1-4 Hz power and pupil size fluctuations. 95 % confidence intervals of the null distribution for correlation coefficients were -0.064 and 0.064 (blue dashed lines). (Adapted from Takahashi et al., 2021)[175].

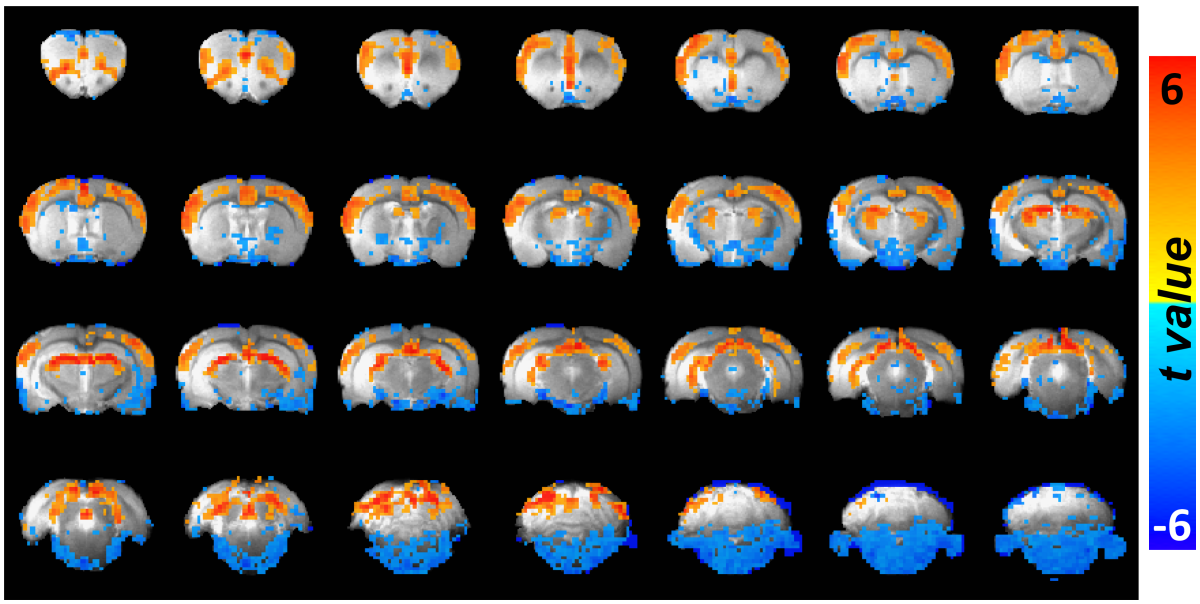

Figure S7 A t-value correlation map between fMRI voxels and Ca^{2+} 1-4 Hz power at the ACC from all trials ($n = 61$). On the overlaid correlation map, only the t-values above 2.25 and below -2.25 are displayed to demonstrate positive and negative correlations (Adapted from Takahashi et al., 2021)[175].

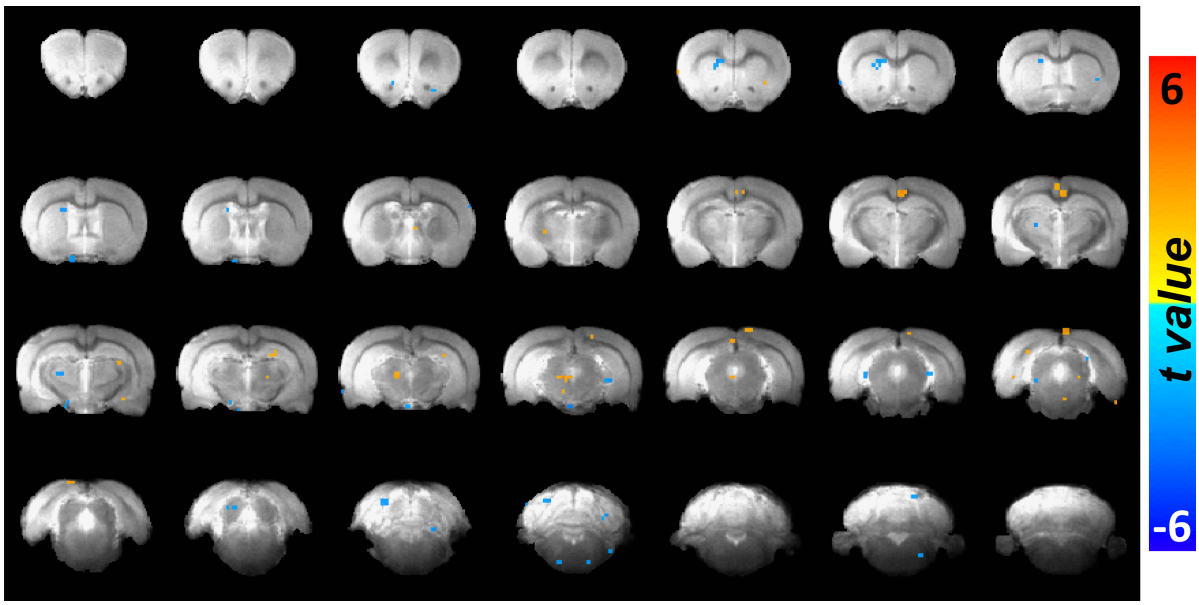

Figure S8 A t-value correlation map between fMRI voxels and Ca^{2+} 1-4 Hz power at the ACC from the trials when Ca^{2+} 1-4 Hz power fluctuation was positively or not correlated with pupil size (31 %, $n = 19$). On the overlaid correlation map, only the t-values above 2.25 and below -2.25 are displayed to demonstrate positive and negative correlations (Adapted from Takahashi et al., 2021)[175].

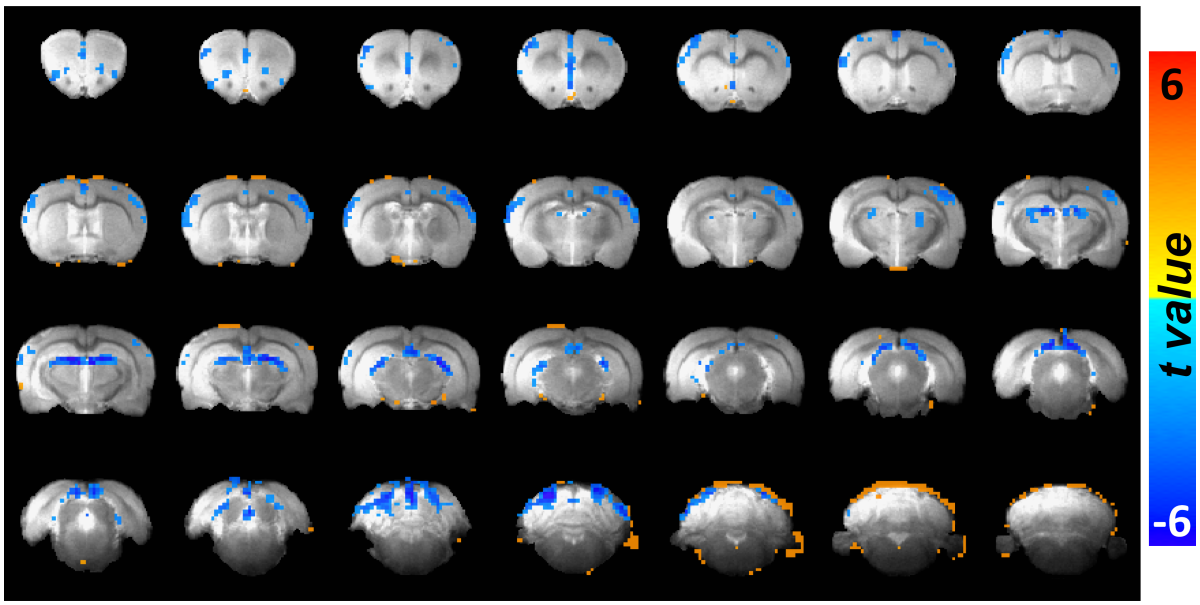

Figure S9 A t-value correlation map between fMRI voxels and pupil size from all trials ($n = 61$). On the overlaid correlation map, only the t-values above 2.54 and below -2.54 are displayed to demonstrate positive and negative correlations (Adapted from Takahashi et al., 2021)[175].

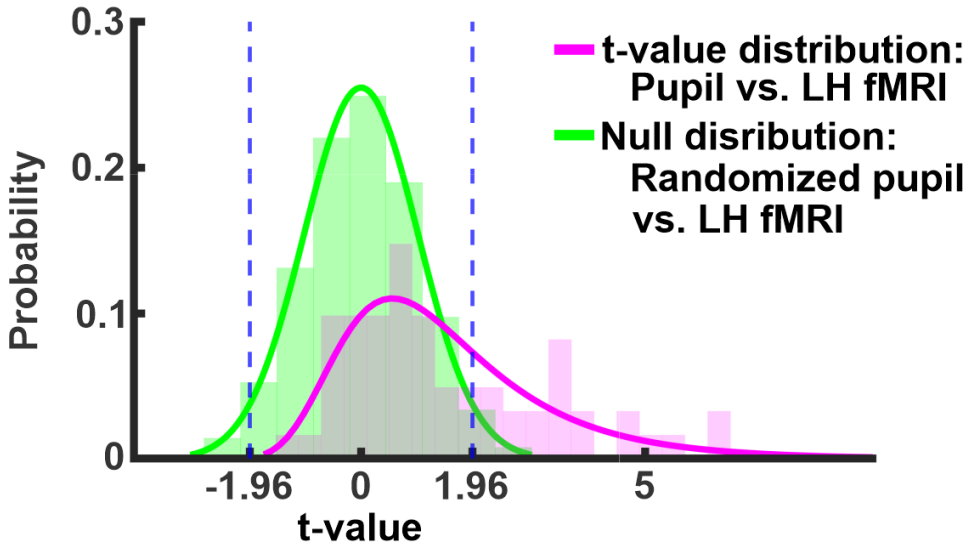

Figure S10 Distribution of correlations between pupil size and LH fMRI signal across all trials (pink curve, 61 trials from 9 animals) and null distribution (green curve) of correlations between randomized time course of pupil size and LH fMRI signal with 10,000 permutations (green curve) to determine the thresholds of positive, no, and negative correlations between LH fMRI signal and pupil size fluctuations. 95 % confidence intervals of the null distribution for t-values of correlation were -1.96 and 1.96 (blue dashed lines). (Adapted from Takahashi et al., 2021)[175].

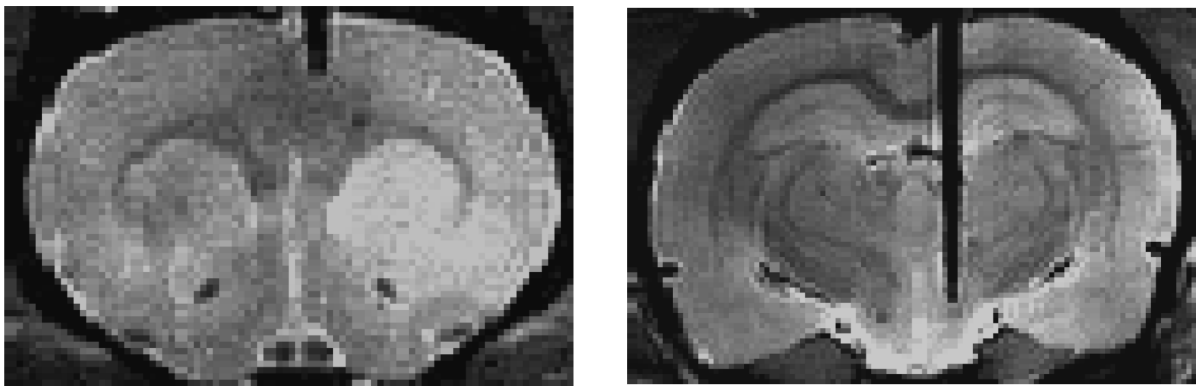

Figure S11 MR images to confirm the position of electrodes at the LH(right) and ACC (left) in a representative animal.

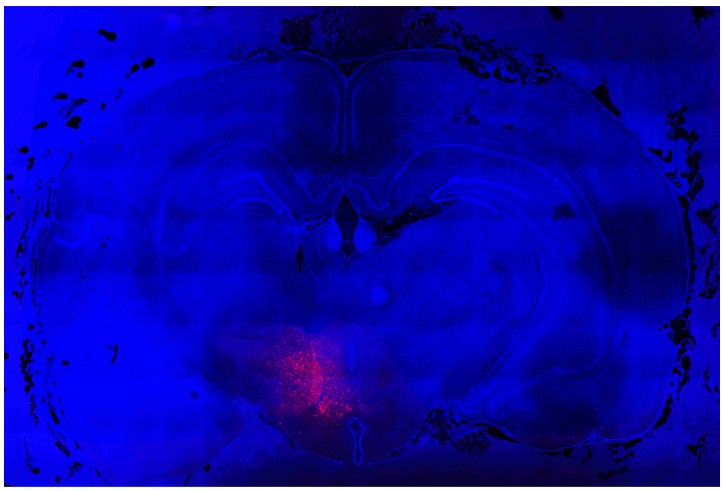

Figure S12 ChR2 expression for CaMKII^{+} neurons in the LH (red: mcherry, blue: DAPI).

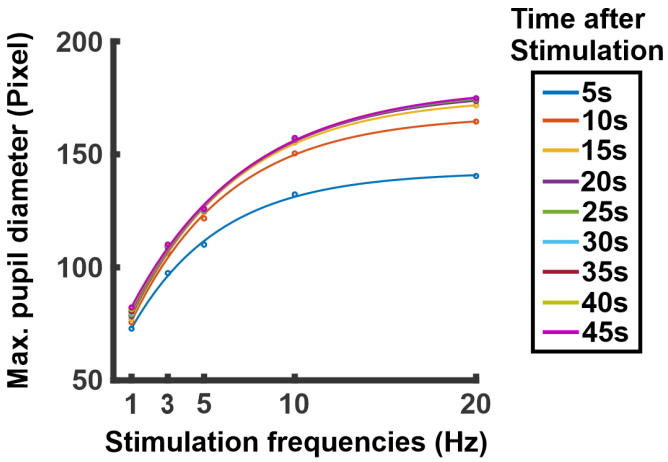

Figure S13 Exponential fit of the maximum pupil diameter after every 5 s of post stimulation period (355 trials on each stimulation frequency, 5 animals).

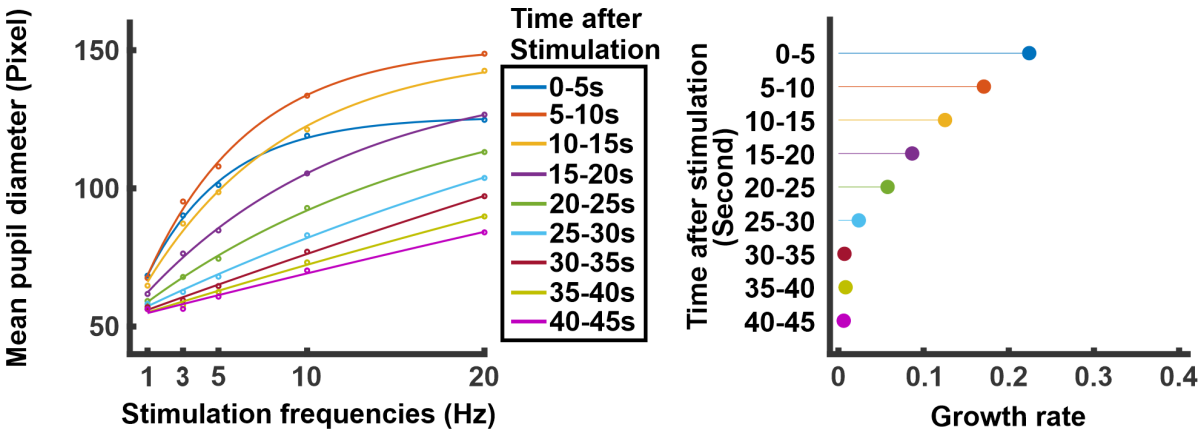

Figure S14 Exponential fit of 5 s-averaged pupil diameter from every 5 s of post stimulation period (355 trials on each stimulation frequency, 5 animals). b) The growth rate from the exponential fit of 5 s-averaged pupil diameter during every 5 s of post stimulation period.

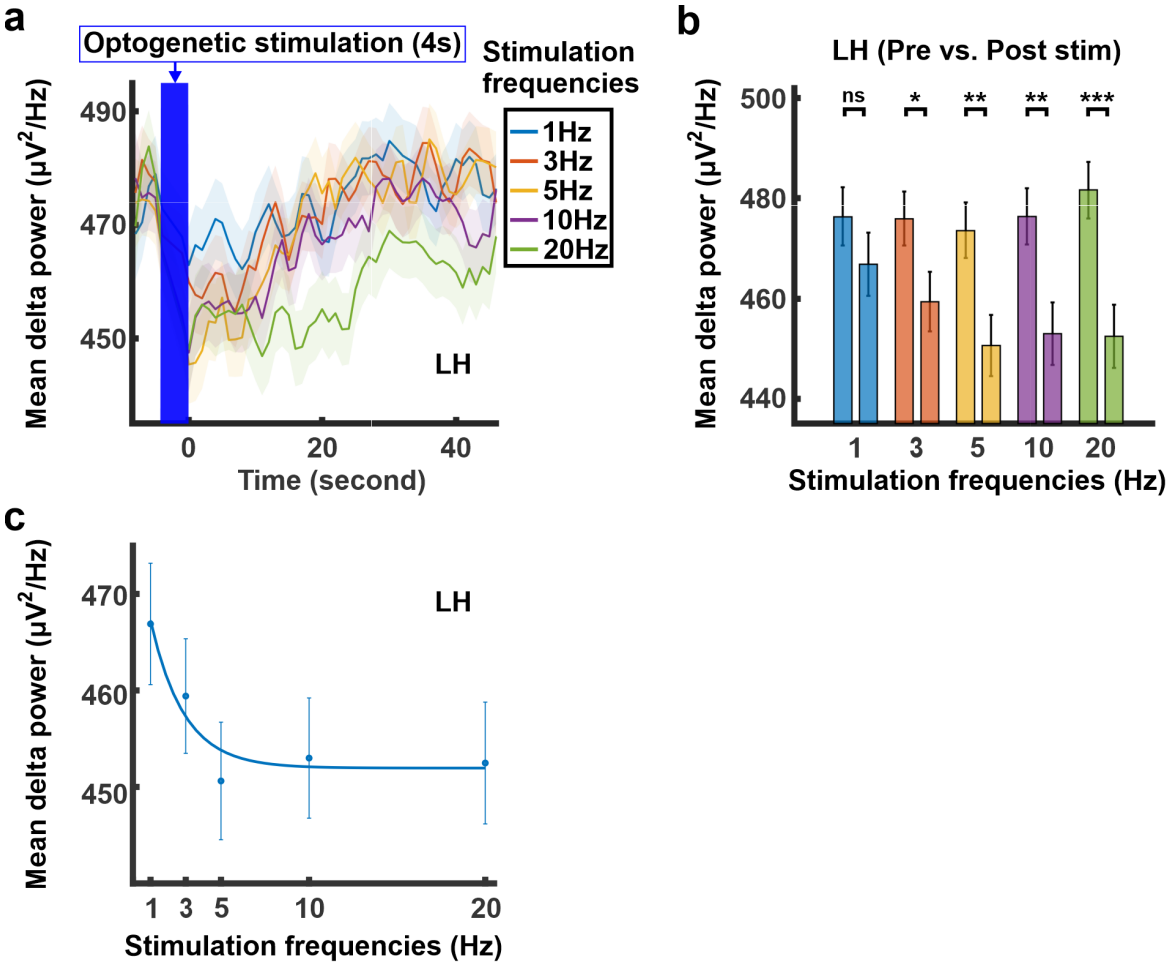

Figure S15 a) Mean LFP delta power from the LH upon optogenetics with different stimulation frequencies (4 s, blue: 1 Hz, orange: 3 Hz, yellow: 5 Hz, purple: 10 Hz, green: 20 Hz). The standard error of mean is indicated by shaded regions. b) Bar plots of LFP delta power changes from the LH comparing between pre- (8 s) and post- (8 s) stimulation periods (355 trials on each stimulation frequency, 2 s average for 1 Hz, 8 s average for 3 Hz, 7 s average for 5 Hz, 8 s average for 10 Hz, 8 s average for 20 Hz). The standard error of mean is illustrated by error bars. c) Exponential fit of mean LFP delta power at LH from post stimulation period (355 trials on each stimulation frequency, 5 animals). The standard error of mean is illustrated by error bars. Note: *** $p < 0.001$, ** $p < 0.01$, * $p < 0.05$, ns: not significant.

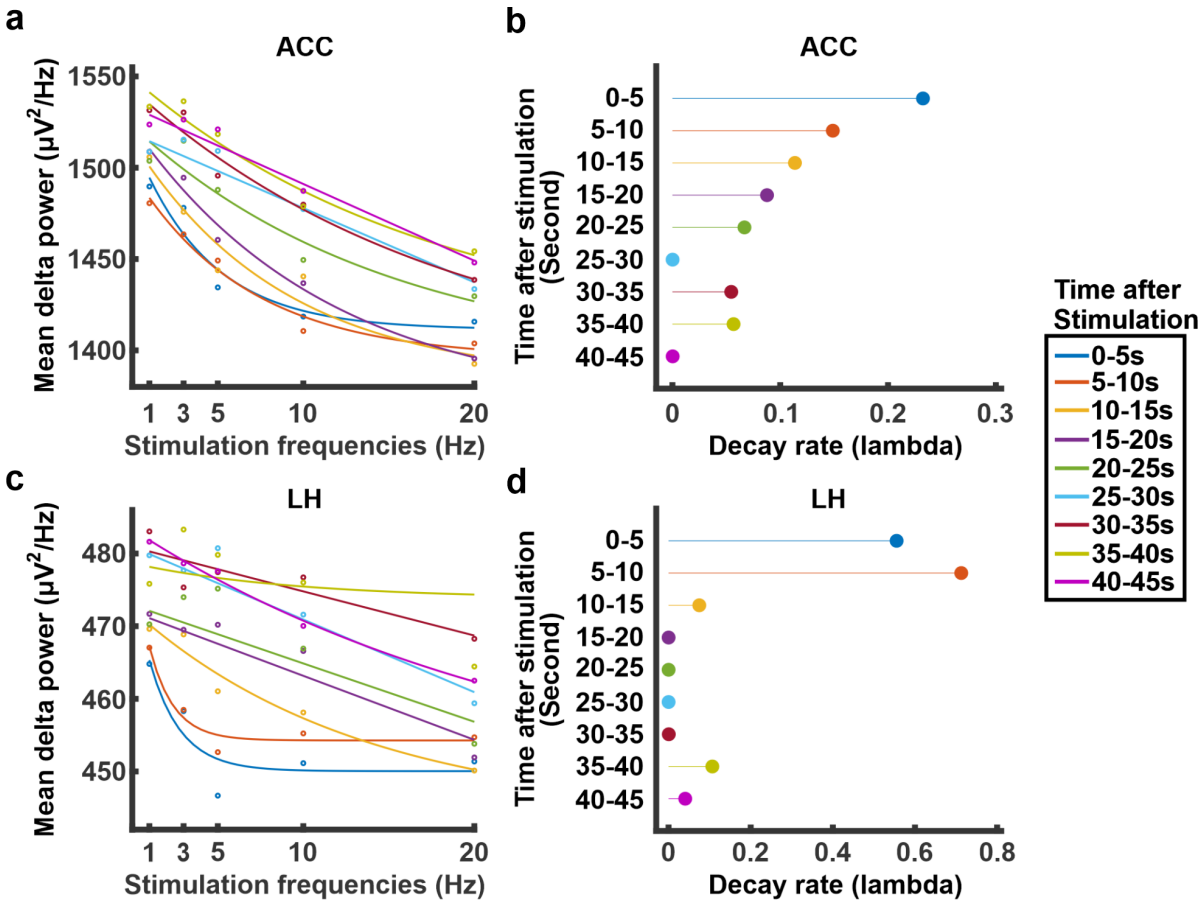

Figure S16 a) Exponential fit of 5 s-averaged LFP delta power at ACC from every 5 s of post stimulation period (355 trials on each stimulation frequency, 5 animals). b) The decay rate from the exponential fit of 5 s-averaged LFP delta power at ACC during every 5 s of post stimulation period. c) Exponential fit of 5 s-averaged LFP delta power at LH from every 5 s of post stimulation period (355 trials on each stimulation frequency, 5 animals). d) The decay rate from the exponential fit of 5 s-averaged LFP delta power at LH during every 5 s of post stimulation period.

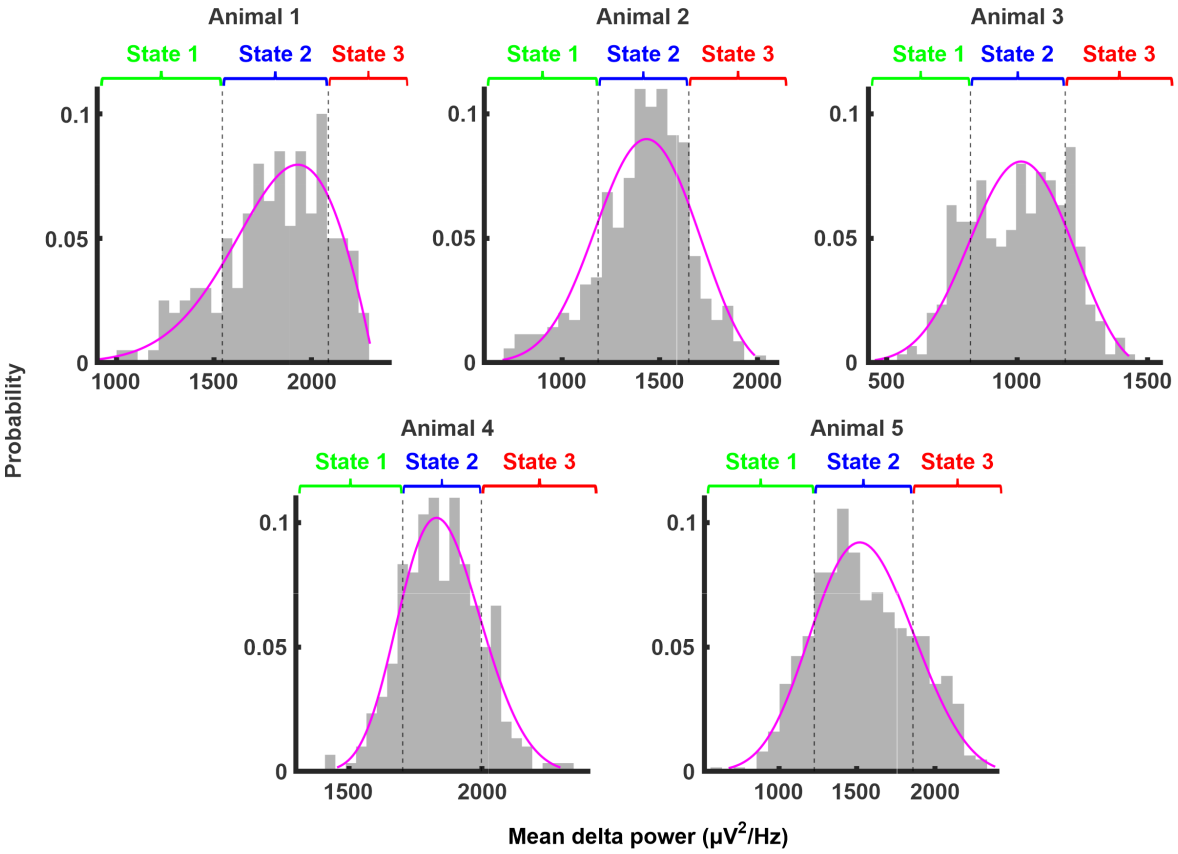

Figure S17 Delta power averaged over 5 s of pre-stimulation phase from five rats (rat1: 350 trials, rat2: 200 trials, rat3: 300 trials, rat4: 300 trials, rat5: 625 trials). Trials below 0.5 SD are defined as State 1 (green), between 0.5 and -0.5 SD as State 2 (blue), and above 0.5 SD as State 3 (red).

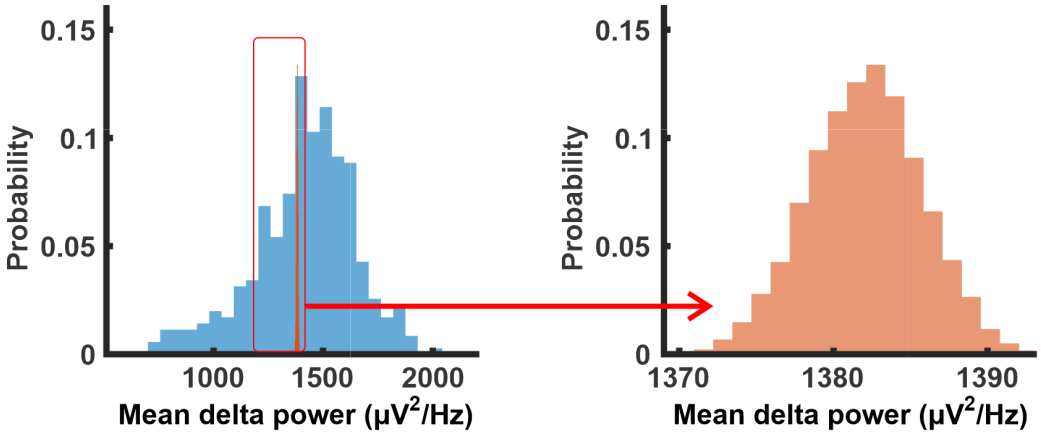

Figure S18 Bar plots for distribution of 5 s-averaged LFP delta power at ACC across all trials in one animal (left figure, blue) and null distribution of bootstrapped data with 10,000 randomization (right figure, orange) to separate trails into State 1, 2, and 3 (See Method 4.2.5).

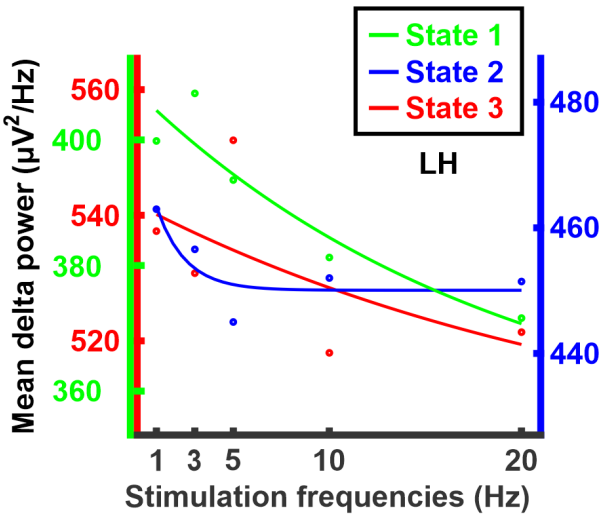

Figure S19 Exponential fit of mean LFP delta power at ACC from post stimulation period under the three different underlying brain states (Green: State 1, Blue: State 2, Red: State 3) from all five animals.

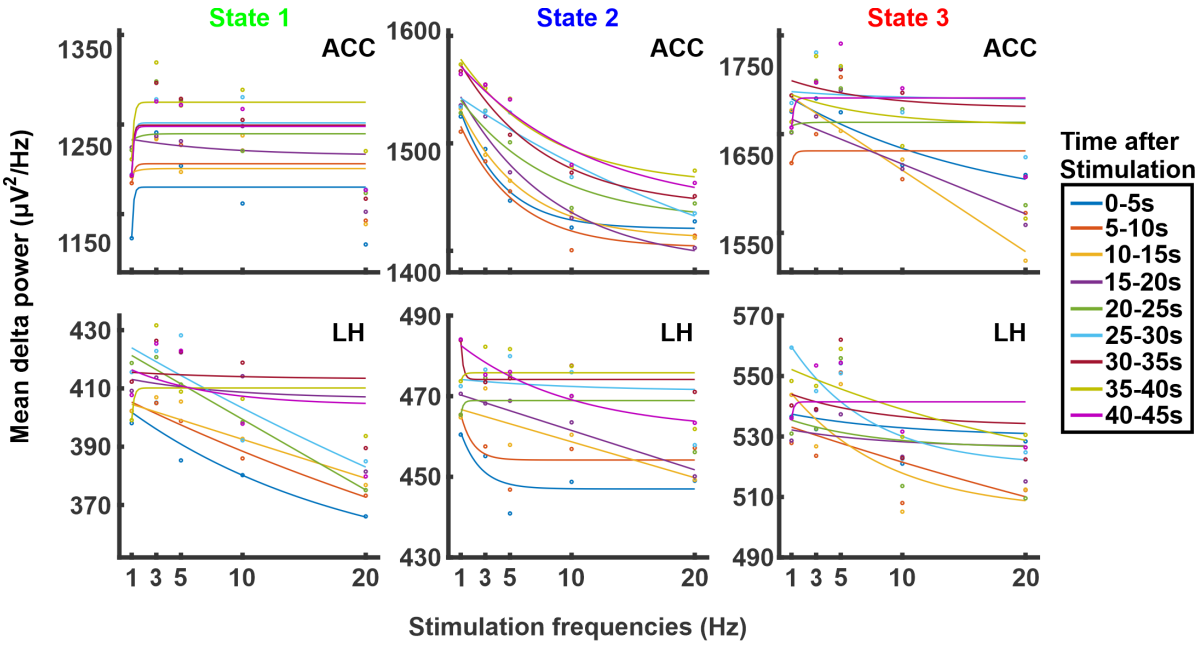

Figure S20 Exponential fit of 5 s-averaged LFP delta power at ACC (Upper figures) and LH (lower figures) from every 5 s of post stimulation period under the three different underlying brain states (Green: State 1, Blue: State 2, Red: State 3).

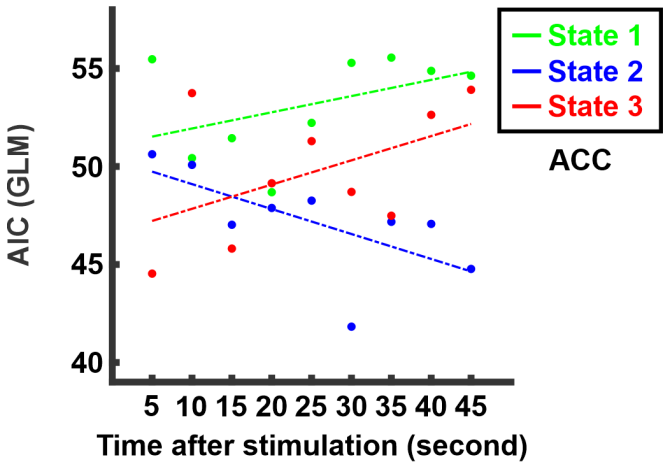

Figure S21 Akaike Information criterion (AIC) calculated from linear regression for ACC delta power in every 5 s of post stimulation period under three different underlying brain states.

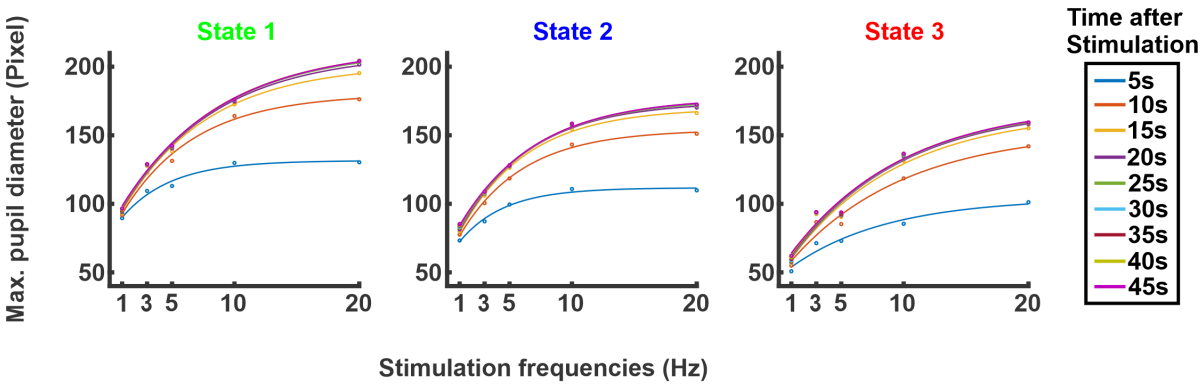

Figure S22 Exponential fit of the maximum pupil diameter after every 5 s of post stimulation period under the three different underlying brain states (Green: State 1, Blue: State 2, Red: State 3).

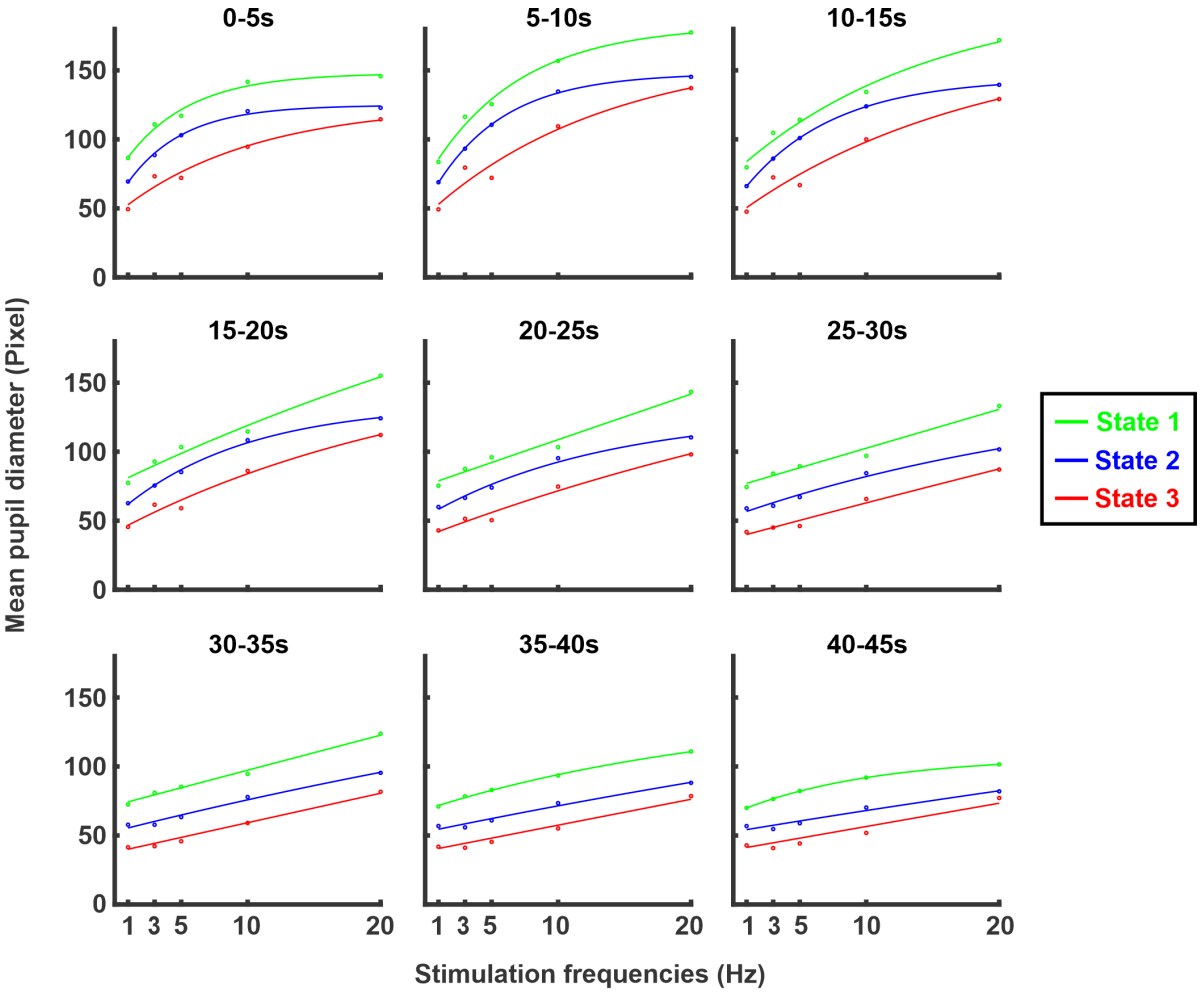

Figure S23 Exponential fit of 5 s-averaged pupil diameter from every 5 s of post stimulation period under the three different underlying brain states (Green: State 1, Blue: State 2, Red: State 3). Note: the number of trials are described in Table S12.

10 Supplementary tables

Table S1 Calculated numbers of standard deviation and means for PLV from LFP-Group 1 and 2.

	Mean		SD	
Phase locking value (ACC vs LH)	LFP-Group 1	LFP-Group 2	LFP-Group 1	LFP-Group 2
1 Hz	0.3388	0.3027	0.1536	0.1291
2 Hz	0.6596	0.4279	0.1723	0.2136
3 Hz	0.5426	0.7119	0.1393	0.1535
4 Hz	0.3724	0.5322	0.1622	0.1267
5 Hz	0.2799	0.3257	0.0977	0.1097

Table S2 Calculated numbers of standard deviation and means for MI at the ACC from LFP-Group 1 and 2.

	Mean		SD	
Modulation index	LFP-Group 1	LFP-Group 2	LFP-Group 1	LFP-Group 2
Delta phase x theta amplitude	0.0114	0.0035	0.0061	0.0019
Delta phase x alpha amplitude	0.0592	0.0247	0.0255	0.0117
Delta phase x beta amplitude	0.1201	0.0564	0.0466	0.0248
Delta phase x low gamma amplitude	0.0701	0.0361	0.0376	0.0251
Delta phase x high gamma amplitude	0.1087	0.0591	0.0443	0.0272

Table S3 Calculated numbers of standard deviation and means for MI at the LH from LFP-Group 1 and 2.

	Mean		SD	
Modulation index	LFP-Group 1	LFP-Group 2	LFP-Group 1	LFP-Group 2
Delta phase x theta amplitude	0.0065	0.0019	0.0046	0.0018
Delta phase x alpha amplitude	0.0298	0.0136	0.0170	0.0090
Delta phase x beta amplitude	0.0438	0.0207	0.0228	0.0109
Delta phase x low gamma amplitude	0.0016	0.0017	0.0014	0.0022
Delta phase x high gamma amplitude	0.0035	0.0019	0.0025	0.0018

Table S4 Adjusted R^2 (linear regression and exponential function) and Akaike information criterion from calculation of model fitting in the changes of 5 s-averaged pupil diameters.

Post-stimulation time	**0-5s**	**5-10s**	**10-15s**	**15-20s**	**20-25s**	**25-30s**	**30-35s**	**35-40s**	**40-45s**
Akaike information criterion (Linear regression)	41.184	42.507	39.330	34.428	29.177	20.972	16.733	18.072	19.580
Adjusted R^2 (Linear regression)	0.680	0.788	0.874	0.934	0.968	0.992	0.995	0.992	0.984
Adjusted R^2 (exponential function)	0.997	0.994	0.994	0.998	0.997	0.995	0.994	0.988	0.977

Table S5 Adjusted R^2 (linear regression and exponential function) and Akaike information criterion from calculation of model fitting in the changes of 5 s-averaged LFP delta power at ACC.

Post-stimulation time	**0-5s**	**5-10s**	**10-15s**	**15-20s**	**20-25s**	**25-30s**	**30-35s**	**35-40s**	**40-45s**
Akaike information criterion (Linear regression)	47.075	43.390	44.006	41.466	42.499	36.649	39.427	39.831	35.054
Adjusted R^2 (Linear regression)	0.546	0.768	0.838	0.915	0.836	0.943	0.922	0.903	0.957
Adjusted R^2 (exponential function)	0.854	0.948	0.871	0.969	0.823	0.894	0.921	0.904	0.931

Table S6 Adjusted R^2 (linear regression and exponential function) and Akaike information criterion from calculation of model fitting in the changes of 5 s-averaged LFP delta power at LH.

Post-stimulation time	**0-5s**	**5-10s**	**10-15s**	**15-20s**	**20-25s**	**25-30s**	**30-35s**	**35-40s**	**40-45s**
Akaike information criterion (Linear regression)	35.149	32.596	25.343	23.974	29.281	25.123	26.353	29.918	18.054
Adjusted R^2 (Linear regression)	0.023	0.074	0.893	0.919	0.792	0.914	0.696	0.654	0.973
Adjusted R^2 (exponential function)	0.618	0.877	0.909	0.810	0.537	0.833	0.544	-0.487	0.983

Table S7 Calculated numbers from the exponential function (See Equation 4.5) in the reduction of LH and ACC delta power under State 1, 2, and 3.

	ACC			LH		
Parameters	**a**	**b**	**lamda**	**a**	**b**	**lamda**
State 1	1144.109	312936.442	8.835	350.737	-56.856	0.052
State 2	1415.062	-149.186	0.278	450.055	-26.011	0.671
State 3	-11404.798	-13133.180	0.000	500.033	-41.669	0.038

Table S8 Adjusted R^2 (linear regression and exponential function) and Akaike information criterion from calculation of model fitting in the changes of 5 s-averaged LFP delta power at ACC under State 1, 2, and 3.

	Post stimulation time	0-5s	5-10s	10-15s	15-20s	20-25s	25-30s	30-35s	35-40s	40-45s
State 1	Akaike information criterion (Linear regression)	55.471	50.428	51.442	48.687	52.225	55.287	55.554	54.878	54.632
	Adjusted R^2 (Linear regression)	-0.014	0.280	0.193	0.485	0.388	-0.104	0.055	-0.221	-0.063
	Adjusted R^2 (exponential function)	-0.533	-0.871	-0.986	-0.746	-0.968	-0.473	-0.589	-0.226	-0.480
State 2	Akaike information criterion (Linear regression)	50.624	50.082	47.027	47.883	48.257	41.827	47.177	47.070	44.773
	Adjusted R^2 (Linear regression)	0.459	0.539	0.756	0.810	0.652	0.907	0.783	0.733	0.839
	Adjusted R^2 (exponential function)	0.914	0.877	0.993	0.933	0.746	0.877	0.936	0.874	0.894
State 3	Akaike information criterion (Linear regression)	44.534	53.743	45.811	49.145	51.293	48.703	47.488	52.633	53.912
	Adjusted R^2 (Linear regression)	0.741	0.243	0.914	0.709	0.513	0.567	0.683	0.633	0.196
	Adjusted R^2 (exponential function)	0.672	-0.977	0.854	0.475	-0.992	-0.835	-0.628	-0.676	-0.863

Table S9 Calculated numbers from the exponential function (See Equation 4.5) in an increment of the maximum pupil size under State 1, 2, and 3.

Parameters	a	b	lamda
State 1	209.910	129.823	0.133
State 2	174.360	111.981	0.177
State 3	170.863	123.652	0.115

Table S10 The values of exponential growth (λ) from model fitting (See Equation 4.5) on 5 s-averaged pupil size every 5 s of the post-stimulation phase under State 1, 2, and 3.

Post-stimulation time	**0-5s**	**5-10s**	**10-15s**	**15-20s**	**20-25s**	**25-30s**	**30-35s**	**35-40s**	**40-45s**
State 1	0.209	0.148	0.068	0.019	0.000	0.000	0.000	0.042	0.099
State 2	0.239	0.191	0.148	0.106	0.076	0.035	0.013	0.010	0.007
State 3	0.099	0.074	0.056	0.040	0.021	0.004	0.000	0.000	0.000

Table S11 Adjusted R^2 (linear regression and exponential function) and Akaike information criterion from calculation of model fitting in the changes of 5 s-averaged pupil size every 5 s of the post-stimulation phase under State 1, 2, and 3.

Post-stimulation time		0-5s	5-10s	10-15s	15-20s	20-25s	25-30s	30-35s	35-40s	40-45s
State 1	Akaike information criterion (Linear regression)	41.818	42.908	36.701	31.376	30.776	28.767	23.271	22.916	28.565
	Adjusted R^2 (Linear regression)	0.680	0.824	0.943	0.973	0.969	0.973	0.988	0.982	0.915
	Adjusted R^2 (exponential function)	0.966	0.981	0.970	0.964	0.953	0.954	0.981	0.996	1.000
State 2	Akaike information criterion (Linear regression)	41.786	43.172	40.595	36.468	32.734	27.388	24.939	24.713	25.609
	Adjusted R^2 (Linear regression)	0.627	0.742	0.828	0.896	0.931	0.968	0.976	0.967	0.944
	Adjusted R^2 (exponential function)	0.991	0.999	1.000	0.994	0.979	0.970	0.966	0.953	0.917
State 3	Akaike information criterion (Linear regression)	37.250	40.051	37.532	33.177	29.932	26.987	22.634	25.156	29.131
	Adjusted R^2 (Linear regression)	0.877	0.887	0.921	0.952	0.966	0.974	0.986	0.973	0.934
	Adjusted R^2 (exponential function)	0.929	0.901	0.922	0.950	0.955	0.961	0.973	0.938	0.850

Table S12 The number of trials tested for 1 Hz, 3 Hz, 5 Hz, 10 Hz, and 20 Hz of stimulation frequencies under State 1, 2, and 3.

Stimulation frequency	**1 Hz**	**3 Hz**	**5 Hz**	**10 Hz**	**20 Hz**
# of trials in State 1	113	100	119	118	97
# of trials in State 2	124	139	142	124	128
# of trials in State 3	118	116	94	113	130